MECHANICS OF PARTICLE AND POLYMER ASSEMBLIES

by

Yujie Sun

BS, University of Science & Technology of China, 1996

MS, University of Science & Technology of China, 1999

Submitted to the Graduate Faculty of

Arts & Sciences in partial fulfillment

of the requirements for the degree of

Doctor of Philosophy

University of Pittsburgh

2005

UNIVERSITY OF PITTSBURGH

FACULTY OF ARTS AND SCIENCES

This dissertation was presented

by

Yujie Sun

It was defended on

April 15th, 2005

and approved by

Prof. Hai Lin

Prof. Steve Weber

Prof. David Waldeck

Prof. Gilbert Walker
Dissertation Director

Mechanics of Particle and Polymer Assemblies

Yujie Sun, PhD

University of Pittsburgh, 2005

ABSTRACT

This thesis reports a variety of developments in atomic force microscopy (AFM) methodology and surface preparation techniques.

Methodologies of assembling colloidal particles into pre-designed patterns on surfaces were studied. Different interactions, such as electrostatic force, magnetic force, and capillary force of varied topography were used. In the topography-assisted particle assembly, the direct observations of the dynamics revealed that the particles are transported inside or toward the grooves of the pattern in the region where the liquid film is appropriately thin, and the particles' self-assembly inside the grooves is caused by a lateral capillary force. Scanning probe microscopy was used to examine topography assisted 2D self-assembly of micrometer-size latex particles in wetting films.

Based on the adhesive interactions between an AFM tip and sample surfaces, an AFM method for measuring surface elasticity was proposed. The method is particularly useful when there is a large adhesion between the tip and soft samples, when the indentation method would be less accurate. For thin and soft samples, this method has much less interference from the substrate than is found using the indentation method because there is only passive indentation induced by tip-sample adhesion. The model was tested on PDMS polymers with different crosslink density. It was found that soft, less crosslinked PDMS polymers showed obvious viscoelastic behavior when interacting with AFM tips. Systematic studies of the viscoelastic effects found that energy dissipation occurs mainly in the bulk of polymer when an AFM tip indents into a polymer. When the tip is pulled out from the polymer, the energy dissipation occurs both in the bulk and interfaces, which causes a turning point of the adherence force of AFM tip with changes of scan rates. The multiple relaxation rates were characterized and compared with that from other methods.

Using AFM imaging and indentation methods, the properties of barnacle adhesive were studied. A multilayered structure of barnacle adhesive plaque was proposed based on layered modulus regions measured by AFM indentation. Analysis shows that there is a strong correlation between the mean Young's moduli of the outmost softest adhesive layer and the barnacle shear strength, but no correlation for other higher modulus regions. Linear, quadratic, and Griffth's failure criterion regressions were used in the fit, and showed close correlation.

ACKNOWLEDGEMENTS

First of all, I would like to give my sincere appreciation to Prof. Gilbert Walker for his invaluable guidance throughout my PhD study. This thesis could not have been completed without his consistent support and encouragement. He has given me great freedom in my research while always keeping keen sights on where and how my projects should go. I really enjoyed working on the projects during the PhD under his guidance.

I am grateful to Prof. David Waldeck and Prof. Steve Weber. They were both on my comprehensive exam committee, and are now on my Ph.D. dissertation committee. Their scientific integrity and personal encouragement have been very important for me.

Special thanks to Prof. Boris Akhremitchev at Duke University, a former member of Walker group, for his great discussion and collaboration. I am also thankful to other former and present colleagues in this group. Dr. Jason Bemis gave me a lot help on Matlab programming and AFM data processing. Senli Guo gave me a great hand in the barnacle project. Rojana Leecharoen, Dr. Slava Romanov, Alexei Tivanskii, and Larissa Stebunova gave me valuable discussions in my research.

Thanks to Prof. Manoj Chaudhury and his students for PDMS samples and modulus data.

Finally, I present my deep appreciation to my wife, daughter, parents, parents-in-law, and two elder brothers' families. My wife, Rong Meng, has been giving me lovely support and encouragement in my work while she has been also working on her PhD degree. My daughter, Mengtang Sun, my princess and the source of my happiness, makes me feel confident in front of frustration in my research. My parents, mother-in-law, and sisters-in-law sacrificed much of their time to take care of my daughter. I can not imagine how I could have finished my work without their help. I would like to dedicate this thesis to my family.

TABLE OF CONTENTS

LIST OF TABLES

LIST OF FIGURES

Chapter 1. Introduction

An Overview

Phenomena at interfaces are of extreme interest and attention because their important applications in material developments in many different fields, such as biomedicine, space, environmental science, and semi-conductor[1].

Assemblies of particles into pre-designed structures have invaluable potentials in the generation of novel optical materials, photonic crystal devices, biological sensors and lithographic or non-lithographic masks, etc.[2]. Ideally, particle assembly should be simple, quick, efficient, universal, reproducible, and with tolerable number of defects in the assembly. Extensive work has been conducted on the search of such methods over the last decade. So far, a number of strategies have been explored to fabricate colloidal particle based 2-dimensional and 3-dimensional mesoscale structures. These strategies utilize different effects such as electrostatic interactions, external electric fields, covalent bonding, capillary forces, optical force, cross linkers, and topography[3-9].

In the first part of my work, Chapter 2, I describe my research on methodologies of assembling colloidal particles into pre-designed patterns on surfaces. The 2-dimensional self-assembly of micrometer-size latex particles in wetting films on patterned poly-dimethylsiloxane (PDMS) polymer surfaces is investigated in detail. It is found that this topography-assisted method is simple, efficient, and universal. The obtained patterns of particle assembly are reproducible as faithful replicates of the substrate and with a small number of defects, see Figure 1-1. Varying the constitution and size of particles and substrate patterns accordingly can thus produce required functional devices based on assembled particle patterns.

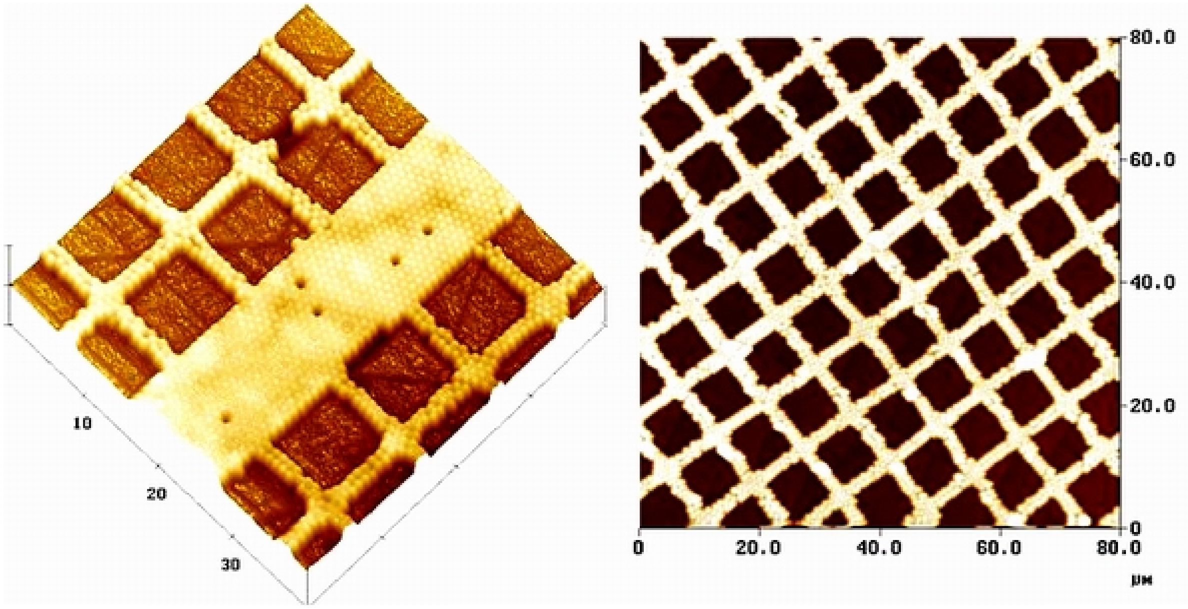

Figure 1-1. AFM height images of assembled colloidal particle arrays prepared by the topography-assisted method. Particles are well assembled in the grooves with a few defects.

The dynamics of the processes involved in the 2-dimensional particle assembly were directly observed using an integrated zoom microscope and CCD camera. The direct observations revealed the particles are transported inside or toward the grooves of the pattern in the region where the liquid film is appropriately thin, and the self-assembly of particles inside the grooves is caused by a lateral capillary force.

The measurements of moduli of materials and biological objects are essential for the improvement of material design and the understanding of mechanisms of their mechanical properties. Atomic force microscopy (AFM) has been used extensively in the quantification of the mechanical properties of materials, such as modulus, viscoelasticity, and yield strength. AFM can probe local surface mechanical properties with much higher resolution, down to several tens of nanometers, and with much finer control of applied force, down to several nano-newtons. These two characteristics give the AFM advantages over other tools for studying the mechanical properties of polymeric systems and biological systems because most of these systems have a nano-scale heterogeneous modulus distribution.

In the second part of my work, Chapter 3 - 5, I describe my research on the development of a novel method for measuring surface elasticity, based on the adhesive interactions between AFM tip and samples surfaces. The viscoelastic effects in the tip-PDMS sample adhesive interactions are investigated systematically. The mechanical properties of barnacle adhesive polymers are studied using AFM imaging and indentation methods. A multilayered structure of barnacle adhesive plaque was proposed based on layered modulus regions measured by AFM indentation.

Chapter 3 proposes a novel method of surface elasticity measurement based on the adhesive interactions between an AFM tip and sample surfaces, see Figure 1-2. The method is particularly useful when there is a large adhesion between the tip and soft samples, when the indentation method would be less accurate. The model is tested on PDMS polymers with different crosslink densities, and found to work well on soft samples.

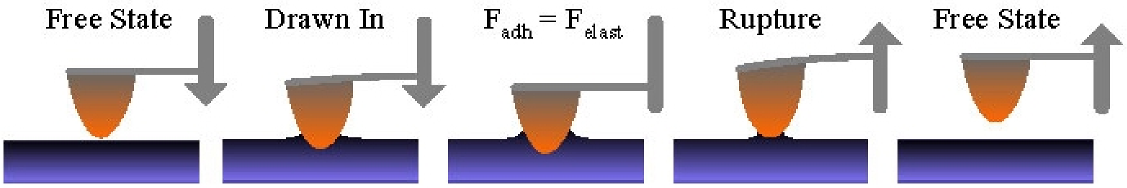

Figure 1-2. Measurement of surface elasticity of material based on the adhesive interactions between an AFM tip and sample surfaces. Here the process of tip-sample adhesive interaction is schematically demonstrated.

During the test of the method of elasticity measurement, it is found that for soft, less crosslinked PDMS polymers, the elasticity values obtained are consistently larger than that obtained by the macroscopic method. We think this is because the less crosslinked PDMS polymers have larger viscoelastic behavior when interacting with AFM tips. In Chapter 4, I systematically investigate the viscoelastic effects of the tip-sample adhesive interactions. It is found that energy dissipation occurs mainly in the bulk of polymer when an AFM tip indents into a polymer. When the tip is pulled out from the polymer, the energy dissipation occurs both in the bulk and interfaces, which causes a turning point of the adherence force of AFM tip, as a function of scan rates. Multiple relaxation rates are characterized.

Using AFM imaging and indentation methods, the properties of barnacle adhesive are studied in Chapter 5. A multilayered structure of barnacle adhesive plaque is proposed based on layered modulus regions measured by AFM indentation, see Figure 1-3. Analysis shows that there is a strong correlation between the mean Young's moduli of the outmost softest adhesive layer and the barnacle shear strength, but no correlation for other higher modulus regions.

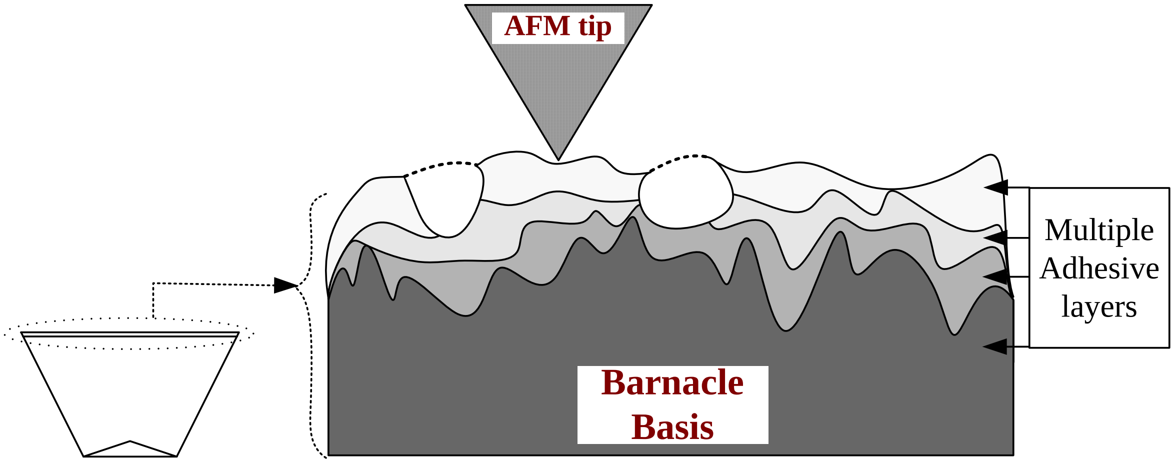

Figure 1-3. A cartoon shows the multilayered structure of adhesive on barnacle baseplates.

Chapter 6 summarizes my work on the studies of mechanics of particle assembly and polymeric systems.

1.1. A review of the current developments of colloidal particle assembly and applications

The objects that have some linear dimension between 1 nm to 1 μm are usually referred to as colloidal particles.[10] Colloidal particles and colloidal phenomena play important roles in chemistry, biology, material science, environmental science and industry. Figure 1-4 lists some colloidal systems, together with their typical critical dimensions.[11]

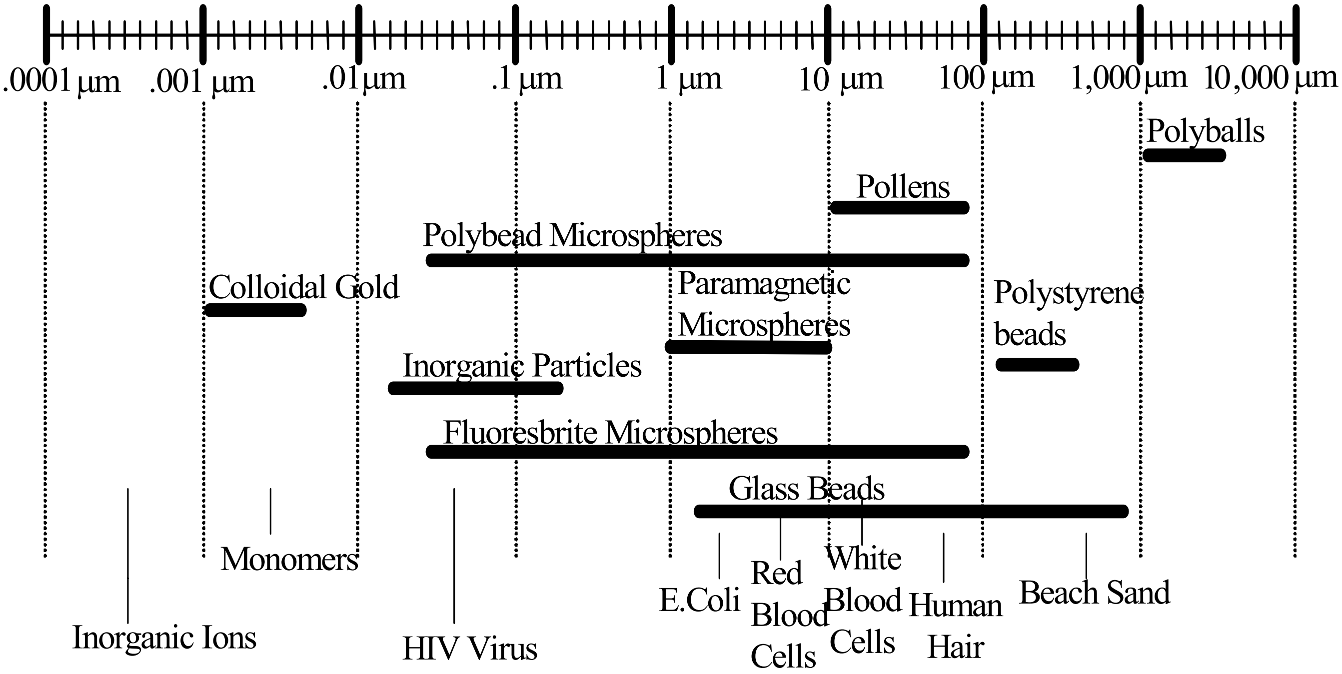

Figure 1-4. A list of some colloidal systems with their typical range of critical dimensions.

Beyond the interesting and useful properties of individual particles, colloidal particles are able to organize themselves into ordered structures which render some special collective properties. Therefore, by combining the choice of material (constituent material or surface functional groups) and controlling the assembly of the particles, researchers make novel materials exhibiting properties remarkably different from conventional engineering materials, and devices with much better efficiency than those made from conventional materials without particulate substructures.

Particle assembly is usually carried out in 2 dimensional (2D) and 3 dimensional (3D) to fabricate desired arrays. So far, a number of strategies have been explored to fabricate colloidal particle based 2D and 3D mesoscale structures. These strategies utilize different effects such as electrostatic interactions, external electric fields, covalent bonding, capillary forces, optical force, cross linkers, and topography.

1.1.1. Methods for 2D assembly of colloidal particles:

(1) A method based on solvent evaporation[4,12-15]:

This is apparently the simplest way to self-assemble colloid particles into 2D crystals. In this method, a liquid dispersion of colloidal particles is spread onto the surface of a solid substrate. As the solvent evaporates, the colloidal particles are self-assembled into a closely packed, hexagonal array because of the attractive capillary forces among the colloidal particles. In order to get a relatively large crystalline domain size, there are several prerequisites for the substrates: the surface has to be chemically homogeneous, clean, flat and hydrophilic (most of colloidal dispersions are aqueous). As a consequence, almost all experiments have been done on glass plates or polished silicon wafers as substrates. Mica was also used in a few occasions, whereas other materials, e.g. semiconductors or metals, have been used hardly at all.

(2) A method based on the Langmuir film technique[5,16-18]:

Colloidal particles can also self-assemble to form a monolayer on a liquid-liquid or liquid-gas interface. Then in principle, the monolayer could be transferred to any substrate, either by the sub phase-lowering method or by the Langmuir-Blodgett technique. This method requires modification of the colloidal particles so that they can stay in the interface. And it also needs a precise control of surfactant concentration and pH, hence the quality of colloidal arrays made by this method is hard to control.

(3) A method based on controlling electrostatic interactions[7,19-23]:

Electrostatic interactions between charged particles and substrate surfaces provide another means to fabricate colloidal particle based nanostructures. In this method, the substrate surfaces firstly are modified to have a self-assembled monolayer which has charges or ionizable end groups. Then the surfaces are soaked in an oppositely charged colloidal dispersion. The electrostatic attraction between the particles and substrates will specifically assemble the particles on the surfaces. There are advantages: (a) by combining this method with micro-contact printing technique[24], one can fabricate desirable 2D structure of colloidal particle assembly; (b) by controlling the ionic strength and pH value of the solution, one can finely control the condition of particle absorption. An unfortunate outcome is that compared to other methods, particle assembly is generally poor (the colloidal particles do not close pack).

(4) A method based on electrophoretic deposition[25-28]:

In this approach, a liquid dispersion of colloidal particles is confined between two parallel solid electrodes such as indium tin oxide (ITO)-coated microscope coverslips. When a sufficiently strong electric field (50-100 V/cm) is applied, the colloidal particles that have been randomly deposited on the anode will move toward each other to form a stable 2D hexagonal array. The entire process can be modulated by changing the amplitude of the applied electric field. It has been suggested that the long-range attraction between the colloidal particles is caused by electrodynamic flows which, in turn, were induced by distortions in the applied electric field and the passage of ionic current through the solution. By applying a mask, this approach can also produce a designed pattern of colloidal particle assembly.

(5) A method based on optical manipulation[29,30]:

When a laser beam is focused to a diffraction-limited spot using a high-numerical-aperture objective, micrometer-sized objects in solution are attracted and trapped in three dimensions into the region of highest light intensity. This means laser beams can be used to assemble colloidal particles in a very precise and free way. Infrared trapping beams are not strongly absorbed by biological tissue and hence cause little optical damage. With their remote and sterile nature, optical tweezers are particularly appealing for biological studies. The shortcomings of this approach are as obvious as its advantages. First, although optical tweezers are able to precisely control the position of particles, it is hard to manipulate a bunch of particles at the same time. The method has to be done with fixation in liquid or gas phase. Also, the set up and running of the instrument are much more expensive than the other methods for the assembly of colloidal particles.

(6) Template-Assisted Assembly[31-35]:

Here we refer to "template-assisted assembly" as "topographically driven particle self-assembly". It is a powerful means to direct and control assembly processes. In the method, a liquid dispersion of colloidal particles is place onto a topographically patterned surface (sometimes the surfaces are confined within a boundary). As the water evaporates, the particles are trapped and self-assemble within the lower features of the patterned surface. This method is a fast and low cost way to produce designed pattern of colloidal particle assembly. Actually, it is a branch of the method of the "evaporation method".

(7) Covalent interactions[36-38] and lock-and-key interactions (biological or non-biological linker)[39-43]:

The elements of these two methods are basically similar to those methods based on electrostatic interaction except they utilize the covalent or lock-and-key interactions rather than electrostatic interactions. To use covalent interactions, usually a substrate surface is first modified with a self-assembled monolayer which has a certain kind of functional group, then this surface is dipped into a colloidal dispersion where the colloids themselves or the functional groups on them can covalently bind to the surface functional groups. In different versions of the lock-and-key method, complimentary DNA-DNA, biotin-avidin, complementary antigen-antibody interactions and other non-biological linkers are used to assemble colloidal particles. The colloidal particles can be assembled in the solution without a solid substrate.

(8) *In situ* particle formation and fabrication by patterned SAMs[3,44]:

A few research groups have used this method to fabricate 2D colloid arrays. In this method, a patterned SAM is formed on a substrate surface by the micro-contact printing technique. This renders a heterogeneous hydrophilicity on the surface, *i.e.,* the SAM-covered and -uncovered areas have reversed hydrophilicity. After the substrate is dipped in and taken out from a solution of an inorganic salt, the solution micro-droplets will preferably stay in the hydrophilic area. Under controlled conditions, the evaporation of the solvent will leave a nanocrystal of the inorganic salt in one element of the hydrophilic arrays. The size of the nanocrystals will depend on many factors like the element area of the arrays, the concentration of the solution, the evaporation condition, etc.. This method so far has only been used to produce 2D arrays of inorganic salt nanocrystals and magnetic oxide crystals. It should also have in principle some applications in bio-colloids assembly.

1.1.2. The methods for 3D assembly of colloidal particles:

(1) A method based on sedimentation[45-47]:

This is the most common approach to the formation of 3D crystalline arrays of colloidal particles. This method involves several processes such as gravitational settling, translational diffusion, and crystallization. Although it is very simple, this method has a few limitations and disadvantages: the size and density of the particles should be high enough to overcome their random thermal motions and to allow them to sink; The sedimentation process should be slow enough to allow the hard-sphere disorder-to-order phase transition at the interface between the crystalline surface and water; it is hard to control the morphology of the top surface and the number of layers of the 3D crystalline arrays; it takes relatively long time (weeks to months) to complete the process.

(2) Crystallization *via* Repulsive Electrostatic Interactions[48,49]:

Under appropriate conditions, dispersions of highly charged, monodisperse, sub-micrometer sized colloidal particles can self-assemble into a variety of crystalline structures as a result of interparticle screened Columbic repulsion. This method has very strict requirements on the experimental conditions: such as temperature, size monodispersity, density of charges on the surface of each sphere, number density of spheres, and concentrations of counterions in the dispersion medium.

(3) Self-Assembly under Physical Confinement[50-53]:

Monodispersed colloidal spheres often organize themselves into a highly ordered 3D structure when they are subjected to a physical confinement. In this method, colloidal particles are assembled into a highly ordered structure in a specially designed packing cell. Usually, a pushing force is applied to speed the particle filling process. Shaking is also provided to the system to make sure the particles tightly packed. This method is relatively fast, and it also provides a tight control over the surface morphology and the number of layers of the crystalline assemblies.

(4) Actually, with some modifications or finer control of experimental conditions, most of the methods used in the 2D colloid array assembly (solvent evaporation, electrophoretic deposition,

electrostatic interaction, optical manipulation, template-assistant assembly, lock-and-key interactions, and covalent interactions) can also be used in the fabrication of 3D colloidal particle nanostructure.

As a summary, the methods of colloidal particle assembly in 2D and 3D mentioned above are listed in Table 1-1. Their advantages and disadvantages are given.

Table 1-1. Methods of colloidal particle assembly in 2D and 3D.

Methods	2D or 3D	Advantages	Disadvantages
Solvent evaporation	2D, 3D	Simple, fast, cheap	Limitation in substrate choice
Langmuir film technique	2D	Good for any substrate by film transfer	Needs special modification of colloidal particles, and finely control of pH and concentration
Sedimentation	3D	Simple, cheap	Slow, special requirement of particle size and density, hard to control number of layers, incapable of regular structural assembly
Electrophoretic deposition	2D, 3D	Simple, fast, capable of regular structural assembly	Particles have to be charged or dipolar
Electrostatic interaction	2D, 3D	Simple, capable of regular structural assembly	Limitation in substrate choice, quality of assembly needs to be improved
Optical manipulation	2D, 3D	Remote, sterile, precise, good for biological applications	Expensive, slow, hard for bulk or complicate structure assembly
Physical confinement	3D	Fast, cheap, high quality crystal, no requirement of particle composites, control of number of layers	Incapable of structural assembly, specially designed packing cells required.
Template-assisted Assembly	2D, 3D	Simple, fast, cheap, no requirement of particle composites, capable of regular structural assembly	Short in study of the fixation and transfer of assembled structures
Lock-and-key interactions	2D, 3D	Specific (good for biosensor building), working for either on substrate or in solution	Hard to control the growth of the assembly structure
Covalent interactions	2D, 3D	Specific, strong binding, capable of regular structural assembly	Requirement in the particle and surface head groups, quality of assembly
In situ particle formation and fabrication	2D	Capable of structural assembly, good for salt crystal formation and assembly	Limited application area
Electrostatic Interactions	3D	Capable of controlling crystalline structures	Strict requirements of the experimental conditions

1.1.3. Potential applications of 2D and 3D colloidal particle assembly

The easily controlled intrinsic properties (material, surface modification, and size) of ordered colloidal particle arrays lead to many promising potential applications, ranging from new materials in engineering to new devices in electronics, optics, chemistry, physics and biology. Some of the important applications of colloidal assembly are listed in Table 1-2.

Table 1-2. Some important applications of colloidal assembly

Applications	Remark
Masks for photolithography and softlithography[54,55]	Quite inexpensive and relatively easily reproduced masks. However, limited in number of structures
Sensor arrays	(1) Biosensors: relying upon the inherent selectivity of enzymes or antibodies[56,57]; (2) Optical sensors[58,59]: relying upon the optical dielectric constant modulation
Catalyst arrays	Higher efficiency in catalysis due to bigger effective surface area. *e.g.* Electroless deposition of metal[60].
Templates for macroporous materials[61-63]	Good for a wide variety of materials. The size of pores and the periodicity of the porous structures can be precisely controlled. Very broad applications.
Electrical, optical components and devices	Single electron transistor[64], light-emitting diode[65], grating[66], filter[67], switch[68], arrays of microlenses[69], high density optical memory devices[70], Photonic bandgap structures[71,72]
Model systems of fundamental phenomena	Crystallization[73]; Phase Transition[74]; Fracture mechanics[75];
Precursors for high strength ceramics	Ceramic materials are produced as uniform colloidal particles and subsequently crystallized into closely packed lattices so that all grains and pores are the same size[76]

For many of the above-named applications, it is desirable to control the position distribution of colloidal particles in 2D and 3D fabrication to obtain geometries of interest for sensors and devices. In other words, one must assemble the particles into a pre-designed architecture.

1.2. A brief introduction to Atomic Force Microscopy (AFM)

A brief introduction to atomic force microscopy is given here because AFM has been used extensively in my work.

The Atomic Force Microscope (AFM) is used to investigate material properties based on the probe technique. It is one member of the family of scanning probe microscopes (SPMs).

1.2.1. The basic construction of AFM

The basic construction of an AFM consists of several major parts: a scanning piezoelectric stage, a cantilever with a sharp tip, a laser beam source, a photon detector, a controller, and output displays, see Figure 1-5.

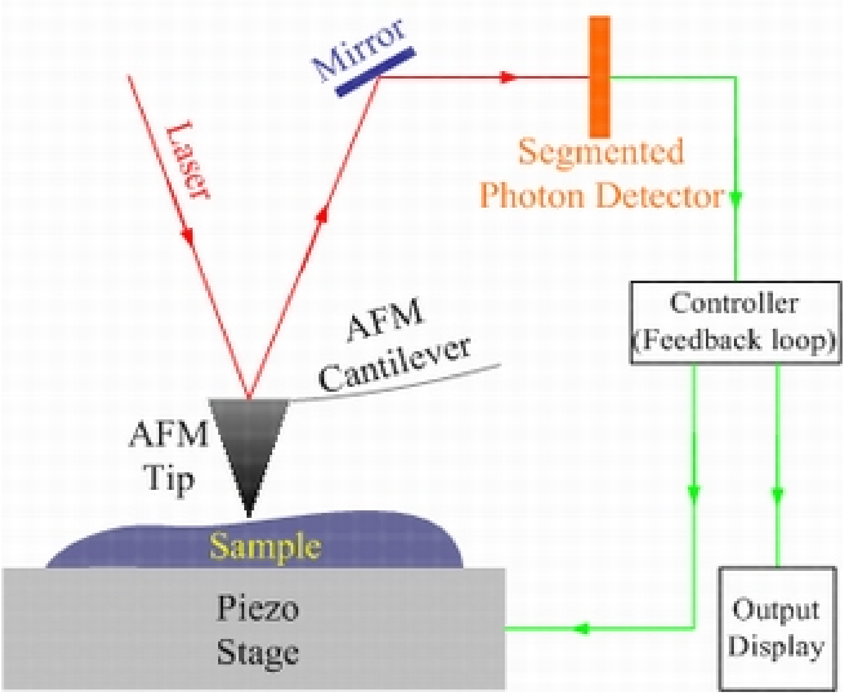

Figure 1-5. The basic construction of AFM. See text for details.

Generally, the cantilever with a sharp tip at its free end is brought down to interact with the sample underneath. A laser beam shines down on the backside of the cantilever and is reflected back to the photon detector. Any interaction change between the tip and the sample results in a change of bend of the cantilever, and this tiny change is magnified through the optical deflection by many thousand folds. The quadrant photon detector converts the optical deflection signal to an electronic signal and records the lateral and vertical changes of the tip position. The controller has a feedback loop. It takes the signal from the photon detector, and adjusts the piezoelectric stage accordingly based on a pre-assigned value of the feedback signal. Meanwhile, the signals are output to the display. For most commercial AFM systems, the vertical resolution is smaller than 0.1 nm, and the lateral resolution is about 1 nm.

1.2.2. The forces commonly involved in AFM

An AFM tip senses different interactions between the tip and the sample at different length scales as shown in Figure 1-6a. Figure 1-6b shows how the interaction force depends on the tip-sample separation based on a Lennard-Jones potential. The tip senses the repulsive force in the contact region, and attractive force in the non-contact region. Generally, AFM senses van der Waals interaction and short-range electrostatic interaction.

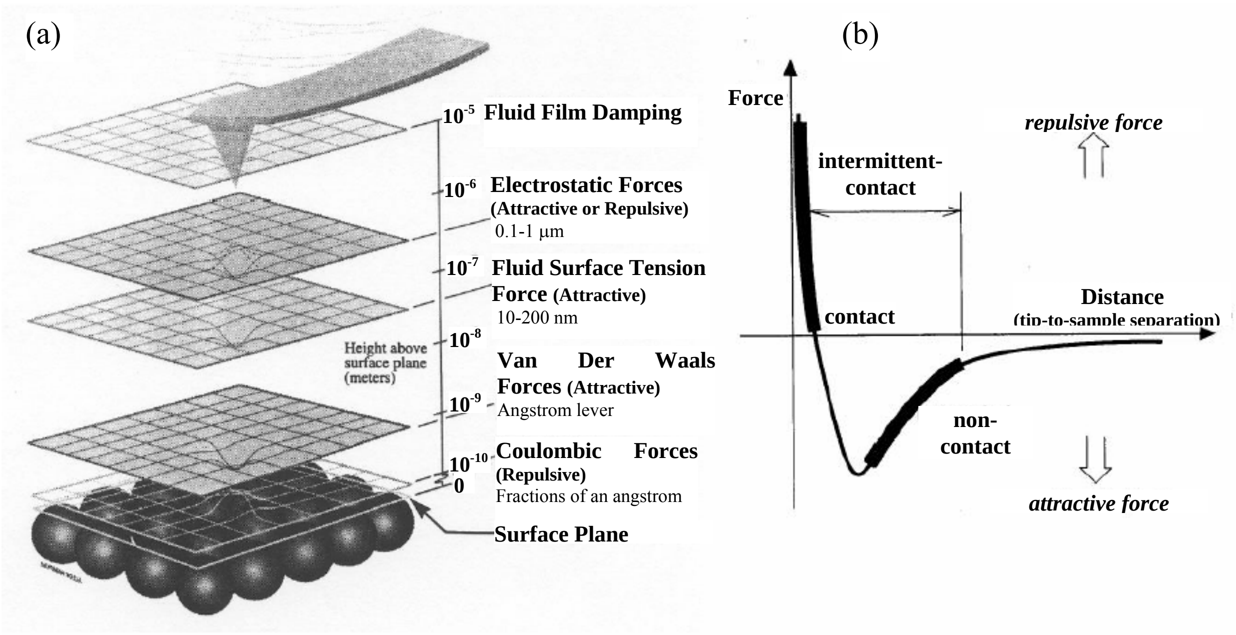

Figure 1-6. (a) The forces commonly involved in the tip-sample interaction of AFM; (b) The interaction force versus the tip-sample separation based on a Lennard-Jones potential.

1.2.3. The common scanning modes of AFM

Imaging mode:

Contact mode and tapping mode are the two common imaging modes of AFM. In both modes, via a feedback loop, a constant tip-sample interaction force (or a constant feedback signal) is maintained by extending or retracting the piezoelectric stage according to the variation of the sample properties, such as topography, stiffness, adhesion, charge density. Thus, many different material properties can be measured with the imaging modes. The most often measured material properties with AFM imaging modes are topography, friction, electric field, magnetic field, surface potential distribution, and phase contrast (based on adhesion, viscoelasticity, etc.). Some of them need special modification of AFM tips. AFM is very useful in biological imaging because it can be done both in ambient and liquid environments.

In contact mode, a tip is scanned across the sample while a feedback loop maintains a constant cantilever deflection (and force), see Figure 1-7a. The force constants of contact mode cantilevers usually range from 0.01 to 1.0 N/m, resulting in forces ranging from nN to µN in an ambient atmosphere.

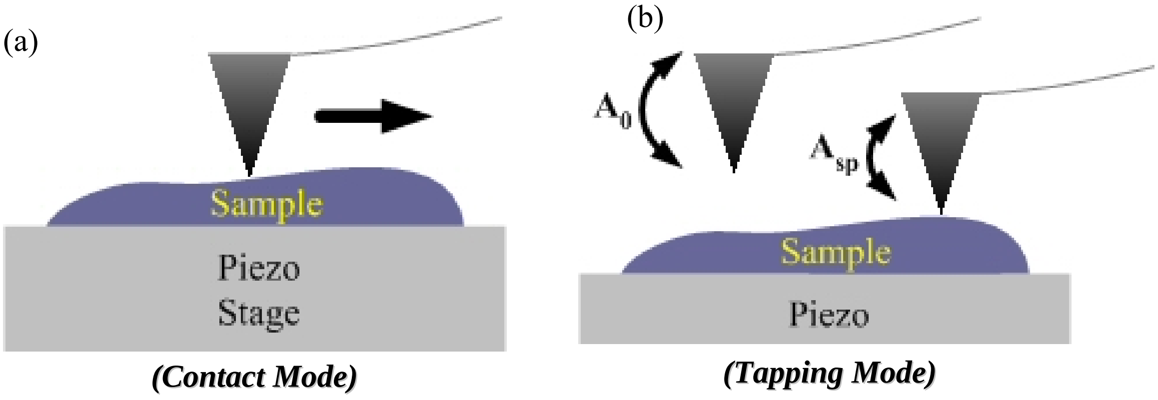

Figure 1-7. The two common AFM imaging modes. (a) Contact mode; (b) Tapping mode. A_0 is the amplitude of the cantilever in air, while A_{sp} is the constant amplitude of the cantilever maintained during the tapping mode imaging.

In tapping mode, a cantilever is oscillated with amplitude A_0 at or near its resonance frequency in the absence of the tip-sample interaction. When scanning across the sample surface. the tip lightly “taps” on the sample surface at the bottom of the cantilever swing with a setpoint (constant) oscillation amplitude A_{sp} smaller than A_0, see Figure 1-7b. Typical amplitudes of the cantilever are 20-100 nm.

Contact mode and tapping mode both have their advantages and disadvantages. Therefore, the choice of contact mode or tapping mode depends on what is preferred in the experiments. Under the same condition, high scan speeds can be achieved with contact mode, while tapping mode usually scans slower. The tip radius of an AFM tip is usually about 10-50 nm, which means that AFM can hardly obtain “atomic resolution” images. However, with the sub-nanometer sized asperities on the tip apex, contact mode AFM can obtain "atomic resolution" images under proper condition. Worthwhile noted is that nowadays robust ultrasharp tips with 1 nm tip radii have been made, so tapping mode can also achieve images with atomic resolution. The disadvantages of contact mode are obvious. When applied to image soft or tender samples, such as most biological and polymeric samples, the lateral (shear) forces in contact mode can distort features in the image, or even damage the samples due to scraping between the tip and sample. In tapping mode, the lateral forces are virtually eliminated, so it is widely used in the study of biological samples.

One extremely useful extension of tapping mode is phase imaging. Phase imaging is based on the measurement of the phase lag of cantilever oscillation relative to the piezoelectric driving oscillation, see Figure 1-8a. The phase lag is determined by the energy dissipation of the tip-sample interaction, which is a function of viscoelasticity, friction, and adhesion of samples. Therefore, phase imaging can provide information about composition, adhesion, friction, and viscoelasticity beyond simple topographical mapping. This is especially useful to detect local property variations of a sample without topographical contrast. Figure 1-8b is a phase image of E. coli cells on the tertiary amino group-quaternized glass[77].

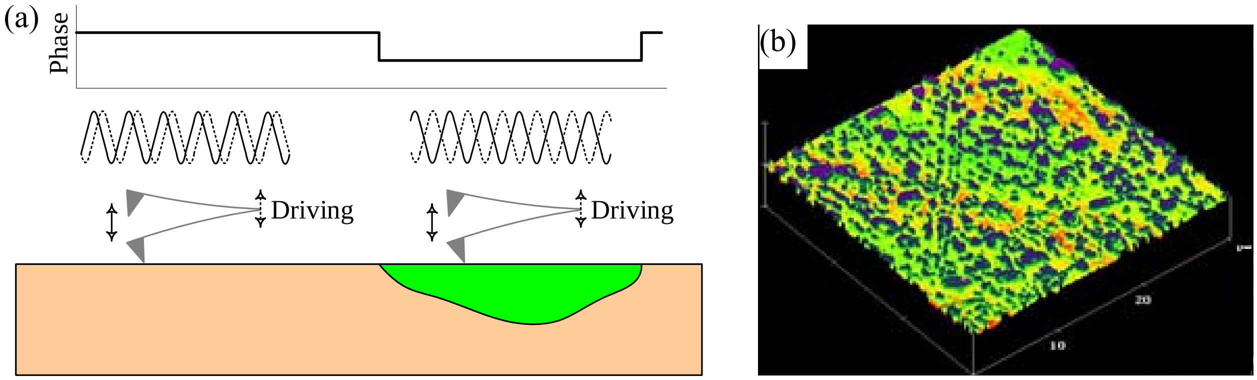

Figure 1-8. (a) Phase imaging is based on the measurement of the phase lag of cantilever oscillation relative to the piezoelectric driving oscillation; (b) a phase image of E. coli cells on the tertiary amino group-quaternized glass[77].

Force mode:

Another important scan mode of AFM is the force mode. In the force mode, the AFM tip is brought down into contact with a sample then pulled off, and the force versus distance curves (usually called force plots or force curves) are recorded.

Figure 1-9b shows the process schematically, and Figure 1-9a is the corresponding force plot.

First, the tip approaches to the surface as state 1 in Figure 1-9b. In Figure 1-9a, it is from right to left. In this range, the tip senses long range attractive or repulsive forces. As the probe tip is brought very close to the surface (usually several nm), it may jump into contact on the surface if the attractive force from the sample is sufficient. This state is shown as the state 2-3 Figure 1-9a and 1-9b.

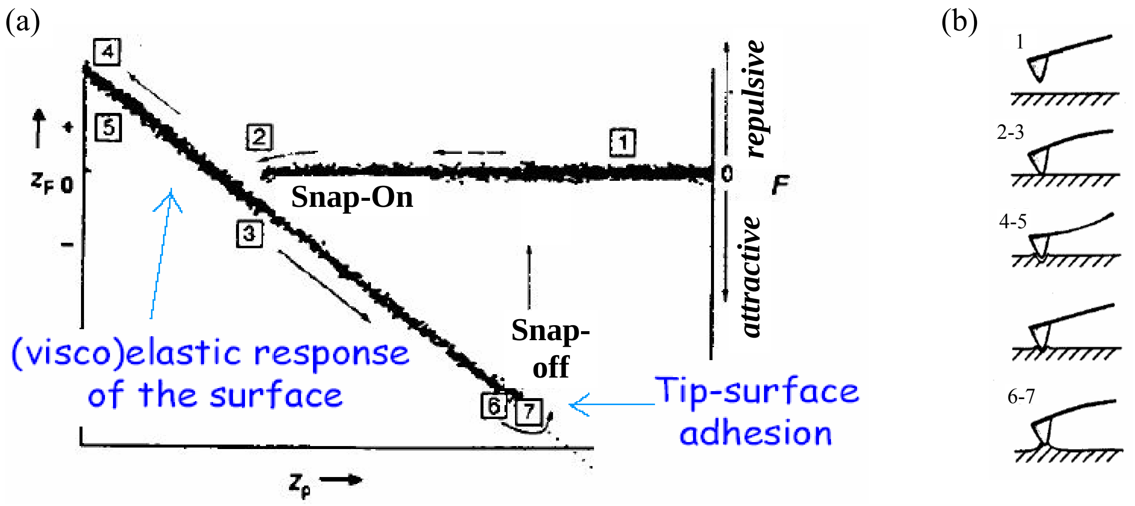

Figure 1-9. (a) A typical AFM force plot; (b) The states of the AFM tip correspond to the force plot in (a) schematically[78].

After the tip jumps into contact with the surface, the fixed end of the cantilever is brought closer to the sample surface, and the cantilever deflection increases as a result of the increased repulsive force between the tip and the sample. This corresponds to the state 4-5 in Figure 1-9. In this state, if the cantilever is sufficiently stiff, the tip can indent into the surface and the corresponding force plot may show a nonlinear curve. In this case, the slope or shape of the contact part of the force curve can provide information about the elasticity of the sample surface.

At a desired loading force value, the process is reversed and the cantilever deflection decreases. Because of the adhesion or bonds formed during contact with the surface, the tip may adhere to the sample some distance past the initial contact point on the approach curve. This can be used to measure the rupture force required to break the bond or adhesion, see state 6-7 in Figure 1-9. After the contact ruptures, the AFM tip jumps back to its free state.

AFM force mode is extensively used in two categories. One is the force volume imaging, which is used to investigate spatial variation of surface properties for an inhomogeneous sample, or provide statistical analysis of surface properties of a homogeneous sample. The other one is force spectrum which is mainly used in single molecule studies.

In force volume imaging, a scanning area is divided into an array, and one force plot is measured at each pixel. Force plots collected at all pixels are combined into a three-dimensional array, called a force volume, see Figure 1-10a. Meanwhile, the corresponding topographic data at each pixel point are also measured and shown as a topographic image. Figure 1-10b shows the elasticity mapping of MDCK cells using AFM force volume imaging technique[79]. The elasticity mapping may identify rearrangements of cytoskeletal elements and other cellular components.

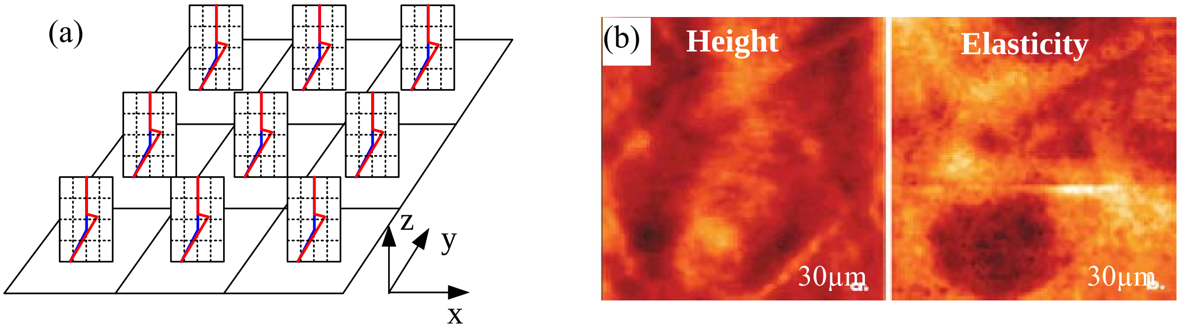

Figure 1-10. (a) AFM force volume imaging: a scanning area is divided into an array, and one force plot is measured at each pixel. Force plots collected at all pixels are combined into a three-dimensional array, called a force volume; (b) Elasticity mapping of MDCK cells using AFM force volume imaging technique[79].

In single molecule force spectrum mode, an AFM tip (usually chemically functionalized) is brought down to pick up single macromolecules, such as polymer chains, DNAs, and proteins. The force versus tip-sample separation is recorded. When combined with single molecule imaging, single molecule force spectroscopy provides unprecedented possibilities to analyze intra- and intermolecular forces. It is widely used in study of elastic property, energy barriers of conformational change of single macromolecules, as well as ligand-binding studies[80-86]. Figure 1-11 gives an example of unfolding single titin molecule fragment[85]. A titin molecule tethered between the cantilever tip and a gold substrate. As the cantilever retracted from the surface, the force on the molecule increased until a domain unfolded. The analysis of the force spectrum can provide the contour length and unfolding energy barrier of protein domains.

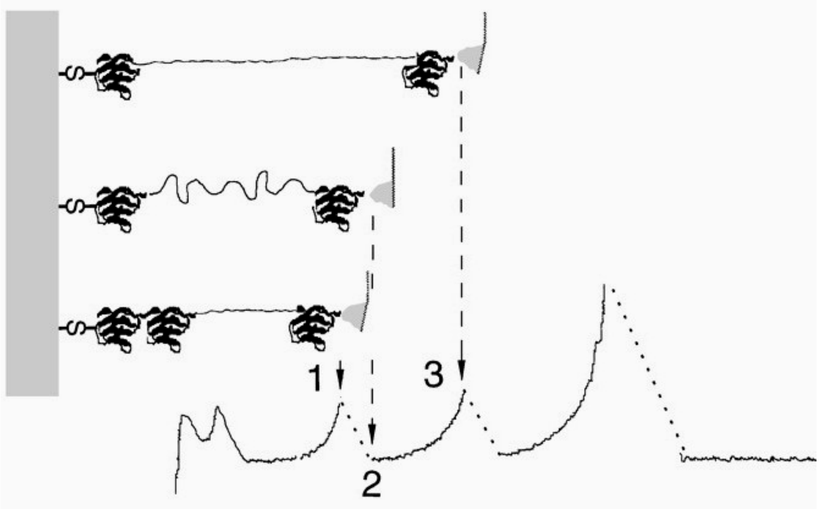

Figure 1-11. This figure shows a possible sequence of events. (1) An Ig4, covalently attached to the gold surface, is picked up by adsorption by an AFM tip. As the AFM tip is retracted, the domains unfold. The sawtooth pattern results from the sequential unfolding of Ig domains, which are mechanically in series. Before a domain unfolds, the extended polypeptide will be stretched until a holding force of 150 to 300 pN is reached and unfolding becomes highly probable. (2) Unfolding of an Ig domain abruptly reduces the holding force because of an increase in the length of the extended polypeptide by 25 nm. (3) Continued retraction of the AFM tip again stretches the extended polypeptide until a force is reached where the next Ig domain unfolds. When a domain unfolds, the AFM tip snaps back 2 to 4 nm into its resting position. This leaves a blind window in the force curve within which no structure of the unfolding process can be observed[85].

1.2.4. The characterization of AFM cantilevers and probes

Calibration of force constants of AFM cantilevers:

Although manufactures usually provide nominal force constant values for their AFM tips, sometimes it is necessary to know a more accurate value of the cantilever force constant. For instance, some AFM experiments, such as single molecular force microscopy, measurement of interfacial forces and force in indentation require precisely controlling or determining the force in AFM experiments.

There have been several popular methods available for the force constant calibration of AFM cantilevers. They are either based on cantilever resonance static loading on cantilever. All methods are accurate to about 10-20%. In Cleveland's method[87], a tungsten particle is attached to the tip of the cantilever purely via a capillary force. The cantilever force constant can be obtained based on the shift of the cantilever resonance frequency before and after the load of tungsten particle. Cleveland's method is the gold standard in cantilever calibration because of its high accuracy. Sader's method[88] is solely based on the measurement of the resonant frequency and dimensions of the cantilever. It has good accuracy, but is only applicable to cantilevers with a rectangle shape. Hutter's method[89] is based on thermal fluctuation of the cantilever. The method is simple and highly non-destructive. However, it is only applicable to weak cantilevers. Torii's method[90] uses a reference cantilever to calibrate the force constant of another cantilever. It is the simplest method, but most destructive.

Table 1-3. Several popular methods for the calibration of cantilever force constant

Method	Cleveland's Method	Sader's Method	Hutter's Method	Torii's Method
Principles	Added Mass + Shift Resonance Frequency of the cantilever	Resonance curve + Dimension of the cantilever	Thermal noise of the cantilever	Reference cantilever method
Advantage	Accurate; works for all cantilevers	Works for both high k and low k cantilevers	Works for cantilevers with different geometry	Easy to perform; Quick
Dis-advantage	Hard to perform; Time consuming	Works only for rectangular cantilever	Extra electronic equipment; Only works for weak cantilever	Destructive to tip

Calibration of the tip radius:

In some applications, such as AFM nano-indentation and conductive AFM, tip radius must be precisely known. There are basically three methods to determine the AFM tip radius. The most straightforward but most time and cost consuming method is to image the AFM tip using an electron or a field ion emission microscope. For most AFM tips, this method might require a conductive coating applied to the tip, which actually damages the tip somewhat. The second method is based on some “tip characterizer”, which has a known shape and small size relative to the tip. A wide assortment of such tip characterizers, such as colloidal gold, DNA, and some manufactured structures, are available[91-95]. In this method, the AFM tip is actually imaged by the sharper or smaller “tip characterizer”. The third method is called "blind" method[96-100]. It allows the determination of the entire complex 3D-shape of the tip from the image alone and without the need of using a known tip characterizer.

1.2.5. The modification of AFM probes

Chemical functionalization:

Functionalization of AFM tips by coating them with molecules has provided unprecedented possibilities for studying specific interactions on a molecular level.

Usually, functionalized silanes or thiols are used in the chemical coating of probes as a first step for further biological functionalization. Coating molecule with different hydrophobicity can be used to probe local variation of sample hydrophobicity by the chemical force microscopy[101,102].

Biological coating, such as protein, DNA, has been widely used in mapping the distribution of binding partners on samples and single molecule force measurements. Although passive, non-specific binding is enough to coat proteins on AFM tips, many protocols have been proposed to attach proteins on AFM tips via covalent bonds. Coating via covalent bonds has two advantages: one is that the biological coating is robust, and second is that it is possible to orient the protein in order to expose specific site of the proteins. The covalent binding of biological molecule on an AFM is usually obtained via a spacer such as polyethyleneglycol (PEG). Typically, a terminal thiolated or silanized PEG first binds to a gold coated tip (for thiol-PEG) or a silicon nitride tip (for silane-PEG). The other end of the PEG is designed to bind proteins covalently[103-106].

Attaching particles to AFM cantilevers:

Attaching particles to AFM cantilevers is useful in several ways. First, particles have simple known shape, which simplifies the analysis of some fundamental tip-sample interaction forces[107-112]. Second, types of particle material are much more than AFM tip material, so chemical modification on attached particle is much more simple and versatile than that on regular AFM tips[113]. This is especially true for polymeric particles.

Particles are usually glued to the end of the cantilever. A fine wire attached to a three-dimensional translational stage is usually used to transport a particle. In my experiment, I used the Dimension 3100 AFM to attach particles to cantilevers, see Figure 1-12a.

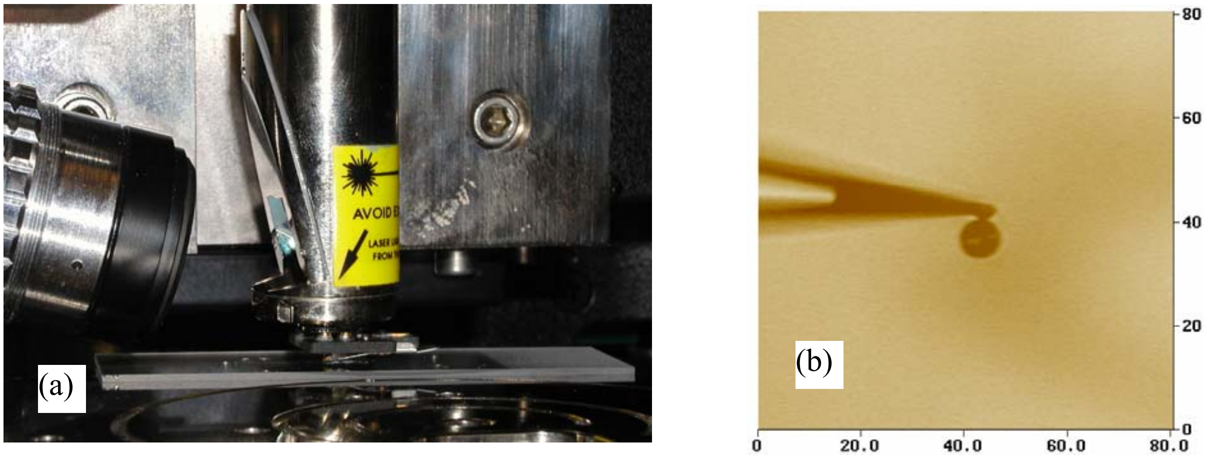

Figure 1-12. (a) The AFM-based setup for attaching particles to cantilevers; (b) A 5 μm polystyrene particle is attached to the end of the cantilever.

To do so, first, a tiny amount of particles are spread on a flat glass surface. Second, a cantilever is put in the tip holder and the AFM is set up for regular scanning. Third, a piece of thin epoxy glue (5-minute epoxy) is written on the glass slide by a sharp toothpick. The cantilever is then brought down to pick up a little bit of glue and quickly moved back to glue up the pre-located particle, see Figure 1-12b. All these procedures can be observed under the integrated optical microscope.

1.3. A basic introduction to elasticity and viscoelasticity

The elasticity and viscoelasticity of a macroscopic object are usually described by stress and strain[114,115].

Stress is defined as the applied force divided by the area of the material where the force is applied, see Figure 1-13a. Strain is defined as the fractional change of dimension of the object under a stress, see Figure 1-13b.

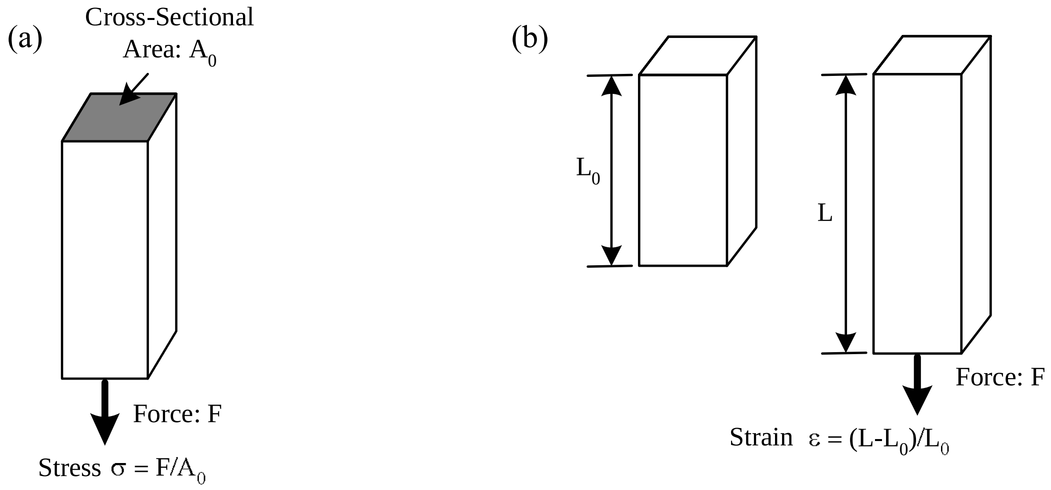

Figure 1-13. (a) Stress is defined as the applied force divided by the area of the material where the force is applied; (b) Strain is defined as the fractional change of dimension of the object under a stress.

The ratio of the stress to the strain is the modulus, which depends on the material and the deformation. There are different kinds of moduli, such as Young's modulus, shear modulus and bulk modulus. This thesis will concentrate on Young's modulus (also called elasticity). Young's modulus is the mechanical resistance of a material while elongating or compressing. It has the units of force per surface area.

If a material is purely elastic under a certain strain, the material will always regain its original form if no more force is applied. This elastic response can be modeled by a Hookean spring, for which the stress and strain are linearly related. The Young's modulus of an elastic material is a constant independent of stress and time as given in Equation (1-1). Under a constant stress over time, the strain is also a constant, see Figure 1-14a.

$$\sigma = E \cdot \varepsilon \tag{1-1}$$

where σ is the stress, ε is the strain, and E is the Young's modulus.

The opposite of a purely elastic response is purely viscous. A viscous response can be modeled by a Newtonian dashpot, for which the stress and strain are dependent on time as given in Equation (1-2). Under a constant stress over time, strain increases linearly, see Figure 1-14b.

$$\sigma = \eta \frac{d\varepsilon}{dt} \tag{1-2}$$

where η is the viscosity.

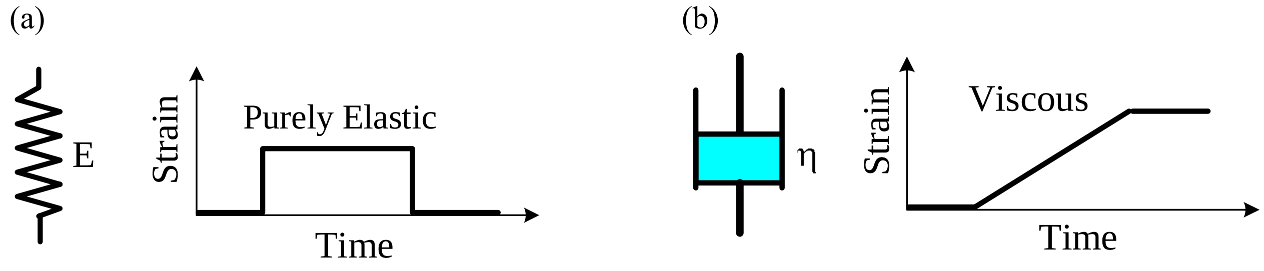

Figure 1-14. (a) An elastic response can be modeled by a Hookean spring, for which the stress and strain are linearly related. The Young's modulus of an elastic material is a constant independent of stress and time. Under a constant stress over time, the strain is also a constant; (b) A viscous response can be modeled by a Newtonian dashpot, for which the stress and strain are dependent on time. Under a constant stress over time, strain increases linearly.

Most real materials show both elastic and viscous properties, jointly named the viscoelasticity of materials. The viscous term leads to energy dissipation, while the elastic term leads to energy storage.

For a viscoelastic material under a constant stress (or strain) over time, the strain (or stress) varies in a non-linear behavior. These phenomena are called creep (for constant stress) and stress relaxation (for constant strain), see Figure 1-15.

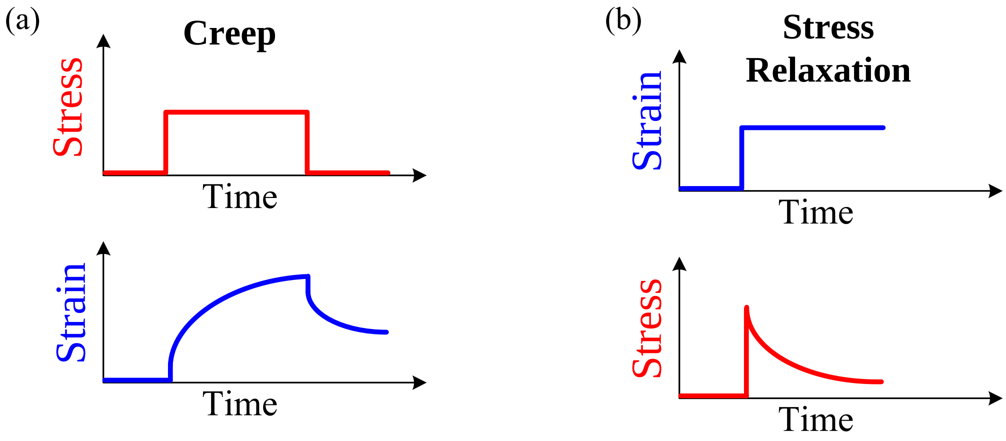

Figure 1-15. For a viscoelastic material under a constant stress (or strain) over time, the strain (or stress) varies in a non-linear behavior. (a) Creep of strain under a constant stress); (b) Stress relaxation under a constant strain.

Usually, at the moments of loading or unloading of stress, there are instantaneous responses of strains, as seen in Figure 1-15a. The strain increases nonlinearly under a constant stress. When the stress is removed, a residue strain may be left as a result of permanent deformation. The creep can be modeled by the Kelvin-Voight model[116], in which a spring and a dashpot are combined in parallel, see Figure 1-16a. Under a constant strain over time, stress decreases nonlinearly, the decay of the stress (stress relaxation) can be modeled by the Maxwell model[116], in which a spring and a dashpot are combined in series, see Figure 1-16b.

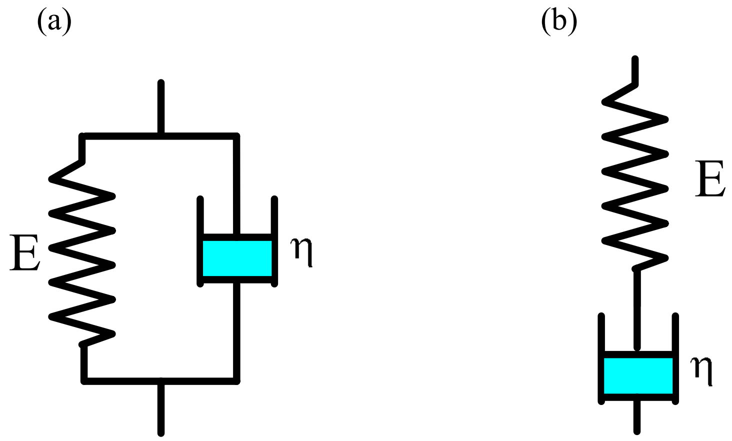

Kelvin-Voight model Maxwell model

Figure 1-16. Models for describing creep and stress relaxation. (a) Kelvin-Voight model; (b) Maxwell model.

For Kelvin-Voight model, the time dependent stress and strain are given by Equations (1-3a) and (1-3b):

$$\sigma = E\varepsilon + \eta \frac{d\varepsilon}{dt} \tag{1-3a}$$

$$\varepsilon(t) = \frac{\sigma}{\eta}\left[1 - \exp(Et/\eta)\right] \tag{1-3b}$$

For Maxwell model, the time dependent stress and strain are given by Equations (1-4a) and (1-4b):

$$\frac{d\varepsilon}{dt} = \frac{1}{E}\frac{d\sigma}{dt} + \frac{\sigma}{\eta} \tag{1-4a}$$

$$\sigma(t) = \sigma_0 \exp(-Et/\eta) \tag{1-4b}$$

In fact, both Kelvin-Voight and Maxwell models are too simple to describe real viscoelastic materials. A viscoelastic material shows a dynamic modulus under an external perturbation. It presents effectively hard initially and softens over time. The two elastic limits are E_0 for the instantaneous modulus at the start of the external perturbation and E_∞ for the relaxed modulus over a long term. For instance, the modulus relaxation of cross-linked polymers is usually described by constitutive models for linear viscoelasticity, in which springs and dashpots are combined in serial or parallel and multiple characteristic times can exist in one material. There are many different such constitutive models. For example, an extended Zener model[116] is given in Figure 1-17.

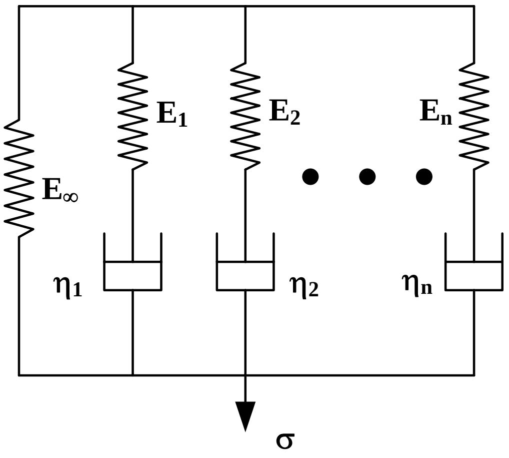

Figure 1-17. Extended Zener's model. E_∞ is the relaxed modulus over a long time, E_i and η_i are the modulus and viscosity of the ith viscoelastic component, and σ is the stress.

The time-dependent elasticity of Zener's model is accumulation of the relaxation modulus of each component as give below

$$E_r(t) = E_\infty + \sum_{i=1}^{n} E_i \exp(-\frac{E_i}{\eta_i} t) \tag{1-5}$$

where $E_r(t)$ is the relaxed modulus at time t, E_∞ is the relaxed modulus over a long time, and E_i and η_i are the modulus and viscosity of the *i*th viscoelastic component, respectively. η_i/E_i is the characteristic time of the *i*th viscoelastic component.

1.4. Measuring surface elasticity with the AFM indentation method

As a kind of deformation, indentation under an external load can be used to deduce the mechanical properties of material, such as elasticity, plasticity, and yield strength, with the knowledge of the contact shape and loading force.

Nanoindentation is a conventional method for measuring elastic moduli of materials. Usually, a hard microindenter, such as a diamond tip, is used to indent into the tested sample under a controllable loading rate. The conventional nanoindentation instrument has relatively poor load resolution, typically not better than ± 100 nN. The smallest maximum loads applied in practice are typically tens of micronewtons to reduce the relative uncertainties in load and penetration depth. Thus, this method has been mostly used in the study of hard materials, such as metals and ceramics. In addition, this method has limited capabilities for studying viscoelastic materials such as polymers and biological systems. It has been reviewed by Vanlandingham et al.[117].

The emerging of AFM has made it possible to study the mechanical response of surfaces to forces with much better control of force and penetration depth[118-122]. Compared with other tools, AFM can probe local surface mechanical properties with much higher resolution, down to several tens of nanometers, and with much finer control of applied force, down to several nano-newtons. These two characteristics give AFM advantages over other tools for studying the mechanical properties of polymeric systems and biological systems because most of these systems have nano-scale heterogeneous modulus distribution.

The measurement of AFM tip indentation depth on a soft sample is given in Figure 1-18 schematically.

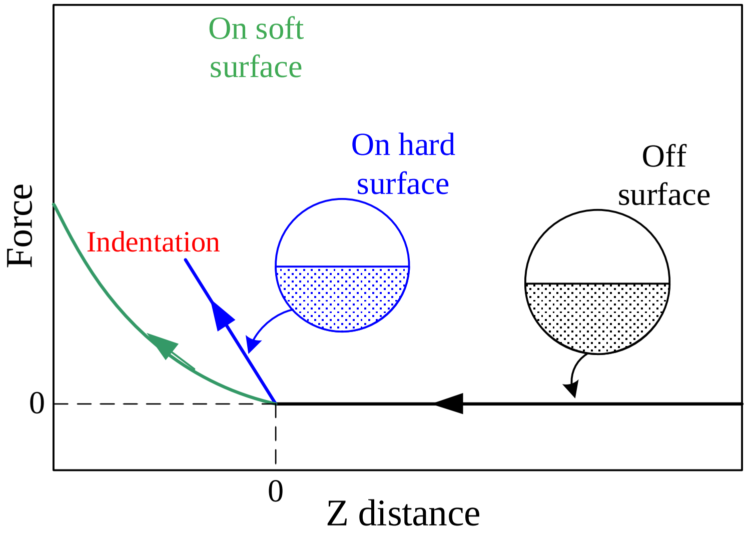

Figure 1-18. The AFM tip indentation depth is obtained from the difference in Z distance between the force curves of tip-on-hard surface and tip-on-soft surface.

In the figure, the x axis is Z distance, which is the relative displacement of the piezoelectric stage. The y axis is the tip-sample interaction force, which is converted from the cantilever deflection. When the tip is off surface, the force is zero. Once the tip comes into contact with the surface at the "0" point on x axis, the cantilever deflection starts to increase. If the sample surface is much stiffer than the cantilever spring, the force will increase linearly. If the sample surface is soft, the tip will penetrate into the sample, and the force will increase nonlinearly. The difference in Z distance between the two force curves at a certain force level is the indentation depth.

In AFM indentation experiments, the tip-sample interaction can be modeled as two springs in series. The displacement of piezoelectric stage ΔZ consists of both the cantilever deflection Δd and the penetration depth $\Delta\delta$ of the sample, as given in Equation (1-6).

$$\Delta Z = \Delta d + \Delta\delta \tag{1-6}$$

Note that when an AFM tip indents into a soft sample, the deformation of the tip is negligible because for Si_3N_4 tips, the Young's modulus is ~220 GPa and for commercial silicon cantilevers the Young's modulus is ~190 GPa[123].

The cantilever deflection and sample deformation are determined by the load *P* between the tip and sample and the effective force constants of the cantilever and the sample, respectively.

The load *P* between the tip and sample is obtained by Equation (1-7).

$$P = k_t \cdot \Delta d \tag{1-7}$$

where k_t is the force constant of the cantilever.

The sample deformation is related to the load, and the elastic modulus of the sample can be obtained from the load-penetration dependence. Hertz[124] first described the elastic deformation of two isotropic spheres in contact under external load as given in Equation (1-8),

$$a_0^3 = \frac{3}{4}\pi(k_1 + k_2)\frac{R_1 R_2}{R_1 + R_2}P_0 \tag{1-8}$$

where a_0 is the contact radius, R_1 and R_2 are the radii of the two spheres, P_0 is the external load, and k_1 and k_2 are the elastic constants of the material of each sphere; that is

$$k_1 = \frac{1-\nu_1^2}{\pi E_1} \quad \text{and} \quad k_2 = \frac{1-\nu_2^2}{\pi E_2}$$

where ν is the Poisson ratio and *E* is the Young modulus of each material.

The Hertz model was extended into contacts between objects of other geometries by Sneddon[125]. An AFM tip is usually in a conical shape or a paraboloid shape. According to the theories of Hertz and Sneddon, the elastic modulus of the sample can be obtained from Equation (1-9) for different tip shapes.

$$P = \frac{2E\tan(\alpha)}{\pi(1-\nu^2)}(\Delta\delta)^2 \qquad \text{(1-9a)}$$

$$P = \frac{4ER^{1/2}}{3(1-\nu^2)}(\Delta\delta)^{3/2} \qquad \text{(1-9b)}$$

where P is the loading force, $\Delta\delta$ is the depth of indentation, E is Young's modulus of the sample, and ν is the Poisson ratio of the sample. Equation (1-9a) is for a conical tip, whose tip semivertical angle is α; Equation (1-9b) is for a paraboloid tip, whose tip radius is R. In this model, the indentations are considered to be purely elastic, and the adhesion between tip and sample is neglected.

1.5. The Johnson, Kendall and Roberts (JKR) theory

In Hertz's theory, the surface attraction is not considered, *i.e.*, under zero load (P_0=0), there is a point contact between two elastic spheres (a_0=0), see Figure 1-19. In fact, when the load is reduced to zero or a negative value, the surface attraction force becomes very important. It results in a finite contact area under zero load. This is especially important for soft objects in contact.

Considering the surface attraction force, Johnson, Kendall and Roberts (JKR) proposed their famous JKR theory[126], see Figure 1-19. This model is based on an equilibrium energy balance, and assumes that the attractive forces are confined within the area of contact and are zero outside. Equilibrium will be obtained when

$$dU_T / da = 0 \qquad \text{(1-10)}$$

where a the contact radius of the contact area, and U_T is the total energy of the system, which consists of three terms: U_E (the stored elastic energy), U_M (the mechanical energy in the applied load), and U_S (the surface energy).

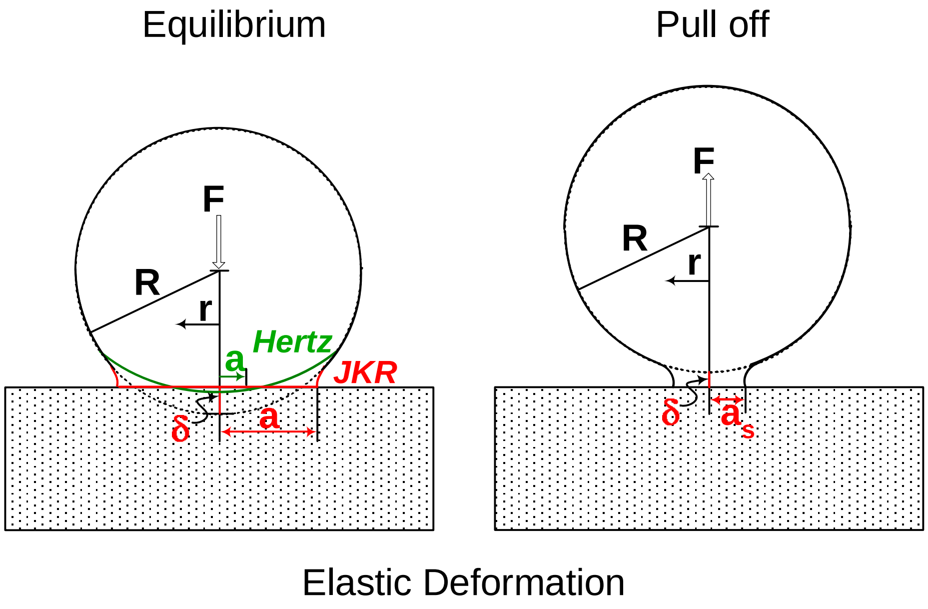

Figure 1-19. The elastic deformation predicted by the JKR model. *a* is the contact radius, R is the radius of the sphere, F is the external load, δ is the sample deformation.

The fundamental assumptions of the JKR theory are:

1. The deformations are elastic.
2. The contact radius and extension are small compared to the particle radius.
3. All interactions are localized within the contact region, *i.e.*, there are no long range interactions.

The JKR theory shows that the contact radius *a* is a function of both the external load and the interfacial energy as given in Equation (1-11).

$$a^3 = \frac{R}{K}\left(P_0 + 3\gamma\pi R + \sqrt{\{6\gamma\pi R P_0 + (3\gamma\pi R)^2\}}\right) \tag{1-11}$$

where P_0 is the external load, γ is the interfacial energy, $R=R_1R_2/(R_1+R_2)$ is the normalized radius of the two spheres with radius of R_1 and R_2 respectively, $K=4/3\pi(k_1+k_2)$. k_1 and k_2 are the elastic constants of each sphere as defined in Equation (1-8).

Under zero load ($P_0 = 0$), there is a finite contact area due to the interfacial adhesion. The contact radius a_0 is given by

$$a_0^3 = 6\gamma\pi R^2 / K \tag{1-12}$$

Under small negative loads (F<0) the particles still adhere until at some critical negative force the surfaces suddenly jump apart. The critical negative force is the adhesion or "pull off " force. It is

$$F_S = -\frac{3}{2}\gamma\pi R \tag{1-13}$$

and separation occurs abruptly once the contact radius has fallen to a_s

$$a_S = a_0 / 4^{1/3} = 0.63 a_0 \tag{1-14}$$

The central displacement δ is given by

$$\delta = \frac{a^2}{R}\left[1 - \frac{2}{3}\left(\frac{a_0}{a}\right)^{3/2}\right] \tag{1-15}$$

The pressure or stress distribution within the contact circle is

$$P(x) = \frac{3Ka}{2\pi R}\left(1 - x^2\right)^{1/2} - \left(\frac{3K\gamma}{2\pi a}\right)^{1/2}\left(1 - x^2\right)^{-1/2} \tag{1-16}$$

where x = r/a.

BIBLIOGRAPHY

1. Israelachvili, J. N., *Intermolecular and Surface Forces*. 2 nd ed. **1992**, London: Academic Press.

2. *Colloids and Colloid Assemblies : Synthesis, Modification, Organization and Utilization of Colloid Particles*, ed. F. Caruso. **2004**, Weinheim: Wiley - VCH.

3. Zhong, Z.;Gates, B.;Xia, Y. *Langmuir* **2000**, *16*, 10369-10375.

4. Rakers, S.;Chi, L. F.;Fuchs, H. *Langmuir* **1997**, *13*, 7121-7124.

5. Sastry, M.;Patil, V.;Mayya, K. S.;Paranjape, D. V.;Singh, P.;Sainkar, S. R. *Thin Solid Films* **1998**, *324*, 239-244.

6. Sides, P. J. *Langmuir* **2001**, *17*, 5791-5800.

7. Zheng, J. W.;Zhu, Z.;Chen, H.;Liu, Z. *Langmuir* **2000**, *16*, 4409-4412.

8. Yin, Y.;Lu, Y.;Gates, B.;Xia, Y. *J. Am. Chem. Soc.* **2001**, *123*, 8718-8729.

9. Ye, Y.-H.;Badilescu, S.;Truong, V.-V.;Rochon, P.;Natansohn, A. *Applied Physics Letters* **2001**, *79*, 872-874.

10. Hiemenz, P. C.;Rajagopalan, R., *Principles of colloid and surface chemistry*. **1997**, New York: Marcel Dekker, Inc.

11. Polysciences, Inc. *LifeScience catalog*, **2000-2001**, p. 167

12. Denkov, N. D.;Velev, O. D.;Kralchevsky, P. A.;Ivanov, I. B.;Yoshimura, H.;Nagayama, K. *Langmuir* **1992**, *8*, 3183-3190.

13. Dushkin, C. D.;Nagayama, K.;Miwa, T.;Kralchevsky, P. A. *Langmuir* **1993**, *9*, 3695-3710.

14. Lazarov, G. S.;Denkov, N. D.;Velev, O. D.;Kralchevsky, P. A.;Nagayama, K. *J. Chem. Soc., Faraday Trans.* **1994**, *90*, 2077-2083.

15. Dimitrov, A. S.;Nagayama, K. *Langmuir* **1996**, *12*, 1303-1311.

16. Kondo, M.;Shinozaki, K.;Bergstry, L.;Mizutani, N. *Langmuir* **1995**, *11*, 394-397.

17. Meldrum, F. C.;Kotov, N. A.;Fendler, J. H. *J. Phys. Chem.* **1994**, *98*, 4506-4511.

18. Kotov, N. A.;Meldrum, F. C.;Wu, C.;Fendler, J. H. *J. Phys. Chem.* **1994**, *98*, 2735-2740.

19. Larsen, A. E.;Grier, D. G. *Nature* **1997**, *385*, 230-233.

20. Gole, A.;Sainkar, S. R.;Sastry, M. *Chem. Mater.* **2000**, *12*, 1234-1239.

21. Taguchi, Y.;Kimura, R.;Azumi, R.;Tachibana, H.;Koshizaki, N.;Shimomura, M.;Momozawa, N.;Sakai, H.;Abe, M.;Matsumoto, M. *Langmuir* **1998**, *14*, 6550-6555.

22. Chen, K. M.;Jiang, X. P.;Kimerling, L. C.;Hammond, P. T. *Langmuir* **2000**, *16*, 7825-7834.

23. He, H. X.;Zhang, H.;Li, Q. G.;Zhu, T.;Li, S. F. Y.;Liu, Z. F. *Langmuir* **2000**, *16*, 3846-3851.

24. Xia, Y.;Rogers, J. A.;Paul, K. E.;G.M., W. *Chem. Rev.* **1999**, *99*, 1823-1848.

25. Hayward, R. C.;Saville, D. A.;Aksay, I. A. *Nature* **2000**, *404*, 56-59.

26. Trau, M.;A., S. D.;Aksay, I. A. *Science* **1996**, *272*, 706-709.

27. Yeh, S.-R.;Seul, M.;Shraiman, B. I. *Nature* **1997**, *386*, 57-59.

28. Solomentsev, Y.;Bomer, M.;Anderson, J. L. *Langmuir* **1997**, *13*, 6058-6068.

29. Boneberg, J.;Burmeister, F.;Schaefle, C.;Leiderer, P.;Reim, D.;Fery, A.;Herminghaus, S. *Langmuir* **1997**, *13*, 7080-7084.

30. Burns, M. M.;Fournier, J.-M.;Golovchenko, J. A. *Science* **1990**, *249*, 749-754.

31. Sun, Y.;Walker, G. C. *J. Phys. Chem. B* **2002**, *106*, 2217-2223.

32. Yin, Y.;Lu, Y.;Xia, Y. *J. Am. Chem. Soc.* **2000**, *123*, 771-773.

33. Yin, Y.;Xia, Y. *Adv. Mater.* **2001**, *13*, 267-270.

34. Huck, W. T. S.;Tien, J.;Whitesides, G. M. *J. Am. Chem. Soc.* **1998**, *120*, 8267-8272.

35. Velev, O. D.;Lenhoff, A. M.;Kaler, E. W. *Science* **2000**, *287*, 2240-2244.

36. Garcia, M. E.;Baker, L. A.;Crooks, R. M. *Anal. Chem.* **1999**, *71*, 256-259.

37. Colvin, V. L.;Goldstein, A. N.;Alivisatos, A. P. *J. Am. Chem. Soc.* **1992**, *114*, 5221-5225.

38. Grabar, K. C.;Smith, P. C.;Musick, M. D.;Davis, J. A.;Walter, D. G.;Jackson, M. A.;Guthrie, A. P.;Natan, M. J. *J. Am. Chem. Soc.* **1996**, *118*, 1148-1152.

39. Loweth, C. J.;Caldwell, W. B.;Peng, X.;Alivisatos, A. P.;Schultz, P. G. *Angew. Chem., Int. Ed.* **1999**, *38*, 1808-1812.

40. Andres, R. P.;Bielefeld, J. D.;Henderson, J. I.;Janes, D. B.;Kolagunta, V. R.;Kubiak, C. P.;Mahoney, W. J.;Osifchin, R. G. *Science* **1996**, *273*, 1690-1694.

41. Storhoff, J. J.;Mirkin, C. A. *Chem. Rev.* **1999**, *99*, 1849-1855.

42. Mirkin, C. A.;Letsinger, R. L.;Mucic, R. C.;Storhoff, J. J. *Nature* **1996**, *382*, 607-609.

43. Alivisatos, A. P.;Johnsson, K. P.;Peng, X.;Wilson, T. E.;Loweth, C. J.;Bruchez, M. P., Jr.;Schultz, P. G. *Nature* **1996**, *382*, 609-611.

44. Qin, D.;Xia, Y.;Xu, B.;Yang, H.;Zhu, C.;Whitesides, G. M. *Adv. Mater.* **1999**, *11*, 1433-1437.

45. Miguez, H.;Meseguer, F.;Liez, C.;Mifsud, A.;Moya, J. S.;Vaquez, L. *Langmuir* **1997**, *13*, 6009-6011.

46. Mayoral, R.;Requena, J.;Moya, J. S.;Liez, C.;Cintas, A.;Miguez, H.;Meseguer, F.;Vaquez, L.;Holgado, M.;Blanco, A. *Adv. Mater.* **1997**, *9*, 257-260.

47. Donselaar, L. N.;Philipse, A. P.;Suurmond, J. *Langmuir* **1997**, *13*, 6018-6025.

48. Weissman, M.;Sunkara, H. B.;Tse, A. S.;Asher, S. A. *Science* **1996**, *274*, 959-961.

49. Kamenetzky, E. A.;Magliocco, L. G.;Panzer, H. P. *Science* **1994**, *263*, 207-209.

50. Leiderer, P.;Palberg, T. *Phys. Rev. Lett.* **1997**, *79*, 2348-2351.

51. Park, S. H.;Qin, D.;Xia, Y. *Adv. Mater.* **1998**, *10*, 1028-1032.

52. Park, S.;Xia, Y. *Langmuir* **1999**, *15*, 266-270.

53. Gates, B.;Qin, D.;Xia, Y. *Adv. Mater.* **1999**, *11*, 466-469.

54. Burmeister, F.;Schefle, C.;Matthes, T.;Bihmisch, M. *Langmuir* **1997**, *13*, 2983-2986.

55. Roxlo, C. B.;Deckman, H. W.;Gland, J.;Cameron, S. D.;Chianelli, R. R. *Science* **1987**, *235*, 1629-1631.

56. Goodey, A., Lavigne, J. J., Savoy, S. M., Rodriguez, M. D., Curey, T., Tsao, A., Simmons, G., Wright, J., Yoo, S., Sohn, Y., Anslyn, E. V., Shear, J. B., Neikirk, D. P., and Mcdevitt, J. T. *J. Am. Chem. Soc.* **2001**, *123*, 2559-2570.

57. Velev, O. D.;Kaler, E. W. *Langmuir* **1999**, *15*, 3693-3698.

58. Holtz, J. H.;Asher, S. A. *Nature* **1997**, *389*, 829-831.

59. Holtz, J. H.;Holtz, J. S. W.;Munro, C. H.;Asher, S. A. *Anal. Chem.* **1998**, *70*, 780-791.

60. Hidber, P. C.;Helbig, W.;Kim, E.;Whitesides, G. M. *Langmuir* **1996**, *12*, 1375-1380.

61. Velev, O. D.;Tessier, P. M.;Lenhoff, A. M.;Kaler, E. W. *Nature* **1999**, *401*, 548-550.

62. Velev, O. D.;Jede, T. A.;Janbo, R. F.;Lenhoff, A. M. *Nature* **1997**, *389*, 447-449.

63. Holland, B. T.;Blanford, C. F.;Stein, A. *Science* **1998**, *281*, 538-540.

64. Klein, D. L.;Roth, R.;Lim, A. K. L.;Alivisatos, A. P.;Mceuen, P. L. *Nature* **1997**, *389*, 699-671.

65. Empedocles, S. A.;Norris, D. J.;Bawendi, M. G. *Phys. Rev. Lett.* **1996**, *77*, 3873-3877.

66. Zhao, Y.;Avrutsky, I.;Li, B. *Appl. Phys. Lett.* **1999**, *75*, 3596-3598.

67. Zhang, Q.;Li, X.;Shen, J.;Wu, G.;Wang, J.;Chen, L. *Mater. Lett.* **2000**, *45*, 311-314.

68. Asher, S. A.;Pan, G.;Kesavamoorthy, R. *MCLC S&T, Sect. B: Nonlinear Opt.* **1999**, *21*, 343-352.

69. Hayashi, S.;Kumamoto, Y.;Suzuki, T.;Hirai, T. *J. Colloid Interface Sci.* **1991**, *144*, 538-543.

70. Korolev, N. E.;Mokienko, I. Y.;Poletimov, A. E.;Shcheulin, A. S. *Phys. Status Solidi A* **1991**, *127*, 327-333.

71. Bertone, J. F.;Jiang, P.;Hwang, K. S.;Mittleman, D. M.;Colvin, V. L. *Phys. Rev. Lett.* **1999**, *83*, 300-304.

72. Mei, D.;Liu, H.;Cheng, B.;Li, Z.;Zhang, D. *Phys. Rev. B* **1998**, *58*, 35-40.

73. Murray, C. A.;Grier, D. G. *Am. Sci.* **1995**, *83*, 238-245.

74. Larsen, A. E.;Grier, D. G. *Phys. Rev. Lett.* **1996**, *76*, 3862-3865.

75. Skjeltorp, A. T.;Meakin, P. *Nature* **1988**, *335*, 424-426.

76. Calvert, P. *Nature* **1985**, *317*, 201-204.

77. Lee, S. B.;Koepsel, R. R.;Morley, S. W.;Matyjaszewski, K.;Sun, Y.;Russell, A. J. *Biomacromolecules* **2004**, *5*, 877-882.

78. Van Der Aa, B. C.;Michel, R. M.;Asther, M.;Zamora, M. T.;Rouxhet, P. G.;Dufrene, Y. F. *Langmuir* **2001**, *17*, 3116-3119.

79. A-Hassan, E.;Heinz, W. F.;Antonik, M. D.;D'costa, N. P.;Nageswaran, S.;Schoenenberger, C.-A.;Hoh, J. H. *Biophys. J.* **1998**, *74*, 1564-1578.

80. Bemis, J.;Akhremitchev, B. B.;Walker, G. C. *Langmuir* **1999**, *15*, 2799-2850.

81. Zlatanova, J.;Lindsay, S. M.;Leuba, S. H. *Prog. Biophys. Mol. Biol.* **2000**, *74*, 37-61.

82. Allen, S.;Chen, X.;Davies, J.;Davies, M. C.;Dawkes, A. C.;Edwards, J. C.;Roberts, C. J.;Sefton, J.;Tendler, S. J. B.;Williams, P. M. *Biochemistry* **1997**, *36*, 7457-7463.

83. Oberhauser, A. F.;Marszalek, P. E.;Erickson, H. P.;Fernandez, J. M. *Nature* **1998**, *393*, 181-185.

84. Oesterhelt, F.;Oesterhelt, D.;Pfeiffer, M.;Engel, A.;Gaub, H. E.;Muller, D. J. *Science* **2000**, *288*, 143-146.

85. Rief, M.;Gautel, M.;Oesterhelt, F.;Fernandez, J. M.;Gaub, H. E. *Science* **1997**, *276*, 1109-1112.

86. Rief, M.;Oesterhelt, F.;Heymann, B.;Gaub, H. E. *Science* **1997**, *276*, 1295-1297.

87. Cleveland, J. P.;Manne, S.;Bocek, D.;Hansma, P. K. *Rev. Sci. Instrum.* **1993**, *64*.

88. Sader, J. E.;Chon, J. W. M.;Mulvaney, P. *Rev. Sci. Instrum.* **1999**, *70*, 3967-3969.

89. Hutter, J. L.;Bechhoefer, J. *Rev. Sci. Instrum.* **1993**, *64*, 1868-1873.

90. Torii, A.;Sasaki, M.;Hane, K.;Okuma, S. *Meas. Sci. Technol.* **1996**, *7*, 179-184.

91. Ramirez-Aguilar, K. A.;Rowlen, K. L. *Langmuir* **1998**, *14*, 2562-2566.

92. S.Xu;M.F.Arnsdorf. *J. Microsc.* **1994**, *173*, 199-206.

93. Thundat, T.;Zheng, X.-Y.;Sharp, S. L.;Allison, D. P.;Warmack, R. J.;Joy, D. C.;Ferrell, T. L. *Scanning Microsc.* **1992**, *6*.

94. Bao, G. W.;Li, S. F. Y. *Talanta* **1998**, *45*, 751-757.

95. Baiker, A.;Atamny, F. *Surface Science* **1995**, *323*, 1314-1318.

96. Bukharaev, A. A.;Berdunov, N. V.;Ovchinnikov, D. V.;Salikhov, K. M. *Scanning Microscopy* **1998**, *12*, 225-234.

97. Villarrubia, J. S. *Metrology, Inspection, and Process Control for Microlithography XII, Proceedings of SPIE* **1998**, *3332*, 10-17.

98. Villarrubia, J. S. *J. Res. Natl. Inst. Stand. Technol.* **1997**, *3332*, 425-454.

99. Williams, P. M.;Shakesheff, K. M.;Davies, M. C.;Jackson, D. E.;Roberts, C. J.;Tendler, S. J. B. *J. Vac. Sci. Technol. B* **1996**, *14*, 1557-1562.

100. Dongmo, S.;Troyon, M.;Vautrot, P.;Delain, E.;Bonnet, N. *J. Vac. Sci. Technol. B* **1996**, *1552-1557.*

101. Lieber, C. M.;Vezenov, D.;Noy, A.;Sanders, C. *Microscopy and Microanalysis* **1997**, *3*, 1253-1254.

102. Noy, A.;Vezenov, D. V.;Lieber, C. M. *Annu. Rev. Mater. Sci.* **1997**, *27*, 381-421.

103. Willemsen, O. H.;Snel, M. M. E.;Werf, K. O. V. D.;Grooth, B. G. D.;Greve, J.;Hinterdorfer, P.;Gruber, H. J.;Schindler, H.;Kooyk, Y. V.;Figdor, C. G. *Biophys. J.* **1998**, *75*, 2220-2228.

104. Micic, M.;Chen, A.;Leblanc, R. M.;Moy, V. T. *Scanning* **1999**, *21*, 394-397.

105. Ros, R.;Schwesinger, F.;Anselmetti, D.;Kubon, M.;Schafer, R.;Plu-Kthun, A.;Tiefenauer, L. *Proc. Natl. Acad. Sci. USA* **1998**, *95*, 7402-7405.

106. Dammer, U.;Hegner, M.;Anselmetti, D.;Wagner, P.;Dreier, M.;Huber, W.;Guntherodt, H.-J. *Biophys. J.* **1996**, *70*, 2437-2441.

107. Ducker, W. A.;Senden, T. J.;Pashley, R. M. *Nature* **1991**, *353*, 239-241.

108. Biggs, S.;Mulvaney, P. *J. Chem. Phys.* **1994**, *100*, 8501-8505.

109. Biggs, S. *Langmuir* **1995**, *11*, 156-162.

110. Butt, H.-J. *J. Colloid Interface Sci.* **1994**, *166*, 109-117.

111. Vakarelski, I. U.;Toritani, A.;Nakayama, M.;Higashitani, K. *Langmuir* **2001**, *17*, 4739-4745.

112. Toikka, G.;Hayes, R. A. *J. Colloid Interface Sci.* **1997**, *191*, 102-109.

113. Yamamoto, S.;Ejaz, M.;Tsujii, Y.;Matsumoto, M.;Fukuda, T. *Macromolecules* **2000**, *33*, 5602-5607.

114. Serway, R. A., *Physics: for Scientists and Engineers*. **1982**, CBS College Publishing: London. p. 298-301.

115. Timoshenko, S. P.;Goodier, J. N., *Theory of Elasticity*. **1970**, London: McGraw-Hill.

116. Ward, I. M., *Mechanical Properties of Solid Polymers*. 2nd ed. **1983**, Chichester: Wiley.

117. Vanlandingham, M. R.;Villarrubia, J. S.;Guthrie, W. F.;Meyers, G. F. *Nanoindentation of Polymers: An Overview*. in *Advances in Scanning Probe Microscopy of Polymers. Macromolecular Symposia.* **2001**.

118. Vanlandingham, M. R.;Villarrubia, J. S.;Guthrie, W. F.;Meyers, G. F. *Macromol. Symp.* **2001**, *167*, 15-43.

119. A-Hassan, E.;Heinz, W. F.;Antonik, M. D.;Dcosta, N. P.;Nageswaran, S.;Schoenenberger, C.-A.;Hoh, J. H. *Biophys. J.* **1998**, *74*, 1564-1578.

120. Tomasetti, E.;Legras, R.;Nysten, B. *Nanotechnology* **1998**, *9*, 305-315.

121. Fraxedas, J.;Garcia-Manyes, S.;Gorostiza, P.;Sanz, F. *Proc. Natl. Acad. Sci. USA* **2002**, *99*, 5228-5232.

122. Pietrement, O.;Troyon, M. *J. Colloid Interface Sci.* **2000**, *226*, 166-171.

123. Cuenot, S.;Demoustier-Champagne, S.;Nysten, B. *Phys. Rev. Lett.* **2000**, *85*, 1690-1693.

124. Hertz, H. *J. Reine Angew. Math.* **1882**, *92*, 156.

125. Sneddon, I. N. *Int. J. Engng Sci.* **1965**, *3*, 47-57.

126. Johnson, K. L.;Kendall, K.;Roberts, A. D. *Proc. R. Soc. London, Ser. A* **1971**, *324*, 301-313.

Chapter 2. Two-Dimensional-Self-Assembly of Latex Particles in Wetting Films on Patterned Polymer Surfaces

Abstract

The 2D self-assembly of micrometer-size latex particles in wetting films on patterned polydimethylsiloxane (PDMS) polymer surfaces was studied. The dynamics of these processes were directly observed using an integrated zoom microscope and CCD camera. The direct observations revealed the particles are transported inside or toward the grooves of the pattern in the region where the liquid film is appropriately thin, and the particles self-assembly inside the grooves is caused by a lateral capillary force. Mechanisms for particle transportation and self-assembly are discussed.

2.1. Introduction

Particles self-assemble on surfaces by design or accident. For example, photonic crystals with unusual periodicities and hence properties can be grown from textured surfaces whose patterns template a lattice structure[1]. Bulk synthesis of functionalized nanoparticles can be enhanced by using a smooth but chemically patterned surface to bring the particles into proximity, also allowing connections between them to be controlled. Particle assembly also occurs spontaneously upon introducing surfaces into physiological solutions. For example, cells, larvae, and spores distribute onto patterned surfaces in ways that may influence inter-cellular communication[2]. It is hoped that insight into the basic mechanism of particulate assembly in these multi-component systems can be derived from the study of simple model systems, such as colloidal particles.

Approaches to 2D or 3D self-assembly of colloidal particles have exploited electrostatic interactions[3-5], external electric fields[6,7], covalent bonding[8], and capillary forces[9-11]. Fabricating optical devices with colloidal particles can require control of particle size and position to create arrays of particles that periodic. Natan et al.[12] first employed the idea of chemically binding to assemble colloidal particles in 2-D, and this work was extended by Sato et al.[13], He et al.[8,14], and Zheng et al.[15]. Using different approaches, Yeh et al.[6], Trau et al.[7] employed an electric field to induce pattern formation in colloid dispersions, and Mio et al.[14] utilized optical trapping to make an array of colloidal particles.

In this study, we report efforts to develop an easier and more effective method to make colloidal particle patterns, and we discuss the mechanisms of 2-D self-assembly of latex particles in wetting films on patterned polymer surfaces. In the experimental section, the materials, experimental apparatus and procedures are introduced. In the experimental results and discussion section, detailed observations of the dynamics and discussions of the mechanisms in those processes are reported. The last section provides a conclusion.

2.2. Experimental Section

1. Materials: Polybead Carboxylate 914 nm microspheres (Polyscience Inc, 2.61% solids-latex) were used. The solutions were prepared by diluting the original suspension to the desired concentrations with deionized water. The patterned polymer cells were prepared by casting prepolymer (Sylgard 184 silicone elastomer) onto single crystal silicon masters (Ted Pella, Inc.) and leaving to cure for two days. After peeling off the polymer, one obtains a polymer cell with patterns at the bottom, providing a negative of the master, see Figure 2-1.

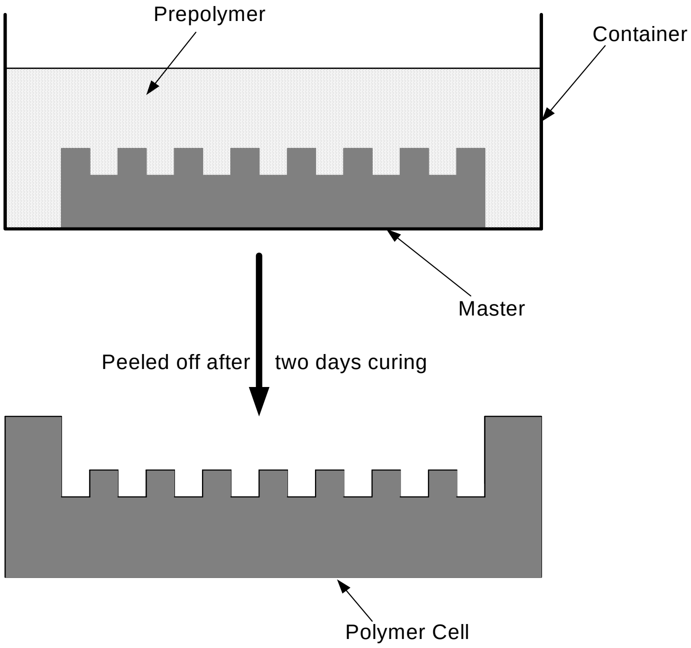

Figure 2-1. Preparation of the patterned polymer cells.

The size of the generated cell was typically 5*mm*x5*mm* and the depth was 0.5*mm*. The pattern that was examined had 2μm wide, 500*nm* deep grooves that crossed and encircled 8μm square mesas. On the master, a broader marking line was written every 500μm, which was useful for orienting the sample for light microscopy.

2. Apparatus: An integrated zoom microscope (10x objective, 2x TV camera tube, motorized zoom system, motorized focus, through-the-lens illumination) of a Dimension 3100 AFM (DI) system was employed to observe the self-assembly processes. A CCD camera and a camcorder were used in some cases to record data.

3. Procedures: Most of the experiments were done at room temperature and ~20% humidity. Before use, the polymer cells were oxidized with air plasma to make their surfaces hydrophilic. A VIC 500 (Electronics Corporation) at power level 8 (highest level 10 = 1800 watts) for 2 minutes was used to generate a hydrophilic layer on the cell surface. It was found that the cells

should be used soon after the oxidization because overnight the cells lose their hydrophilic layers. To observe the process of colloidal particle self-assembly in wetting films, about 12.5μL (equal to the volume of the cell) 0.1% latex suspension was added to the cell and left to dry. The 2D-motorized positioning station was used to move the cell, the Z-scanner was used to focus and the zooming optics of the microscope was used to zoom in where interested, tracking the whole process. The video function was used to save pictures of the processes.

2.3. Experimental Results

1. Observations of the dynamics of the self-assembly process

Using the apparatus described above, the dynamics of the self-assembly process were directly observed and recorded.

In the beginning, the cell was filled with the 0.1% latex suspension to create an approximately flat liquid surface. As the water in the suspension evaporated, the liquid surface became concave because of the capillary force at the cell wall. At this stage, microscopic observations showed that the latex particles made Brownian motion, see Figure 2-2.

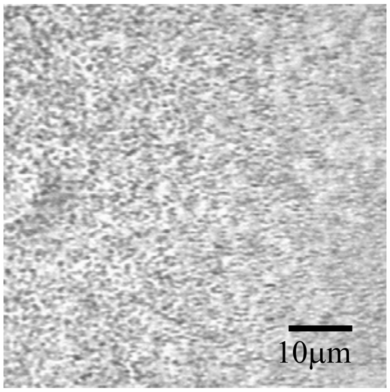

Figure 2-2. The colloidal particles in the suspension made Brownian motion during the process of water evaporation.

After the thickness of the concave center was reduced to a value comparable to the size of the latex particles (~1μm), we observed a very small region (about 50μm) at the center of the layer, containing particles that were more dense and ordered, see Figure 2-3.

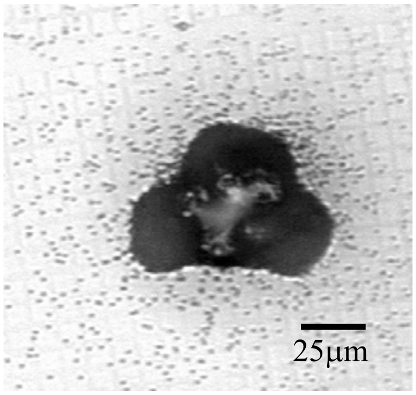

Figure 2-3. A dense colloidal particle array (about 50 μm in diameter) forms at the center of the cell when the thickness of the concave film center falls to a value comparable to the size of the latex particles (~1 μm).

As the film thinned, the wetting film at the center suddenly ruptured, leaving a dense particle array, and the periphery of the rupture region rapidly receded and formed a relatively dry region of about 400-600μm across. This characteristic region is hereafter denoted as Region A, see Figure 2-4.

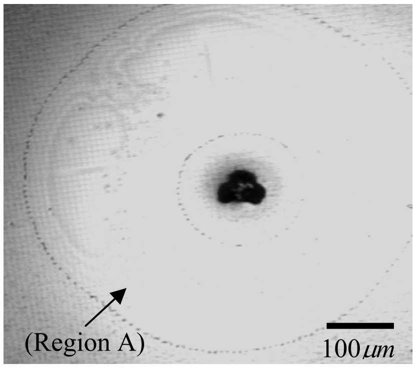

Figure 2-4. The arrow denotes Region A (about 400-600 μm) — the rupture region around the centered dense colloidal particle array in Figure 2-3.

The liquid film around the periphery of Region A thickened due to film rupture and evolved into another dynamic equilibrium state. At this point, the process of pattern-assisted latex particle self-assembly started along the periphery of Region A, see Figure 2-5a. The particles were transported toward to the leading edge of the pattern, and moved inside the crossing grooves in directions both parallel and perpendicular to the direction of the net flux. The particles in the grooves were attracted to each other to form longer chains and crystals. The patterned crystal grew radially toward the cell periphery. As more particles filled the grooves, a large beautiful pattern of colloid particle crystal formed, following the pattern of the substrate. At this point, there were no particles on the mesas. This characteristic region is hereafter denoted as Region B, see Figure 2-5b. Microscopic observations showed that the flow rate of the particles significantly increased at a certain moment, and the rapidly moving particles self-assembled both on the mesas and in the grooves. This characteristic region is hereafter denoted as Region C, see Figure 2-5c.

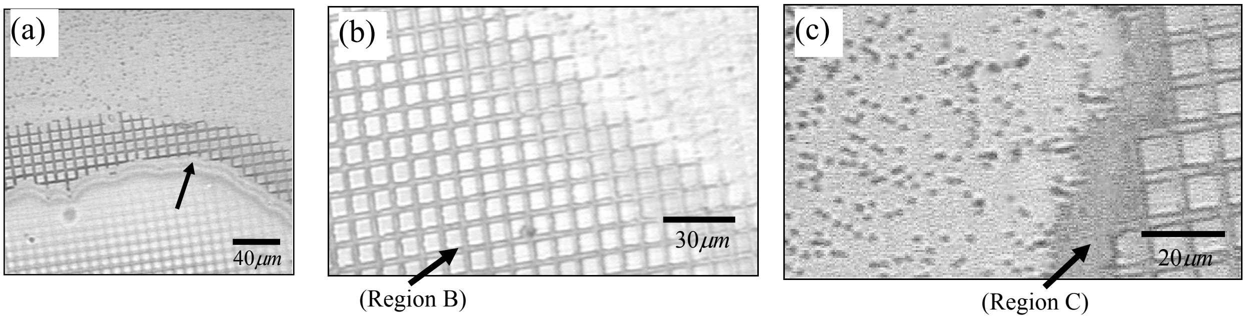

Figure 2-5. Several pictures of the late stage of the evaporation process (after the beginning of self-assembly in a pattern). The square in each graph is 8 μm x 8 μm. (a) Pattern-assisted latex particle self-assembly starts along the periphery of Region A, as denoted by the arrow; (b) A large beautiful pattern of colloid particle crystal forms, following the pattern of the substrate; (c) Particles self-assembling both on the mesas and in the grooves to form Region C.

The flow rate diminished during the formation of Region C, and self-assembly only in grooves started again to form Region B. In most cases, we observed that the radial formations of Region B and Region C occurred, see Figure 2-6.

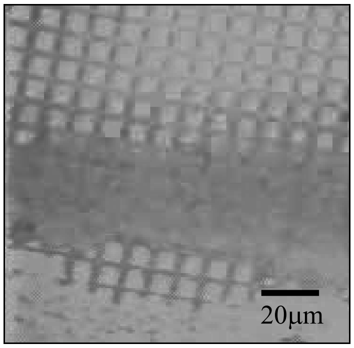

Figure 2-6. The radial formations of Region B and Region C occur alternately in a varying way; the boundaries do not have regular shapes.

In the whole process, because of the unevenness of the surface of the cell and some other factors such as polydispersity of colloid particles, air convection over the liquid film, surrounding conditions, motorized positioning station moving during observations, etc., the phenomena described above occurred with slight variations. For example, Region A is rarely circular (Figure 2-4), although that would be expected because of surface tension; Region C along the edge of the Region B does not necessarily exhibit a regular shape either, and the persistence of Region C formation is not uniform across all areas (Figure 2-6). Some open spots can form in Region B and C, seen by Newton rings, and are caused by the local film rupture. We also used AFM to analyze the 2D latex-particle patterned crystal formed by this process. The results are shown in Figure 1-1.

2.4. Discussion

(1) Mechanism of particle transportation.

The particles were brought to the growing pattern's edge by water flux. The question is: what makes this flux?

The system we are studying is an evaporating meniscus. Various authors[17-20] have suggested that the pressure gradient in the liquid film is sufficient to support a fluid flow. Optical interferometry was used by them to obtain the meniscus profile, and resistance thermometry was used to obtain the heat flux for the evaporating meniscus. It was found that the different evaporation rates along the liquid-vapor interface result in the changes in the meniscus profile, which in turn results in a pressure gradient. An extended meniscus can be divided into three zones[17] (see solid lines in Figure 2-7): (1) the immediate vicinity of the triple interline (junction of solid-liquid-vapor) - the thin film region, where the liquid flow results from the pressure gradient produced in the liquid by the varying force of attraction between the liquid and solid (disjoining pressure); (2) the inner intrinsic meniscus region where the fluid flow results from very large pressure gradients due to the curvature gradient; and (3) the outer intrinsic meniscus region where the fluid flow results from small pressure gradients due to curvature gradient. Experimental and theoretical studies showed that the evaporation rate has a maximum at the transition point between the thin film region and the inner intrinsic meniscus region, and decreases sharply to zero at the triple interline. The average flow rate u(x) accordingly has the similar behavior, which is shown in Figure 2-7. For details about the pressure-gradient driven flow, see the Appendix.

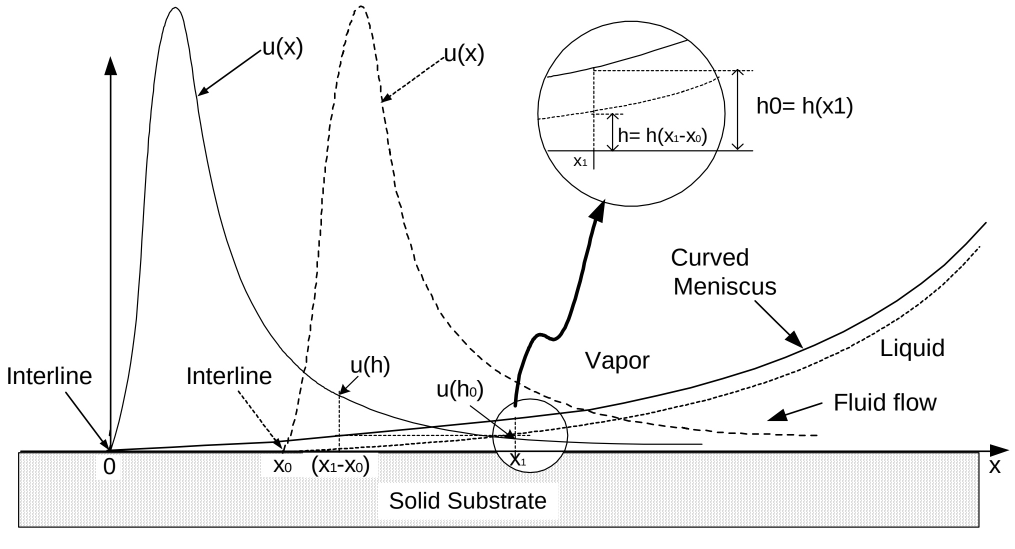

Figure 2-7. An evaporating meniscus and the average flow rate "u(x)"distribution (solid lines). In a minimal time period t, the meniscus interline recedes from 0 to x_0. The solid lines show the case where the meniscus interline is at 0, and the dashed lines show the case where the meniscus interline is at x_0.

Observations showed that whenever a Region B grows, there is always a transition region between the Region B and the region of the bulk fluid flux, see the cartoon in Figure 2-8. In Region B, particles were already assembled into long crystals, and there is virtually no liquid film. The transition region has a thin fluid film with a thickness comparable to the size of particles. Particles are transported within the parallel and perpendicular grooves of the substrate. The region of the bulk fluid flux is much thicker than the size of particles. Particles are transported by the fluid flux toward to the transition region. V_p is the proceeding rate of Region B, and V_M is the proceeding rate of the leading edge of Transition region (or the receding rate of the meniscus interline).

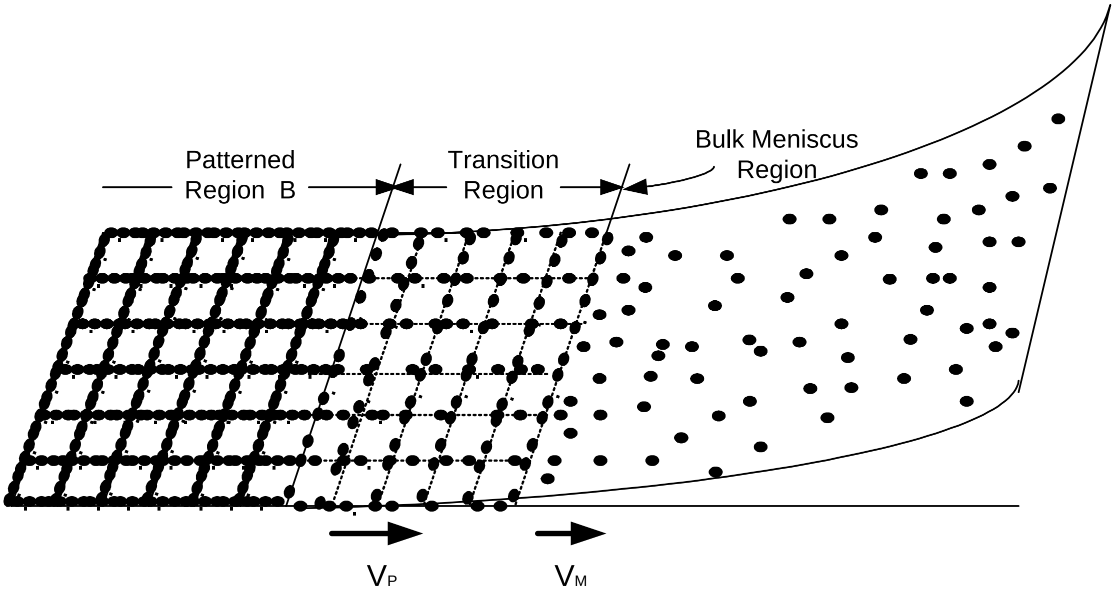

Figure 2-8. Whenever a Region B grows, there is always a transition region between the Region B and the bulk meniscus region. V_p is the proceeding rate of Region B, and V_M is the proceeding rate of the leading edge of Transition region.

The observations of the particles' speeds close to the leading edge of Transition Region can be used to test the model proposed in Figure 2-7. As seen in Figure 2-7, in a minimal time period *t*, the meniscus interline recedes (due to evaporation) from 0 to x_0 with a rate V_M during the Region B formation. In this process, the film thickness at x_1 changes from h_0 to h_1. We assume the contact angle is a constant, and the average speed of the liquid flux *u(x)* keeps the same profile along the meniscus. From the similarity of the two meniscuses, we have

$$\frac{h_1}{h_0}=\frac{h(x_1-x_0)}{h(x_1)}=\frac{x_1-x_0}{x_1}=\frac{x_1-V_M t}{x_1} \tag{2-1}$$

Hence

$$h(x_1-x_0)=h(x_1)\cdot(1-\frac{V_M}{x_1}t) \tag{2-2}$$

As shown in the appendix, the fluid flow rate is

$$u(x)=\frac{\int_0^{h(x)}u(y)dy}{\int_0^{h(x)}dy}=-\frac{\gamma_{lv}}{3\mu}h(x)'''h(x)^2 \tag{2-3}$$

Based on the model in [17],

$$h(x)'''=\frac{d^3h(x)}{dx^3}=-\frac{3\mu\dot{n}*}{\gamma_{lv}}\frac{1}{(h(x)+\delta*)^3} \tag{2-4}$$

In Equations (2-2) and (2-3), the γ_{lv} is the surface tension; and μ is the absolute viscosity, $\dot{n}^*$ is the total incoming volumetric flow rate per unit width, which is a constant; the parameter δ* is a measure of the region over which evaporation occurs and of the size of the initial pressure gradient in the model. Combining Equations (2-3) and (2-4), one obtains

$$u(x)=-\frac{\gamma_{lv}}{3\mu}h(x)'''h(x)^2=\dot{n}*.\frac{h(x)^2}{(h(x)+\delta*)^3} \tag{2-5}$$

The region that we are studying is part of the Bulk Meniscus Region, which is close to the Transition Region leading edge. In this region, the film thickness is slightly larger than the particle size (1μm), and the particles are dragged by the fluid flow. Within this range of film thickness, the fluid flow is laminar and viscous. The speed of the particle should be proportional to the flow rate. Therefore, one obtains

$$v(x) = A * u(x) \tag{2-6}$$

where *v(x)* is the speed of the particle, *A* is the proportional coefficient, *u(x)* is the flow rate. Thus, after introducing Equations (2-2) and (2-5) into Equation (2-6), one obtains

$$v(t)_{x_1} = v(h) = A \cdot \dot{n} * \cdot \frac{h(x_1 - x_0)^2}{(h(x_1 - x_0) + \delta *)^3} \tag{2-7}$$

For the simplicity of the discussion, in the region we are studying (relatively far from the interline) we assume a constant volumetric flow rate in this evaporating meniscus, which is according to the parameter δ*=0. Thus Equation (2-7) becomes

$$v(t)_{x_1} = v(h) = A \cdot \dot{n} * \cdot \frac{1}{h(x_1 - x_0)} \tag{2-8}$$

From Equations (2-2) and (2-8), one gets

$$\begin{aligned} v(t)_{x_1} &= v(h) = A \cdot \dot{n} * \cdot \frac{1}{h(x_1 - x_0)} = A \cdot \dot{n} * \cdot \frac{1}{h(x_1) \cdot (1 - \frac{V_M}{x_1} t)} \\ &= v(t = 0)_{x_1} \cdot \frac{1}{1 - \frac{V_M}{x_1} t} \end{aligned} \tag{2-9}$$

To test the above model, we collected data from video of the process, as follows:

We chose an area that is close to the leading edge of the Transition Region, and measured the average speeds of five different particles found within 100 μm of each other. We sampled over this area to reduce the influence of factors other than the fluid flow rate. The data collected are shown in Table 2-1.

Table 2-1. Particle speed data collected from video.

		Time for a particle moving 48um (s)						Average speed *v(t)* over 48 um (um/s)
		Position 1	Position 2	Position 3	Position 4	Position 5	Average	
time (s)	0	9.47	9.8	9.82	9.73	9.84	9.73	4.93
	2	8.94	9.13	9.05	9.34	8.92	9.08	5.29
	4	9.06	8.7	8.97	8.68	8.6	8.80	5.45
	6	8.38	8.56	8.79	9.27	8.75	8.75	5.48
	8	7.97	8.52	8.6	8.57	8.05	8.34	5.75
	10	7.96	8.21	8.32	8.07	7.89	8.09	5.93
	12	7.88	7.53	8.04	7.56	7.53	7.71	6.23
	14	7.74	7.38	7.26	6.91	7.06	7.27	6.60
	16	7.19	7.33	7.24	6.99	6.73	7.10	6.76
	18	6.68	6.55	7.17	6.41	6.39	6.64	7.23

We plotted the average speed versus time and fitted a reciprocal function as follows, see Figure 2-9:

$$v(t)_{x_1} = a\cdot\frac{1}{1-b\cdot t} = 5.00\cdot\frac{1}{1-0.017\cdot t} \tag{2-10}$$

The fitting yields $a = 5.00$ µm/s and $b = 0.017\text{s}^{-1}$. The value of a is close to the coefficient "$v(t = 0)_{x1} = 4.93$ µm/s" in Equation (2-9).

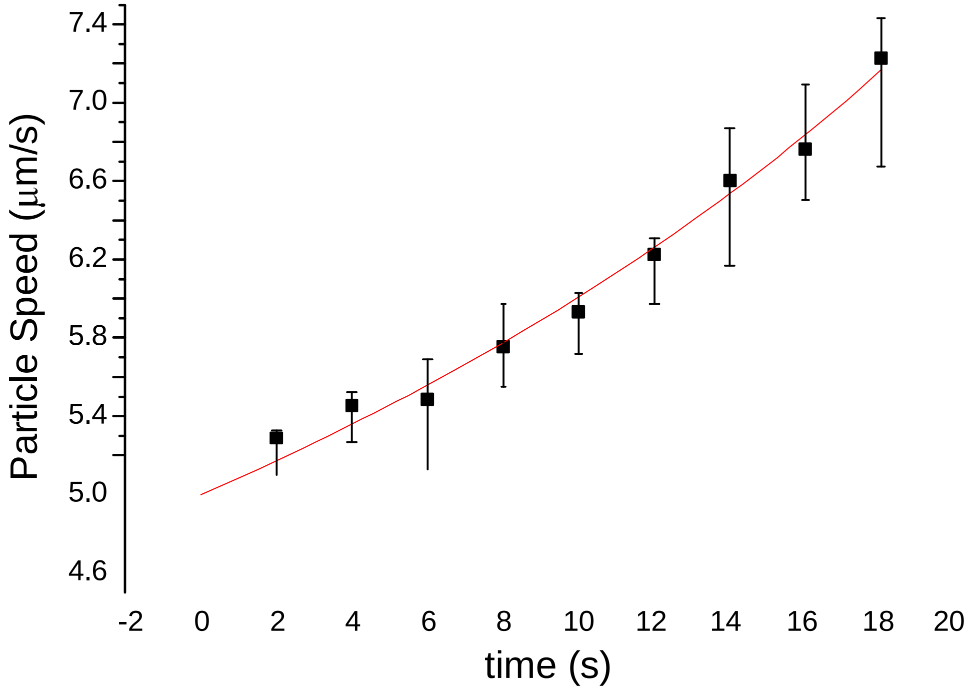

Figure 2-9. The average speed v(t) (um/s) changes with time(s) at a fixed point. The data was fitted with a reciprocal function of Equation (2-10).

We have estimated the value of the parameter V_M/x_1 as follows: The motion of Transition Region leading edge provides V_M. From the first two pictures in Figure 2-10, the Transition Region leading edge moved about $20\mu m$ in $25s$. Thus V_M can roughly be $20\mu m\ /25s$. We know $x_1 = 48\ um$, hence $V_M/x_1 = (20/25)/48 = 0.017\ s^{-1}$. This parameter is close to the corresponding parameter from the numerical fit, reported above. The quality of the fit to the data supports the use of this transportation model.

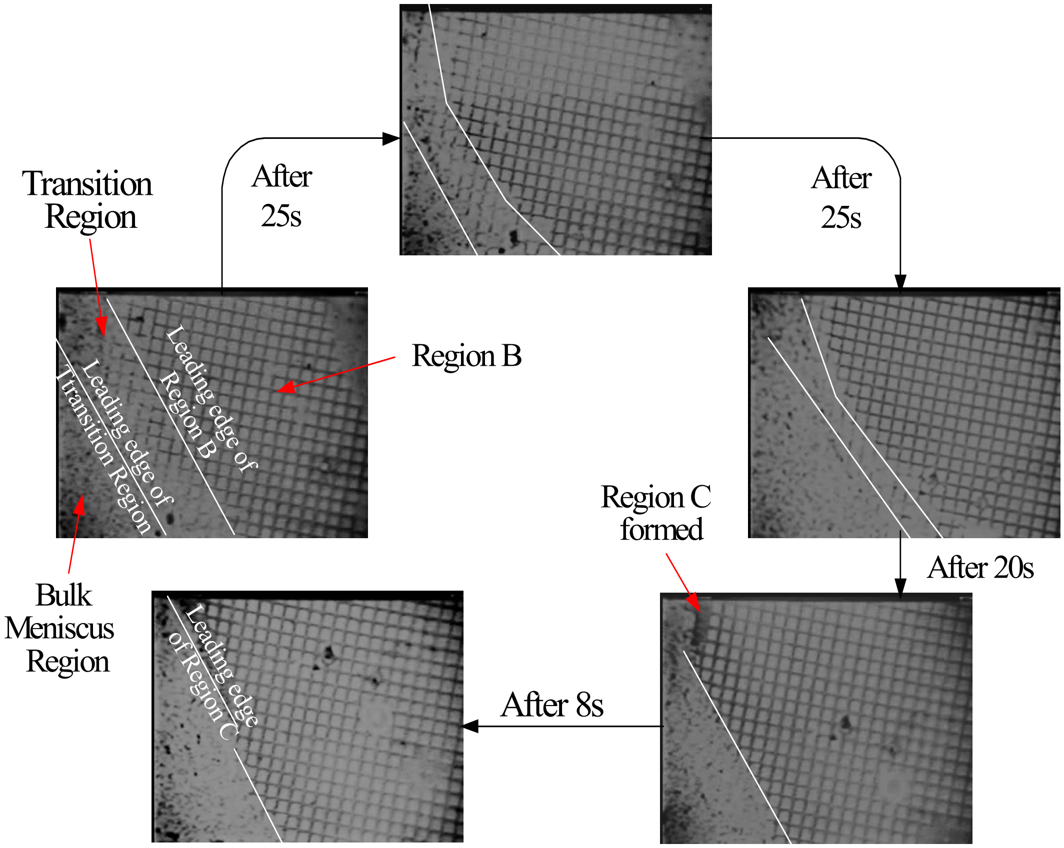

Figure 2-10. Pictures captured from the video show the changes of Transition region.

Why does Region C form, where one sees dense packing of particles on grooves AND mesas? We propose the following model, where the liquid film thickness determines particle mobility, see Figure 2-8 (top view) and Figure 2-11 (side view).

When Region B forms, the particles move only within either parallel or perpendicular grooves of the Transition Region; there is inadequate flow atop the mesas. On the other hand, in the Bulk Meniscus Region, flow atop the entire surface is strong enough that particles glide over the grooves and fail to fill them. As Region B grows, the Transition Region shortens, see Figure 2-10. Finally it disappears, and Region B directly contacts the Bulk Meniscus Region. Region C starts to form because the film thickness at the interline is now close to 1 μm. This dynamic process is illustrated by a cartoon in Figure 2-8 and Figure 2-11.

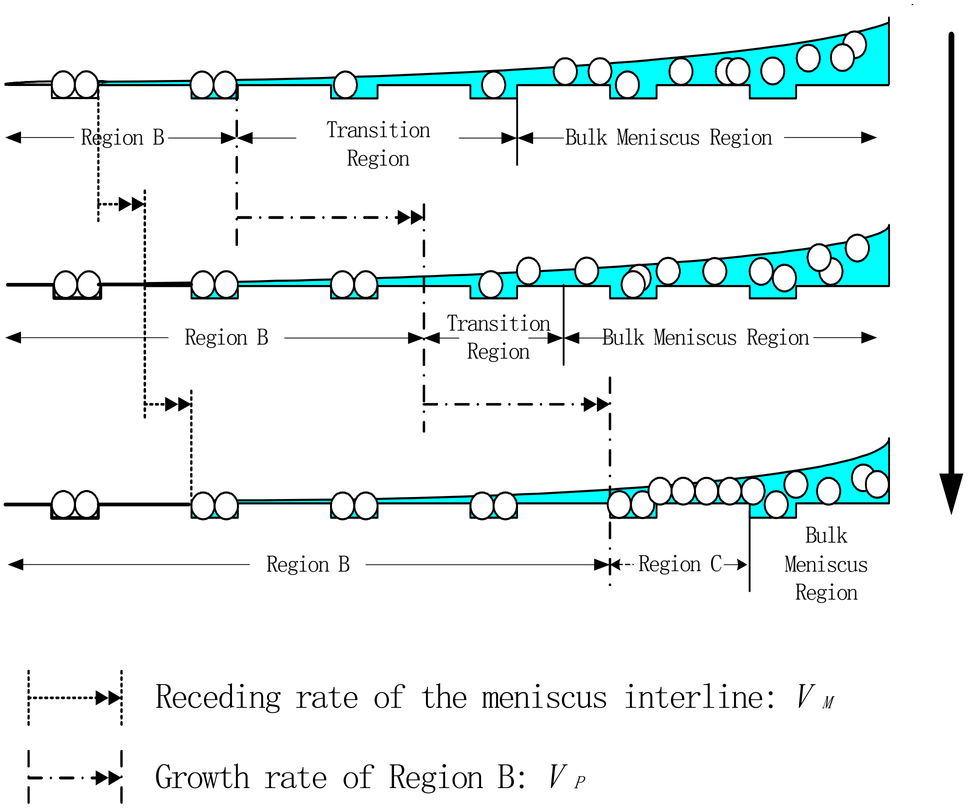

Figure 2-11. The competition between pattern growth rate VP and the meniscus receding rate VM causes Transition Region to shrink (side view).

Because the contact angle is a constant, we conclude that the rate of Region B's growth, V_P, is greater than the rate the meniscus interline to recede, V_M, due to evaporation. Region C grows more slowly than Region B because Region C requires many more particles per unit area. V_M exceeds V_P, causing the film thickness of the vicinity of the interline to be reduced until a transition region appears. At this point, Region B reforms, see Figure 2-6. Other factors, including large size particles, higher features of the substrate, coagulation of the particles and the contact line pinning effect[21,22], can lead to the formation of localized C-type regions, which depends on the film thickness close to the pattern's leading edge.

(2) Mechanism of the Self-Assembly

We return to the region of crystal formation. There is a wetting film in this region. In Region B, microscopic observations show that, in the transition region, the particles move inside the grooves in either parallel or perpendicular directions, and finally forward to the leading edge of Region B. As they move inside the grooves, the particles self-assembly. The incoming particles either incorporate into an existing crystal or form new short chains, which then attract each other to form longer chains. Previous work by Kralchevsky et al.[23-25] and Yamaki et al.[26], has shown that the lateral capillary force drives self-assembly in a similar situation. A lateral capillary force exists between the particles partially immersed in a liquid layer. The deformation of the liquid layer due to the wetting of the particle surface provides the lateral capillary force[11, 23-26], see Figure 2-12.

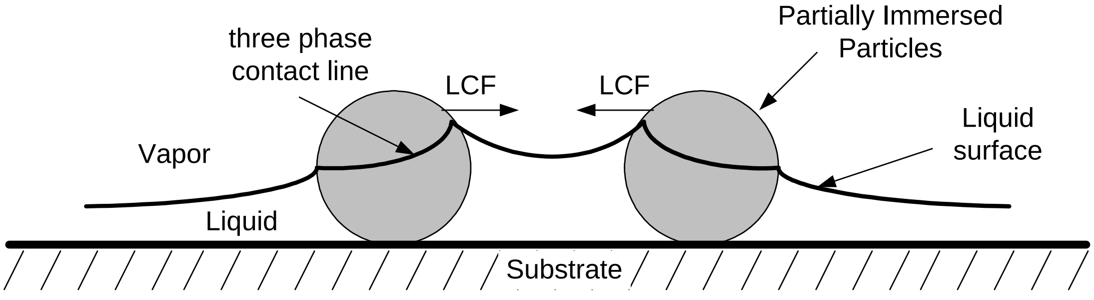

Figure 2-12. The physical nature of the lateral capillary force (LCF) between the partially immersed particles. The LCF is the total effect of the vapor pressure, liquid pressure and the surface tension along the three phase contact line on the particles.

Self-assembly in the grooves perpendicular to the flux direction strongly supports that the lateral capillary force is acting on the partially immersed particles. Apparently, the presence of the transition region just allows the action of the lateral capillary force.

2.5. Conclusion

In this study, the bottom-patterned polymer cells were made and used to study the process of the two-dimensional-self-assembly of latex particles in wetting films on patterned surfaces. Based on direct microscopic observations, the mechanisms of the particle transportation and the particle self-assembly were discussed. The particles were transported by a flux caused by the pressure gradient in an evaporating meniscus. The self-assembly of particles was driven by the lateral capillary force between the partially immersed particles. 2-D latex particle patterned crystals can be designed by exploiting the features of the substrate.

This paper has demonstrated a method to generate 2D latex particle patterns over a spatial range of up to 200 μm. An important future direction of this work is to extend uniform patterning over several millimeters. This is necessary for constructing photonic devices of practical dimensions. In addition, patterning of biological particles using this technique, in varying solvents and with particles of different modulus, should also prove possible. This may also provide insight into the design of textured polymer surfaces for applications such as non-toxic, fouling prevention in marine and implant environments.

2.6. Appendix

Fluid flow driven by the pressure gradient due to curvature in an evaporating meniscus

The local liquid film pressure is related to the ambient pressure by capillary equation:

$$P_v - P_l(x) = \gamma_{lv} \cdot K(x) \tag{2-11}$$

where $K(x)$ is the local curvature of the liquid-vapor interface and γ_{lv} is the surface tension. A change in curvature then provides a mechanism for producing the pressure gradient for flow in the evaporating meniscus. Assuming constant surface tension along the interface, Equation (2-11) can be differentiated as follows:

$$-\frac{dp_l}{dx} = \gamma_{lv}\frac{d}{dx}\left[\frac{h''}{(1+h'^2)^{3/2}}\right] = \gamma_{lv}\left[h''' - \frac{3}{2}h'h''^2 + \cdots\right] \tag{2-12}$$

It has been common practice to ignore all terms except for the first in the interline vicinity because of the small meniscus slope. Thus Equation (2-12) becomes

$$-\frac{dp_l}{dx} = \gamma_{lv}h''' \tag{2-13}$$

The Navier-Stokes momentum equation gives:

$$\frac{dp_l}{dx} = \mu\frac{d^2u}{dy^2} \tag{2-14}$$

where μ is the viscosity coefficient. Solving Equations (2-13) and (2-14) under the appropriate no-slip condition at y = 0 and no-shear condition at y = h, one obtains

$$u(y) = \frac{-\gamma_{lv}}{\mu}h'''(\frac{y^2}{2} - hy) \tag{2-15}$$

and

$$u(x) = \frac{\int_0^{h(x)} u(y)dy}{\int_0^{h(x)} dy} = -\frac{\gamma_{lv}}{3\mu} h''' h^2 \tag{2-16}$$

It is not possible to obtain the analytical solutions to the above equations. However, by experimentally and theoretically studying the evaporating meniscus, various authors[17-20] have found that the evaporation rate has its maximum close to the interline caused by the local temperature difference between the liquid-vapor interface and substrate surface.

BIBLIOGRAPHY

1. van Blaaderen A., Ruel R., and Wiltzius P., *Nature* **1997**, *385*, 321-323; van Blaaderen A. and Wiltzius P., *Adv. Mat.* **1997**, *9*, 833-837
2. Andersson, M., Berntsson, P., Jonsson, P., and Gatenholm, P., *Biofouling* **1999**, *14*, 167-178; Roberts C., Chen S.C., Mrksich M., Martichonok V., Ingber E. D., and Whitesides M. G., *J. Am. Chem. Soc.* **1998**, *120*, 6548-6555.
3. Chen, K.M.; Jiang, X.; Kimerling, L.C.; Hammond P.T. *Langmuir* **2000**, *16*, 7825-7834
4. Tien, J.; Terfort, A.; Whitesides, G.M. *Langmuir* **1997**, *13*, 5349-5355
5. Schmitt, J.; Machtle, P.; Eck, D.; Mohwald, H.; Helm, C.A. *Langmuir* **1999**, *15*, 3256-3260
6. Yeh, S.; Seul, M.; Shraiman, B.I. *Nature* **1997**, *386*, 57-59
7. Trau, M.; Saville, D.A.; Aksay, I.A. *Science* **1996**, *272*, 706-709
   Trau, M.; Sankaran, S.; Saville, D.A.; Aksay, I.A. *Nature* **1995**, *374*, 437-439
   Hayward, R.C.; Saville, D.A.; Aksay, I.A. *Nature* **2000**, *404*, 56-59
8. He, H.X.; Zhang, H.; Li, Q.G.; Zhu, T.; Li. S.F.Y.; Liu, Z.F. *Langmuir* **2000**, *16*, 3846-3851
9. Jiang, P.; Bertone, J.F.; Hwang, K.S.; Colvin, V.L. *Chem. Meter.* **1999**, *11*, 2132-2140

10. Dushkin, C.D.; Nagayama, K.; Miwa, T.; Kralchevsky, P.A. *Langmuir* **1993**, *9*, 3695-3701

11. Denkov, N.D.; Velev, O.D.; Kralchevsky, P.A.; Ivanov, I.B.; Yoshimura, H; Nagayama, K. *Nature* **1993**, *361*, 26

12. Freeman, R.G.; Grabar, K.C.; Allison, K.J.; Bright, R.M.; Divas, J.A.; Guthrie, A.P.; Hommer, M.B.; Jackson, M.A.; Smith, P.C.; Walter, D.G.; Natan, M.J. *Science* **1995**, *267*, 1629-1632

13. Sato, T.; Hasko, D.G.; Ahmed, H. *J. Vac. Sci. Technol. B* **1997**, *15*, 45-49

14. He, H.X.; Huang, W.; Zhang, H.; Li, Q.G.; Li, F.Y.S.; Liu, Z.F. *Langmuir* **2000**, *16*, 517

15. Zhang, J.; Zhu, Z.; Chen, H.; Liu, Z. *Langmuir* **2000**, *16*, 4409-4412

16. Mio, C.; Marr, D.W.M. *Adv. Mater.* **2000**, *12*, 917

17. Renk, F.J.; Wayner, P.C., Jr. *Journal of Heat Transfer* **1978**, *101*, 55-62

18. Moosman, S.; Homsy, G.M. *J. Colloid Interface Sci.* **1980**, *73*, 212-223

19. Renk, F.J.; Wayner, P.C., Jr. *J. Colloid Interface Sci.* **1978**, *67*, 408-414

20. Potash, M., Jr; Wayner, P.C., Jr; *Int. J. Heat Mass Transfer* **1972**, *15*, 1851-1863

21. Deegan, R.D.; Bakajin, O.; Dupont, T.F.; Huber, G.; Nagel, S.R.; Witten, T.A. *Nature* **1997**, *389*, 827-829

22. Deegan, R.D.; Bakajin, O.; Dupont, T.F.; Huber, G.; Nagel, S.R.; Witten, T.A. *Phys. Rev. E* **2000**, *62*, 756-765

23. Kralchevsky, P.A.; Nagayama, K. *Adv. Colloid Interface Sci.* **2000**, *85*, 145-192

24. Dushkin, C.D.; Nagayama, K.; Miwa, T.; Kralchevsky, P.A. *Langmuir* **1993**, *9*, 3695-3700

25. Kralchevsky, P.A.; Nagayama, K. *Langmuir* **1994**, *10*, 23-28

26. Yamaki, M.; Higo, J.; Nagayama, K. *Langmuir* **1994**, *10*, 432-436

Chapter 3. Using the Adhesive Interaction between AFM tips and Polymer Surfaces to Measure the Elastic Modulus of Compliant Samples

Abstract

An atomic force microscope (AFM) method for measuring surface elasticity based on the adhesive interactions between an AFM tip and sample surfaces is introduced. The method is particularly useful when there is a large adhesion between the tip and soft samples, when the indentation method would be less accurate. For thin and soft samples, this method will have much less interference from the substrate than is found using the indentation method because there is only passive indentation induced by tip-sample adhesion; in contrast, a large indentation with a sharp tip in the sample may break its stress-strain linearity, or even make it fracture. For the case where it is difficult to accurately locate the tip-sample contact point, which is problematic for the indentation method, the method based on adhesive interactions is helpful because it does not require locating the tip-sample contact point when fitting the whole retraction force curve. The model is tested on PDMS polymers with different degrees of cross-linking.

3.1. Introduction

The atomic force microscope (AFM) can be used to measure elasticity of surfaces[1-8]. Compared with other tools, AFM can probe local surface mechanical properties with high resolution, down to several tens of nanometers, and with fine control of applied force, down to several nano-newtons[9-11]. These two characteristics give the AFM advantages for studying the mechanical properties of polymeric and biological systems because most of these exhibit nano-scale heterogeneous modulus distribution.

Historically, the measurement of elasticity using AFM has been accomplished by the indentation method[12-16], in which the AFM tip is pushed into the surface of the sample, and force-versus-distance curves are monitored. The recorded force curves can be used to quantitate elastic properties. However, the indentation technique has limitations when applied to soft, thin, or adhesive samples such as many biological and polymeric surfaces. For instance, in the cases where it is difficult to accurately locate the tip-sample contact point, a small uncertainty will cause a significant error in calculating sample elasticity using the indentation method. Active indentation in soft and thin samples also will have interference from the substrate modulus, which complicates the study of sample properties. Moreover, a large indentation with a sharp tip in the sample may break its stress-strain linearity, or even make it fracture. Sample elasticity can also be evaluated by AFM phase imaging[17,18] and the force modulation technique[19-22]; unfortunately, those techniques also have significant limitations. AFM phase imaging can only provide qualitative information about the sample viscoelasticity. The force modulation technique can not be applied to soft samples since during scanning there is a significant lateral force applied to the sample. In the presence of significant adhesion, the force modulation method is no longer quantitative because the elasticity value is derived using the value of applied force, which is difficult to quantitate.

The adhesive interaction and elastic deformation are related[23-25]. To complement the indentation measurements, adhesive interactions between the AFM tips and the sample surfaces can be used to provide the elasticity, though until now an accurate model has been lacking[26,27]. We introduce an improved method based on the adhesive interactions which effectively reduces limitations existing in the indentation method. The method is particularly useful when there is a large adhesion between the tip and soft samples. For thin and soft samples, this method will have much less interference from the substrate than is found using the indentation method because there is only passive indentation induced by tip-sample adhesion. Meanwhile, the lower stress induced by tip-sample adhesion may keep the stress-strain linearity of the sample. The method based on adhesive interactions does not require locating the tip-sample contact point when fitting the whole retraction force curve. In the theory section of this paper, a model based on using AFM force plots is proposed. In the section of materials and methods, details about samples and the experimental setup are provided. In the experimental section, we show results from applying the model to obtain the surface elasticity of a series of poly(dimethylsiloxane) PDMS polymers, with different degrees of cross-linking. In the discussion section, we discuss the advantages and limitations of our method.

3.2. Theory

Hertz[28] proposed a continuum mechanics model to describe the contact between two elastic spheres under external load in the absence of adhesion. However, the adhesion force can be significant and cannot be neglected when the external load is very small; studies have shown that significant elastic deformation can be induced by adhesion under zero external load in some systems[29,30]. As two elastic spheres contact, the adhesion and the external load causes an elastic deformation, and a contact area forms between the two elastic bodies.

When an AFM tip approaches and retracts from the sample, it is deflected by the interaction with the sample. A force curve is such a plot of the force applied to the AFM tip (or the sample) as a function of the tip-sample displacement of the cantilever holder relative to the surface. AFM force plots can provide detailed information about the interaction between an AFM tip and a sample. The Young’s modulus of a sample can be obtained from force plots by analyzing the sample deformation under adhesive interaction with an AFM tip. When an AFM tip approaches a soft sample, the adhesive interaction can draw the tip into the sample, and when an AFM tip retracts from a soft sample, the AFM tip can pull and deform the sample by the adhesive interaction. We treat the AFM tip and the sample as two elastic bodies, see Figure 3-1. The AFM tip is represented as a sphere, and the spring represents the AFM cantilever. *P* is the external force, *R* is radius of the tip end (because the sample's radius is much larger than the tip's, the normalized radius is equivalent to the tip radius), *a* is the radius of tip-sample contact region, k_c is the cantilever's force constant, and δ is the deformation of the sample surface (the tip deformation should be negligible because for Si_3N_4 tips, the Young's modulus is ~220 GPa and for commercial silicon cantilevers the Young's modulus is ~190 GPa[31], while the Young's modulus of the sample of interest in this work is only about 1 MPa).

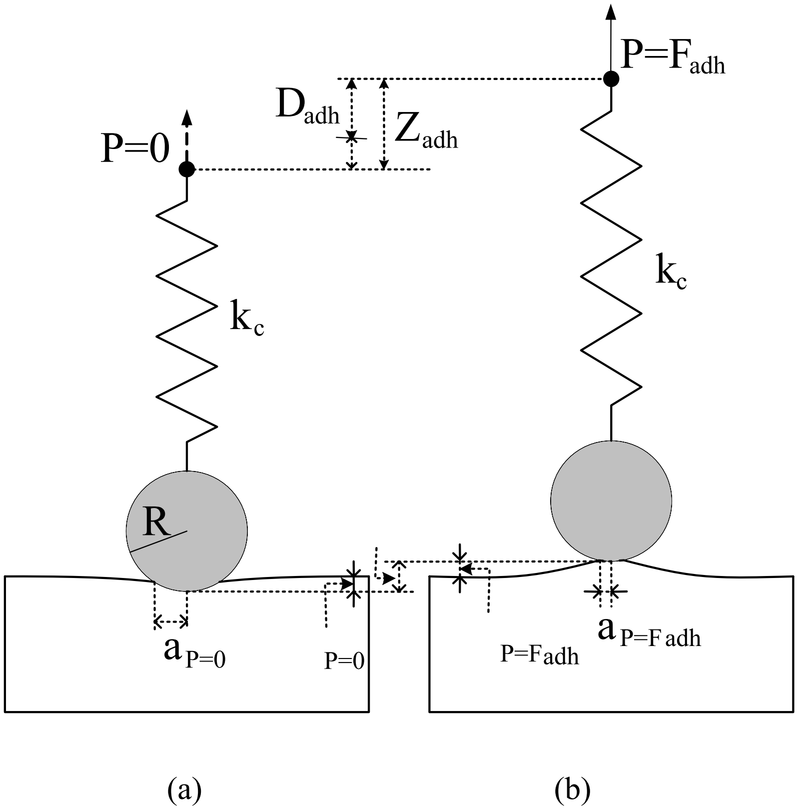

Figure 3-1. The AFM tip and sample treated as two elastic bodies. The AFM tip is represented as a sphere, and the spring represents the AFM cantilever. (a) The sample is deformed by adhesion when the external load P=0. (b) The sample is deformed by adhesion when the external load *P=0*. (b) The sample is deformed by adhesion when the external load *P=F_{adh}*.

Figure 3-1a is the case where the external load $P=0$, and Figure 3-1b is the case where the external load $P=F_{adh}$ where the contact between the tip and the sample ruptures. The deformation of the sample Δ is obtained by taking the distance between the points where the external load $P=0$ and where the external load $P=F_{adh}$. This Δ defines how much the sample can deform when it is pulled under the adhesive interaction between the tip and the sample. Z_{adh} is the retraction distance of AFM's piezoelectric actuator, and D_{adh} is the deflective displacement of AFM cantilever during this procedure. The total retraction distance Z_{adh} of AFM piezoelectric actuator consists of the deflection displacement D_{adh} of AFM cantilever and the deformation Δ of the sample.

A typical AFM force plot for such case is given in Figure 3-2, where the force is obtained by multiplying the AFM cantilever deflection by the force constant of the cantilever.

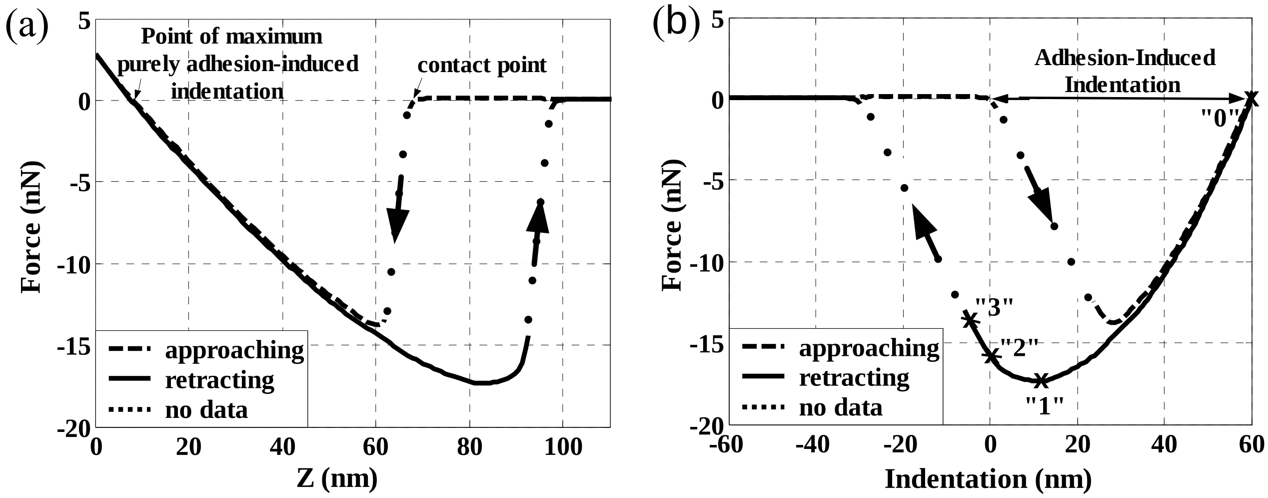

Figure 3-2. (a) A typical AFM force plot for the case of an AFM tip interacting with a soft sample under adhesive interaction. (b) The corresponding force vs. indentation plot. The forces on the AFM tip as it approaches the surface are indicated by the dashed lines while the forces upon retraction are shown by the solid lines. Point "0" is where the AFM tip has zero external force, "1" is where the tip has a maximum external force, "2" is where the tip has zero indentation in the sample, and "3" is where the tip ruptures from the sample.

Upon approach to the surface, the tip jumps to the surface at the point of mechanical instability, when the gradient of the interaction force exceeds the force constant of cantilever. Since the force curve showed in Fig. 3-2a does not exhibit an instantaneous jump-to contact, we can then conclude that the gradient of the interaction force is much less than the force constant of cantilever. Therefore, the point where the interaction becomes attractive corresponds to the point where tip contacts the surface. Once the tip contacts the surface, the tip is pulled into the sample by the adhesive interaction between the tip and the sample. This is shown as the sharp decrease of the force on the AFM cantilever in the extension part of the force plot in Figure 3-2a. The force plot is converted into its corresponding indentation vs. force plot in Figure 3-2b.

So long as the relationships of the indentation δ - contact radius a and of the external force P- contact radius a are known, one can obtain the elastic properties of the samples by combining any two points in the retraction part of the force plots, and we call the method based on using two such points on a force curve the "2-points method". For instance, the indentation δ and external force P are both functions of the contact radius a, interfacial energy γ_{12}, and the sample elasticity E; i.e. $\delta=\delta(a,\gamma_{12},E)$, and $P=P(a,\gamma_{12},E)$. For any two points on a force curve, there are four equations and four variables a_1, a_2, γ_{12}, and E, where a_1 and a_2 are the contact radii at the two points on a force curve. The indentation δ and external force P at each point can be obtained directly from the force curve in Figure 3-2b. Therefore, the sample elasticity E can be obtained by the 2-points method, see Appendix for details. For the ease of data processing and to compare consistently, we choose to combine the special points in the force curve to calculate the sample elasticity. More specifically, point "**0**" was combined with any of the three points "**1**", "**2**", and "**3**" according to the 2-points method. The combinations "**0**" with "**2**", and "**0**" with "**3**" can be used in simple analytical expressions for the sample elasticity in the JKR model[32], as will be discussed below. The sample elasticity can also be extracted by fitting the whole retraction curve of the force plots, as will be discussed in the discussion section. We will propose different methods to calculate the sample elasticity by treating an AFM tip in different ways. We will use subscripts to denote the related contact radius a, indentation δ, and external force P at each special point. For instance, a_1, δ_1, and P_1 are the contact radius, indentation, and external force at point "**1**" respectively.

Case 1. The AFM tip is treated as a sphere, and its contact radius with the sample is small.

For this case, Johnson, Kendall, and Roberts[32] proposed a theory (henceforth called JKR theory) that includes the adhesion effect. To assist the later introduction of our model, we first briefly review some of the main conclusions of JKR theory. Further details can be found in the literature[32].

As two elastic spheres contact, the adhesion and the external load causes an elastic deformation, and a contact area forms between the two elastic bodies. According to JKR theory, the contact radius a of the contact area is given by

$$a^3 = \frac{R}{K}\left[P + 3\pi R\gamma_{12} + \sqrt{6\pi RP\gamma_{12} + (3\pi R\gamma_{12})^2}\right] \tag{3-1}$$

$$a_0^3 = 6\gamma_{12}\pi R^2 / K \tag{3-2}$$

$$\delta = \frac{a^2}{R}\left[1 - \frac{2}{3}\left(\frac{a_0}{a}\right)^{3/2}\right] \tag{3-3}$$

where P is the external load, γ_{12} is the interfacial energy, a_0 is the contact radius under zero external load, δ is the sample deformation, $R=R_1R_2/(R_1+R_2)$ is the normalized radius of the two spheres with radii of R_1 and R_2, $K=4/3\pi(k_1+k_2)$. k_1 and k_2 are the elastic constants of each sphere, that is

$$k_1 = \frac{1-\nu_1^2}{\pi E_1} \quad \text{and} \quad k_2 = \frac{1-\nu_2^2}{\pi E_2}$$

where ν is the Poisson ratio, and E is the Young modulus of each material.

Under negative loads, the spherical tip adheres until, at the critical negative force, the surfaces suddenly jump apart. The contact radius a_3 at the rupture point is given by

$$a_3 = a_0 / 4^{1/3} = 0.63 a_0 \tag{3-4}$$

The point "**3**" in Figure 2b for the JKR model then can be located using Equation (3-4). Combining points "**0**" and "**3**", one obtains (details can be found in Appendix):

$$\delta_0 = \frac{1}{3}\sqrt[3]{\frac{16 \cdot P_3^2}{K^2 R}} \tag{3-5}$$

$$\delta_3 = -\frac{1}{3}\sqrt[3]{\frac{P_3^2}{K^2 R}} \tag{3-6}$$

Combining Equations (3-5) and (3-6), one obtains:

$$K = \left(\frac{1+16^{1/3}}{3}\right)^{3/2} \cdot \frac{P_3}{\sqrt{R \cdot (\delta_0 - \delta_3)^3}} \tag{3-7}$$

When, as is typical for examining polymer surfaces with a hard tip, the elastic modulus of the tip greatly exceeds that of the sample, the elastic modulus E of the sample is given by

$$E = \frac{3(1-v^2)K}{4} = \frac{3(1-v^2)}{4} \cdot \left(\frac{1+16^{1/3}}{3}\right)^{3/2} \cdot \frac{P_3}{\sqrt{R \cdot (\delta_0 - \delta_3)^3}} \tag{3-8}$$

where υ is the Poisson ratio of the sample.

Combining points "**0**" and "**2**": Similarly, one can obtain

$$E = \frac{3(1-v^2)P_2}{8}\sqrt{\frac{3}{\delta_0^3 R}} \tag{3-9}$$

Combining points "**0**" and "**1**": E can be obtained by solving Equations (3-1), (3-2) and (3-3). First, a_0 and a_1 can be solved from Equation (3-3) because δ_0 and δ_1 are known from the force plots; second, one combines Equations (3-1) and (3-2) and obtains

$$a_1^3 = \frac{R}{K}\left[P_1 + a_0^3 K/2R + \sqrt{P_1 a_0^3 K/R + (a_0^3 K/2R)^2}\right] \tag{3-10}$$

from which K can be obtained.

Case 2. The AFM tip is treated as a sphere, but its contact radius with the sample is large.

The JKR theory of the elastic contact of spheres with adhesion is valid only for small contact radii (much smaller than the sphere radii). Many references have theoretically and experimentally shown that for the case of small particles (about several μm) on very compliant elastic substrates (about several MPa), the contact radius under zero load can be rather large and does not vary as the particle radius to the 2/3 power, but rather to the first power[29,30,33,35]. This is true for the case in this study, where the tip end is small (<60 nm) and the samples are very compliant (<5 MPa). Maugis[36] extended the JKR theory by using the exact expression for the profile of the sphere and obtained $\delta(a)$, and $P(a)$.

$$\delta = \frac{a}{2}\ln\frac{R+a}{R-a} - \sqrt{\frac{8\pi a\gamma_{12}}{3K}} \tag{3-11}$$

$$P = \frac{3aK}{2}\left(\frac{R^2+a^2}{4a}\ln\frac{R+a}{R-a} - \frac{R}{2} - \sqrt{\frac{8\pi a\gamma_{12}}{3K}}\right) \tag{3-12}$$

Therefore, the sample elasticity can be obtained from Equations (3-11) and (3-12) by combining point "**0**" and any other special point in Figure 3-2b.

Case 3. The AFM tip is treated by a hyperboloid shape.

We used silicon nitride cantilevers (NP-C, Vecco Metrology, nominal k_c=0.58 N/m) to collect force plots, where the Si_3N_4 tip shape could be modeled by a hyperboloid. A SEM image of one of these tips, and a fit using hyperboloid shape can be seen in Figure 3-3.

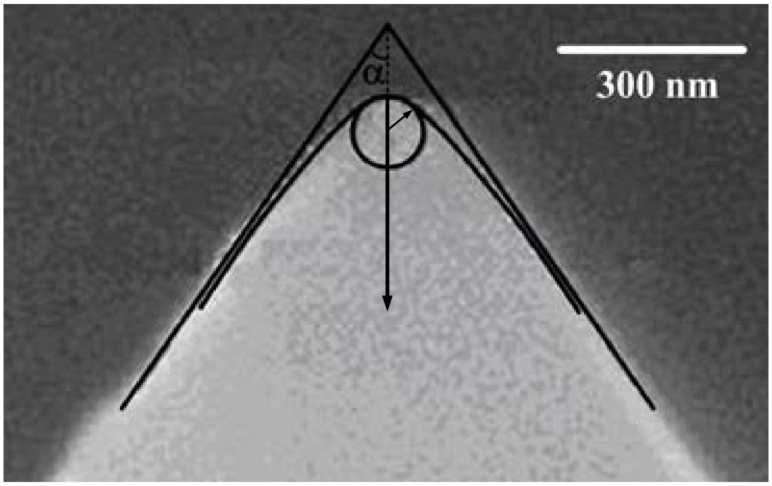

Figure 3-3. The Si3N4 tips used here can be modeled by hyperboloids. A SEM image of one of these tips is fitted by a hyperboloid profile. R is the radius of the curvature of the tip apex, α is the tip semivertical angle.

The profile function for a hyperboloid shape tip is given by

$$f(x) = R\cot^2\alpha\left[\sqrt{(ax/R\cot\alpha)^2+1}-1\right] \tag{3-13}$$

where R is the radius of the curvature of the tip apex, α is the tip semivertical angle as shown in Figure 3-3, and $x = r/a_0$ (a_0 is the contact radius, $0 \le r \le a_0$).

To solve the dependence of the load and indentation on the contact radius, we used Griffith's criterion[37] and the method proposed by Sneddon[38], and obtained

$$\delta = \frac{aA}{2R}\left[\frac{\pi}{2}+\arcsin\left(\frac{(a/A)^2-1}{(a/A)^2+1}\right)\right]-\sqrt{\frac{2a\pi(1-v^2)\gamma_{12}}{E}} \tag{3-14}$$

and

$$P=\frac{2E}{1-v^2}\left[\frac{A}{2R}\left[aA+\frac{a^2-A^2}{2}\left(\frac{\pi}{2}+\arcsin\frac{(a/A)^2-1}{(a/A)^2+1}\right)\right]-a\sqrt{\frac{2a\pi(1-v^2)\gamma_{12}}{E}}\right] \qquad (3\text{-}15)$$

where δ and P are the indentation and the load respectively. R is the tip radius of curvature, $A=R\cdot cot(\alpha)$, α is the tip semivertical angle, v is the Poisson ratio of the sample, E is the elastic modulus of the sample, a is the contact radius, and γ_{12} is the interfacial energy of the tip and the sample, see Appendix for details. The sample elasticity can be obtained based on Equations (3-14) and (3-15) by combining point "**0**" and any other special point in Figure 3-2b.

3.3. Materials and Methods

The methods introduced above relate the Young's modulus of a sample to its deformation under adhesive interaction with an AFM tip. For all the cases discussed above, the indentation and the AFM cantilever deflection can be obtained directly from the force plots, by which the contact radii can be calculated as discussed in the theory section above. For an example showing detailed computation of the 2-points method, see Appendix. The loading force on the AFM cantilever can be obtained by multiplying the cantilever deflection by k_c, the force constant of the AFM cantilever. k_c can be obtained by several methods[39-44]. We used Cleveland's method[42] to calibrate the force constants of cantilevers. The tip radii were measured by SEM and AFM[45]. To test our model, we studied a series of PDMS samples with different degrees of polymerization. PDMS has moderate adhesion to Si_3N_4 or silicon AFM tips.

PDMS samples were kindly provided by Vorvolakos and Chaudhury. Samples were prepared in hemisphere droplets with diameters of about 5 mm and heights of about 2 mm. The degree of polymerization was adjusted by controlling the ratio of the pre-polymer and cross-link agent[46]. The degree of polymerization (DP) of the samples are DP= 18, 25, 37, 60, 120, 253, and 705 (corresponding to molecular weights of the oligomeric precursor (kg/mol), M=1.33, 1.85, 2.74, 4.44, 8.88, 18.72, and 52.17, respectively). A smaller DP polymer is expected to have a larger elastic modulus because smaller DP corresponds to a higher density of cross-links, or smaller molecular weight between cross-links. Cross-links occur at the ends of oligomer precursors.

A Dimension 3100 AFM with a Nanoscope III controller (Vecco Metrology, Santa Barbara, CA) was used to collect the force curves. The polymer samples were imaged using AFM in intermittent contact mode and showed that the RMS roughness of the samples is ~1 nm over 5x5 μm^2 and 10x10 μm^2 scan size. (The details of surface roughness characterization can be found in Appendix.) A smooth sample surface can simplify the collection of force curves because the topographical effect is minimized. Force volumes[47]. arrays of force curves in a 2-D grid across the surface, were collected, to reduce the statistical error. Silicon cantilevers (NSC15, Micromash, nominal $k_c = 40$ N/m) were used for intermittent contact mode imaging. Before use, all tips were cleaned by argon plasma for 20 sec at a low power (180 W). A spherical colloidal tip was prepared by gluing a glass bead (about 7 μm in diameter) to the end of an NP-C cantilever using epoxy[48-50]. Cantilever sensitivities were collected on a piece of sapphire before and after each experiment.

The experiments were done on the PDMS samples with different degrees of polymerization using one silicon nitride cantilever and one bead-attached tip, so the cantilever force constants and the tip radii were the same for all samples. The force plots were processed by custom software written using Matlab (The Mathworks, Inc. Novi, MI).

3.4. Experimental Results

The analysis of force plots over a test area gives the distribution of sample moduli. A typical summary for 25 DP PDMS at scan rate of 0.1 Hz over 5x5 μm^2, analyzed using Equation (3-8) of the JKR model introduced above, is given in Figure 3-4.

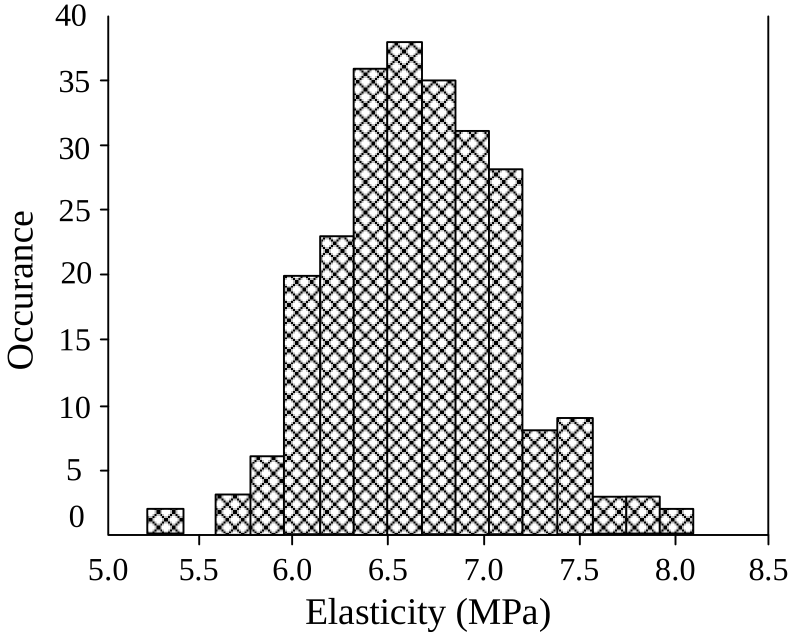

Figure 3-4. Elasticity (6.63 ± 0.47 MPa) obtained from force plots collected over a surface of 25 DP PDMS at a scan rate of 0.1Hz (Kc = 0.66 N/m, R = 58 nm) over an area of 5x5 μm2. There are 256 force plots in the force volume data. The data were analyzed using Equation (3-8) of the JKR model.

Figure 3-5 gives the elasticity values calculated by different methods for PDMS samples studied at a scan rate of 0.1 Hz, showing how elasticity correlates with the reciprocal of molecular weight of the oligomeric precursor. Also included are the macroscopic results of elasticity obtained using the well-known macroscopic JKR technique[46], in which hemispheres of the silicone rubber were pressed into contact with a reflective surface, and the normal load and contact area were recorded for a range of loads. Figure 3-5a and 3-5b were obtained using the same data collected by a regular silicon nitride NP-C AFM tip. Figure 3-5a gives the results obtained from JKR model which assumes a spherical tip; Figure 3-5b gives the results obtained from the model based on a hyperboloid tip, which is close to a real tip shape. Figure 3-5c was obtained using the data collected by a colloidal tip as described in the materials and methods section. When using the colloidal tip to collect force plots, the adhesion between the large tip and soft samples (120 DP, 253 DP and 705 DP) were so large that the cantilever deflection was beyond the detection limit. Thus the results for harder samples alone are given in Figure 3-5c.

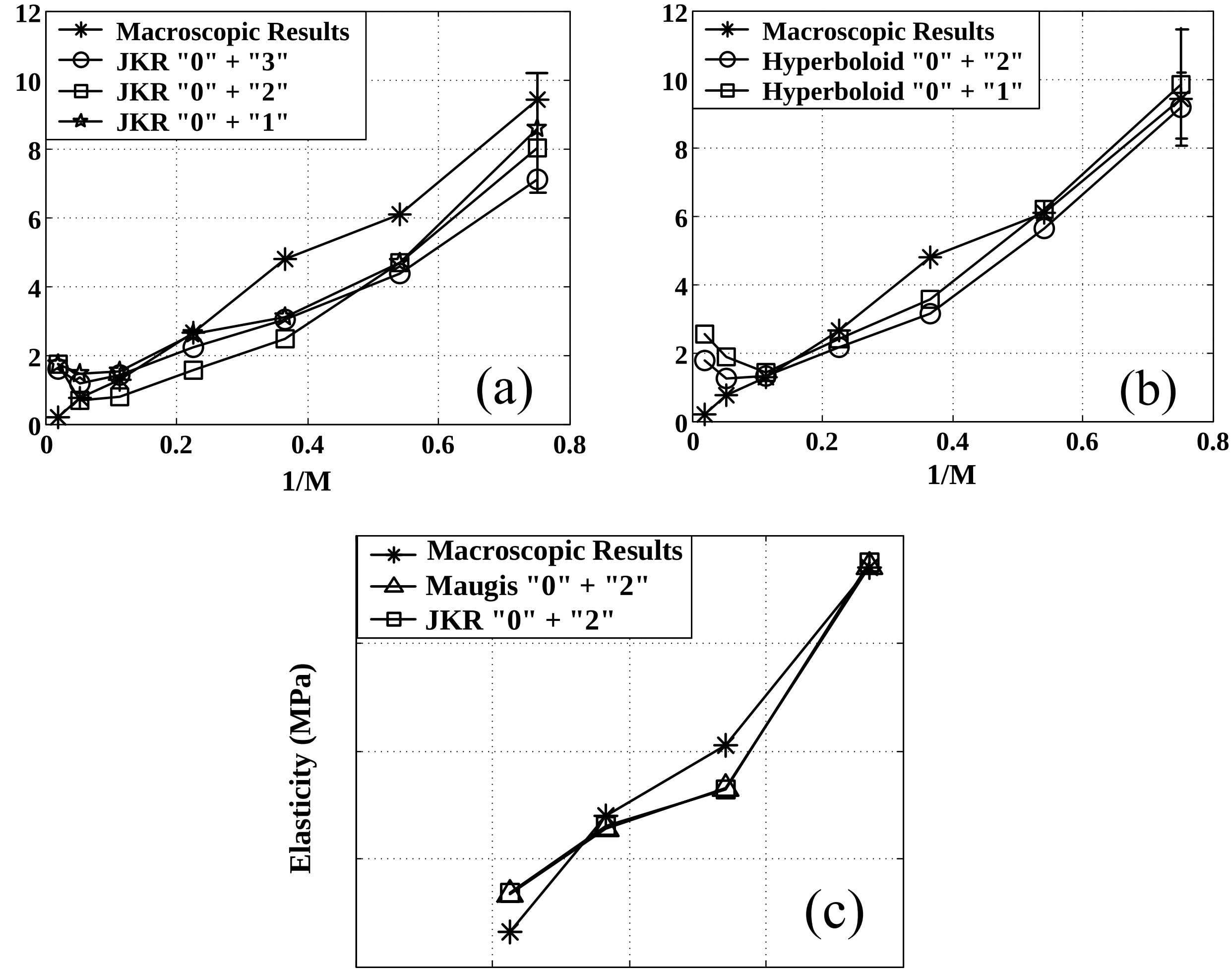

Figure 3-5. Elasticity for all PDMS samples obtained using different methods are plotted versus the reciprocal of molecular weight of the oligomeric precursor. (a) Results obtained from a JKR model which assumes a spherical tip; (b) Results obtained from a model based on a hyperboloid tip. (a) and (b) were obtained using the same data collected by a regular Si_3N_4 AFM tip. Obtained through analysis such as in Figure 4, each plotted elasticity in (a) and (b) represents the median value obtained from the corresponding force volume data at a scan rate of 0.1 Hz over an area of 5x5 μm^2. The error bars are the standard deviation of the mean of all the data in a force volume. For the data points that do not show error bars, actual errors are less than the marker size. (c) Results based on the data collected by a colloidal tip, whose adhesion to 120 DP, 253 DP, and 705 DP PDMS are so large that the cantilever deflection is over the AFM detection limit, so no elasticity values are obtained for these samples. The macroscopic results are taken from Vorvolakos[46].

3.5. Discussion

Comparing Figures 3-5a and 3-5b, one can see that the results obtained from the methods based on a hyperboloid tip shape are more consistent with the macroscopic results than those from the JKR methods. As we briefly mentioned above, the JKR theory for the elastic contact of those adhesive spheres is valid only for contact radii much smaller than sphere radii. This is not true for small particles on very compliant elastic substrates, which can have larger contact radii under a zero load. The real tip shape has to be considered when characterizing very soft samples because the adhesion-induced indentation of the AFM tip into a sample during loading is very large. For instance, when the external force is zero, the adhesion-induced indentation of a tip into 120 DP PDMS sample is about 200nm, which is much larger than the 60nm tip radius, see Figure 6. Treating the tip as a sphere with a radius of the tip apex significantly underestimates the real contact radius when a tip has a deep indentation into a sample. This is why the moduli obtained from the JKR methods are smaller than the macroscopic moduli for harder polymers (18 DP, 25 DP, 37 DP, and 60 DP). When a sharp tip indents into a network, whether or not the continuum mechanics can hold is always a concern. The sample we discussed in Figure 3-6 is the 120 DP PDMS. The PDMS samples studied in this work have highly coiled chains between networks and can hold their continuum mechanical property under large deformation. (See Appendix for a detailed discussion.) In addition, in Figure 3-6b, the strain of the polymer network under the tip can be estimated as 1 under the adhesion-induced stress, which is smaller than the upper limit for stress-strain linearity of typical rubbers. This analysis also implies another advantage of the method that is one can obtain the elasticity of the sample more accurately than using the indentation method if the indentation in the sample breaks stress-strain linearity of the sample, or makes it fracture.

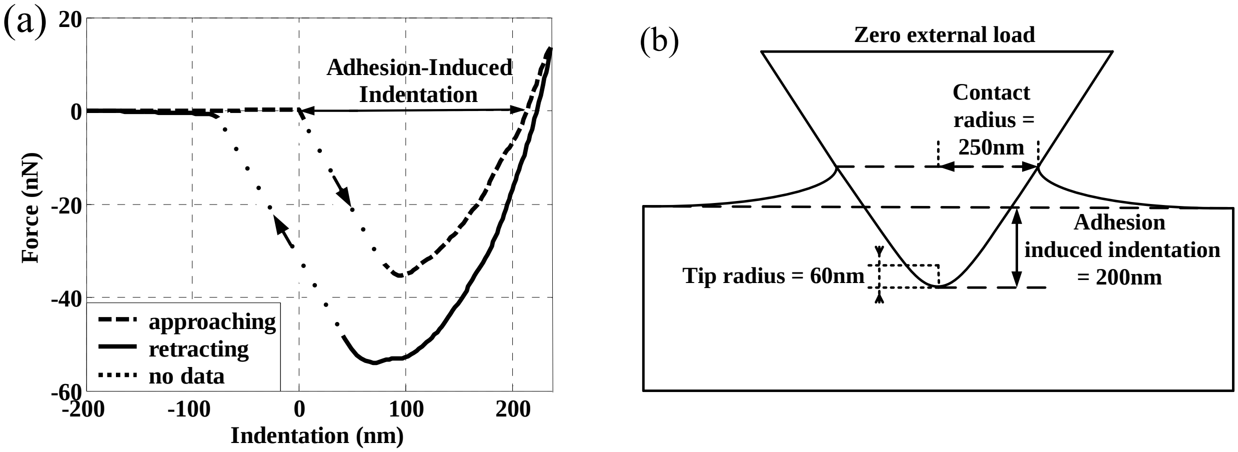

Figure 3-6. The adhesion-induced indentation of AFM tips on a very compliant surface can be much larger than the tip radius. (a) A typical force-indentation plot collected on a 120 DP PDMS sample using a regular Si3N4 AFM tip (kc = 0.66 N/m). (b) Schematic representation of a tip indenting the 120 DP PDMS sample due to the adhesive interaction.

One can see in Figure 3-5a and 3-5b that, for estimates made by both the JKR methods and the methods based on a hyperboloid tip shape, the moduli of softer polymer 253 DP and 705 DP are all much larger than those obtained using the macroscopic method. We believe that this is mainly due to the strong tacky effect for very soft materials, which was studied by Barquins and Maugis[51] for a spherical tip. This will be discussed in Chapter 4.

To examine this assumption, we calculated elasticity values solely based on the adhesion-induced indentation for a hyperboloid tip because the adhesion-induced indentation corresponds to the process of increasing of the contact area, which exhibits no tacky effect. Using Equations (3-14) and (3-15), one obtains the elasticity by the adhesion-induced indentation alone, i.e. the point "**0**" in Figure 3-2b, as long as the interfacial energy between the tip and the sample is known. The interfacial energy between SiO_2 (the out layer of the plasma cleaned Si_3N_4 tip) and PDMS is about 58 mJ/m^2. [52-54]

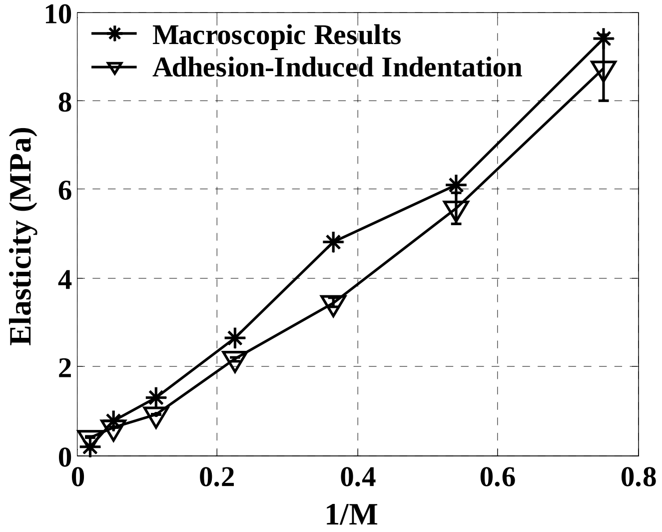

Figure 3-7. Elasticity for all PDMS samples obtained using the adhesion-induced indentation method and the correlation between the elasticity and the reciprocal of molecular weight of oligomeric precursor 1/M. Obtained through analysis such as in Figure 3-4, each plotted elasticity point in this figure represents the median value obtained from the corresponding force volume data at scan rate of 0.1Hz (K_c = 0.66 N/m, *R* = 58 nm) over an area of 5x5 μm^2 on a PDMS sample. The error bars provide the standard deviation of the mean of all the data in a force volume. The macroscopic results are taken from Vorvolakos [46].

The results are given in Figure 7. The moduli obtained from the adhesion-induced indentation are consistently slightly smaller than the macroscopic results, which could be due to an underestimate of the interfacial energy, but the results for the 253 DP and 705 DP samples are much closer to the macroscopic results than would be obtained using our AFM adhesion rupture method. This is interesting because it can provide an indirect way to obtain the elasticity for very tacky samples without dealing with the complicated viscoelastic effects, as long as the interfacial energy can be estimated. The method based on the adhesion-induced indentation is especially good for a series of samples which have same chemical composition but different moduli because the interfacial energy may be obtained from the less tacky samples once their elasticity values are known.

Using a spherical tip improves the applicability of the JKR-method-based elasticity measurements. The results obtained using the data collected by a spherical colloidal tip (Figure

3-5c) are closer to the macroscopic values than those where the JKR method was used for the data colleted by a regular AFM tip (Figure 3-5a). However, a large colloidal tip can reduce the ability of AFM to measure local sample elasticity at high spatial resolution. Because the colloidal tip was so large, the deformation of the samples was always quite small compared to the tip radius. This caused the JKR and Maugis's fits, where the latter is based on an accurate spherical profile, to be equivalent to each other, as one can see in Figure 3-5c.

In some cases, it is very difficult to unambiguously locate the contact point as seen in Figure 2a. Thus, it is not possible to obtain the absolute indentation value δ at each point on the AFM retraction force curve as seen in Figure 3-2b. In this case, fitting the whole retraction force curve for sample elasticity E and interfacial energy γ_{12} is a better method, without the need to know the absolute indentation value δ for each point on the force curve. As an example, Figure 3-8 shows the results of 25 DP PDMS.

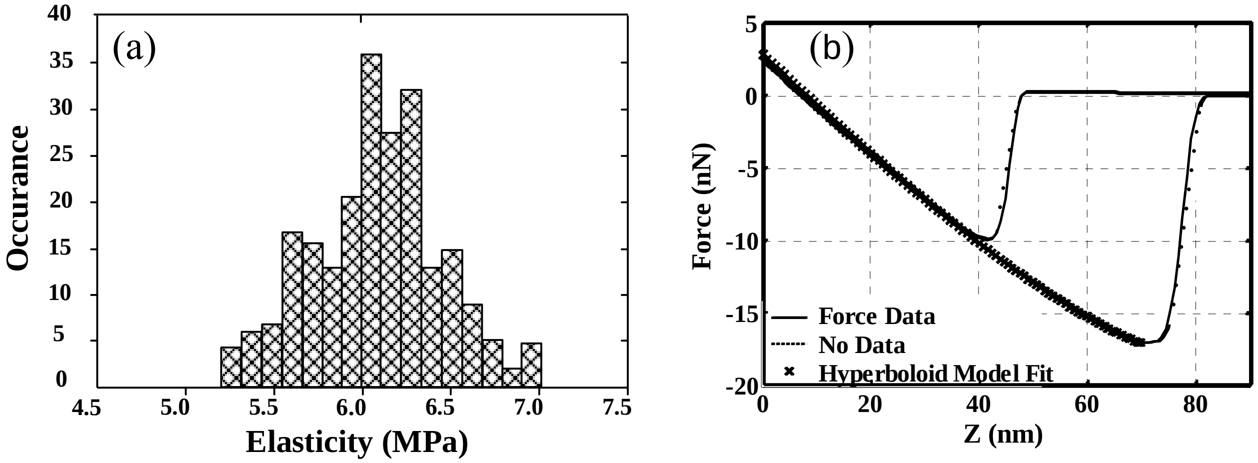

Figure 3-8. Elasticity E can be obtained by fitting the whole retraction curve without the need of knowing the absolute indentation value δ for each point on the force curve. (a) Result obtained for all force plots of 25 DP PDMS force volume data (same data as in Figure 3-4). (b) The averaged force plot (obtained by averaging all force plots in the force volume data) and its fitted curve using E = 6.05 MPa and γ_{12} = 60.5 mJ/m^2, which are the mean values obtained from the fit.

Figure 3-8a is the histogram of elasticity *E* (6.05 ± 0.36 MPa) obtained for all force plots of 25 DP PDMS force volume data (same data as in Figure 3-4). Figure 3-8b shows the averaged force plot (obtained by averaging all the force plots in the force volume data) and its fitting curve using $E = 6.05$ MPa and $\gamma_{12} = 60.5$ mJ/m^2, which are the mean values obtained from the fit. All fits are based on the model for a hyperboloid tip shape, *i.e.* Equations (3-14) and (3-15).

Following the style of Figure 3-4, Figure 3-9 shows a comparison of the macroscopic results, the hyperboloid 2-points method, and the hyperboloid whole curve fitting method.

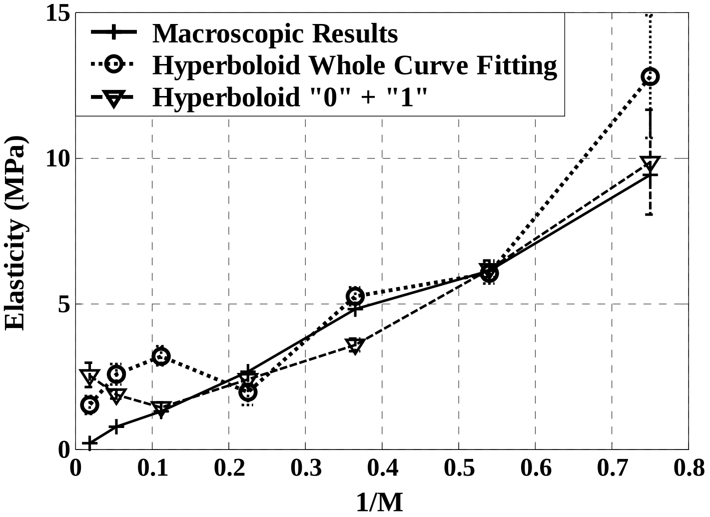

Figure 3-9. Comparison of elasticity for all PDMS samples obtained using different methods is plotted versus the reciprocal of molecular weight of the oligomeric precursor 1/M. The macroscopic results are taken from Vorvolakos[46].

From Figure 3-9, one can see that the hyperboloid 2-points method and the hyperboloid whole curve fitting method closely agree with the macroscopic results. One very interesting thing is that for soft polymers (120 DP, 253 DP, 705 DP PDMS samples), the two methods showed opposite trend in the elasticity values. This is probably due to the different ways of treating the viscoelastic effect in the two methods. However, this discussion is beyond the scope of this paper. The whole curve fitting method is very time consuming. In our case, it usually takes 5 hours to fit all force plots in a force volume data on a Pentium4 2.0 GHz computer. Therefore, we prefer to use the 2-points method, which takes only a few minutes to do a fit. However, as mentioned earlier, for cases when the contact point is hard to locate, the whole curve fitting method is necessary.

In addition to the tip shape and the adhesion hysteresis, there are several other factors that affect the applicability of this method, both practically and theoretically. These factors are the interfacial adhesive energy between the tip and sample, the relative stiffness of the cantilever and the sample, environmental humidity.

Because this model to evaluate elasticity of a sample is based on the tip-sample adhesion behavior, the adhesion between the tip and the sample should be enough to deform the cantilever and the sample measurably as the tip is pulled away from the sample surface. However, the adhesion should not be so much that the induced cantilever deflection is over the detection limit of the AFM for that cantilever, as was observed for the colloidal AFM tip, see Figure 3-10.

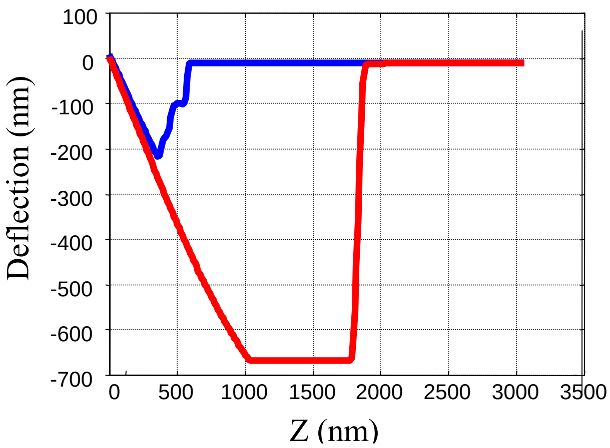

Figure 3-10. For an AFM cantilever with a small force constant, a large tip-sample adhesion causes the cantilever deflection beyond the detection limit of deflection.

The relative stiffness of the cantilever k_t and the sample k_s must be chosen to optimize the signal-to-noise of the force plots, which was discussed by Aime et al.[55]. There are two extreme cases. One is the fixed load case, $k_t << k_s$, in which pulling on the sample will not cause a noticeable deformation Δ. Another case is the fixed grid, $k_t >> k_s$, in which the cantilever deflection is kept close to zero as it is pulled off the surface. Since the effective sample stiffness $k_s = \left(\partial P / \partial \delta\right)_A$, where A is the contact area, depends on the magnitude of the contact area ($k_s = \frac{3}{2} aK$ for the JKR model, where $K = 4E/[3(1-v^2)]$), the relative stiffness of the cantilever and the sample should be estimated all-around by considering the tip radius, sample elasticity and their adhesion strength.

The capillary effect, which results from the condensation of water around the tip on hydrophilic surfaces, can be important in determining the tip-sample behavior.[56-57] However, because PDMS is very hydrophobic, this effect was not significant in our experiment. Jones, et al.[58] studied the dependence of pull-off force on relative humidity between a silicon AFM tip and a hydrophobic silicon surface and found that the pull-off force is almost constant over the entire range of relative humidity, which means the capillary effect is negligible for hydrophobic polymers.

3.6. Conclusion

Methods to calculate surface modulus based on the adhesive interaction between AFM tips and samples have been presented. The methods are useful for soft and thin samples because accurately locating the tip-sample contact point is not necessary when fitting the whole retraction force curve. The method introduced here has less interference from the substrate than does the indentation method. The analysis and discussion show that the adhesive interaction model works reasonably well. Without any correction, the results for moderately soft samples such as 18 DP, 25 DP, 37 DP, 60 DP and 120 DP PDMS samples, which have elastic moduli ranging between 10 MPa and 1 MPa, are very close to the results obtained from the macroscopic JKR method. Our model could benefit from the inclusion of the corrections for the viscoelastic effect, which caused errors a factor of 5 and a factor of 2 for the softest samples 705 DP and 253 DP PDMS samples respectively, and this will be examined later.

3.7. Appendix

1. Derivation of Equations (3-5) and (3-6) in the article text

As two elastic spheres contact, the adhesion and the external load causes an elastic deformation, and a contact area forms between the two elastic bodies. According to JKR theory, the contact radius *a* of the contact area is given by

$$a^3 = \frac{R}{K}\left[P + 3\pi R\gamma_{12} + \sqrt{6\pi RP\gamma_{12} + (3\pi R\gamma_{12})^2}\right] \tag{A3-1}$$

$$a_0^3 = 6\gamma_{12}\pi R^2 / K \tag{A3-2}$$

$$\delta = \frac{a^2}{R}\left[1 - \frac{2}{3}\left(\frac{a_0}{a}\right)^{3/2}\right] \tag{A3-3}$$

where P is the external load, γ_{12} is the interfacial energy, a_0 is the contact radius under zero external load, δ is the sample deformation, $R=R_1R_2/(R_1+R_2)$ is the normalized radius of the two spheres with radii of R_1 and R_2, $K=4/3\pi(k_1+k_2)$. k_1 and k_2 are the elastic constants of each sphere, that is

$$k_1 = \frac{1-\nu_1^2}{\pi E_1} \quad \text{and} \quad k_2 = \frac{1-\nu_2^2}{\pi E_2}$$

where ν is the Poisson ratio and E is the Young modulus of each material.

Under negative loads, the elastic spheres adhere until, at the critical negative force, P_{rupt}, the surfaces suddenly jump apart. The contact radius a_{rupt} at the rupture point is given by

$$a_{rupt} = a_0 / 4^{1/3} = 0.63 a_0 \qquad \text{(A3-4)}$$

and the adhesion force P_{rupt} is given by

$$P_{rupt} = -\frac{3}{2}\pi R^2 \gamma_{12} \qquad \text{(A3-5)}$$

The equations above are the general conclusions from the JKR theory.

Combining Equations (A3-2), (A3-3) and (A3-5), one obtains the deformation δ_0 under a zero load as

$$\delta_0 = \frac{a_0^2}{3R} = \frac{(6\gamma_{12}\pi R^2 / K)^{2/3}}{3R} = \frac{1}{3}\sqrt[3]{\frac{16 \cdot P_{rupt}^2}{K^2 R}} \qquad \text{(A3-6)}$$

Similarly, combining Equations (A3-2), (A3-3), (A3-4) and (A3-5), one obtains the deformation δ_{rupt} at the rupture point as

$$\delta_{rupt} = \frac{a_{rupt}^2}{R}\left[1 - \frac{2}{3}\left(\frac{a_0}{a_{rupt}}\right)^{3/2}\right] = -\frac{1}{3}\cdot\frac{a_0^2}{4^{2/3} R} = -\frac{1}{3}\sqrt[3]{\frac{P_{rupt}^2}{K^2 R}} \qquad \text{(A3-7)}$$

Equations (A3-6) and (A3-7) are the Equations (3-5) and (3-6) in the main text.

2. The derivation of the dependence of the load and indentation on the contact radius for a hyperboloid tip.

As in reference[38], we used the Sneddon equations to characterizing an axisymmetric hyperboloid punch indenting an elastic half-space. For a indenter whose profile is given by *f(x)* ($x=r/a$, a is the contact radius), Sneddon has shown the indentation δ in the elastic half-space and the corresponding load P are given by

$$\delta = \int_0^1 \frac{f'(x)dx}{\sqrt{1-x^2}} + \frac{\pi}{2}\chi(1) \qquad \text{(A3-8)}$$

$$P = \frac{\pi a E}{1-\nu^2}\int_0^1 \chi(t)dt \tag{A3-9}$$

where

$$\chi(t) = \frac{2}{\pi}\left[\delta - t\int_0^t \frac{f'(x)dx}{\sqrt{t^2-x^2}}\right] \tag{A3-10}$$

where E and ν are the Young modulus and Poisson ration of the elastic half-space respectively. According to Griffith's criterion[37] and discussions in other references[59,60], the energy release rate G during a Griffith elastic fracture propagation is given by

$$G = \frac{\pi E}{8a(1-\nu^2)}\chi^2(1) \tag{A3-11}$$

The profile function for a hyperboloid tip is given by

$$f(x) = R\cot^2\alpha\left[\sqrt{(ax/R\cot\alpha)^2+1}-1\right] \tag{A3-12}$$

where R is the radius of the curvature of the tip apex, and α is the tip semivertical angle. Set $A=R\cot\alpha$, Equation (A3-12) becomes

$$f(x) = \frac{A^2}{R}\left[\sqrt{(ax/A)^2+1}-1\right] \tag{A3-13}$$

and

$$f'(x) = \frac{a^2}{R}\frac{x}{\sqrt{(ax/A)^2+1}} \tag{A3-14}$$

Inserting Equation (A3-14) in equation (A3-11), one obtains

$$G = \frac{\pi E}{8a(1-\nu^2)}\chi^2(1) = \frac{E}{2\pi a(1-\nu^2)}\left[\delta - \frac{aA}{2R}\left[\frac{\pi}{2}+\arcsin\left(\frac{(a/A)^2-1}{(a/A)^2+1}\right)\right]\right]^2 \tag{A3-15}$$

Writing the equilibrium as $G=\gamma_{12}$, with γ_{12} the interfacial energy, one obtains

$$\delta = \frac{aA}{2R}\left[\frac{\pi}{2} + \arcsin\left(\frac{(a/A)^2 - 1}{(a/A)^2 + 1}\right)\right] - \sqrt{\frac{2a\pi(1-\nu^2)\gamma_{12}}{E}} \tag{A3-16}$$

Combining Equation (A3-9) and (A3-10), one can solve the load P

$$\begin{aligned} P &= \frac{2aE}{1-\nu^2}\left[\delta - \int_0^1 t\int_0^t \frac{f'(x)dx}{\sqrt{t^2 - x^2}}dt\right] = \frac{2aE}{1-\nu^2}\left[\delta - \int_0^1 \sqrt{1-x^2}\, f'(x)dx\right] \\ &= \frac{2E}{1-\nu^2}\left[a\delta - \frac{A}{2R}\left[\frac{a^2 + A^2}{2}\left(\frac{\pi}{2} + \arcsin\left(\frac{(a/A)^2 - 1}{(a/A)^2 + 1}\right)\right) - aA\right]\right] \end{aligned} \tag{A3-17}$$

Putting Equation (A3-16) in (A3-17), one obtains

$$P = \frac{2E}{1-\nu^2}\left[\frac{A}{2R}\left[aA + \frac{a^2 - A^2}{2}\left(\frac{\pi}{2} + \arcsin\frac{(a/A)^2 - 1}{(a/A)^2 + 1}\right)\right] - a\sqrt{\frac{2a\pi(1-\nu^2)\gamma_{12}}{E}}\right] \tag{A3-18}$$

3. An example showing detailed computation using the 2-points method for any two points on the retraction force curve.

In Figure 3-11, two arbitrary points “1” and “2” are chosen on the retraction force curve. We use subscripts to denote the related contact radius a, indentation δ, and external force P at each point. For instance, a_1, δ_1, and P_1 are the contact radius, indentation, and external force at point “**1**” respectively in Figure 3-11.

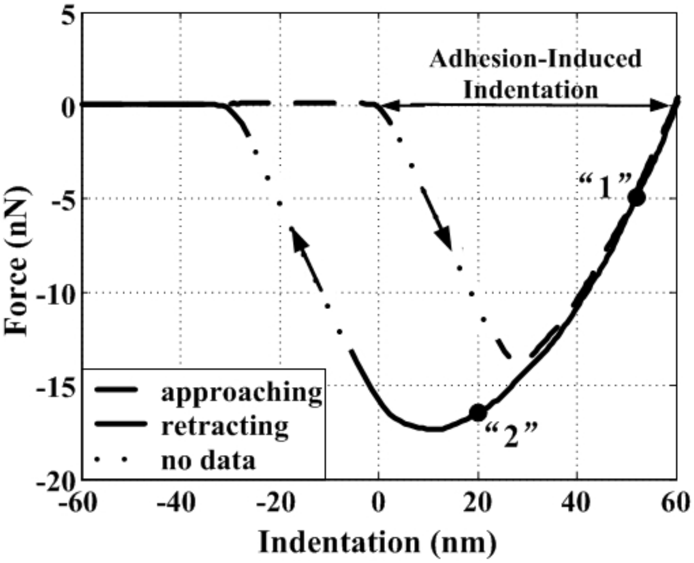

Figure 3-11. A typical AFM indentation vs. force plot for the case of an AFM tip interacting with a soft sample under adhesive interaction. The forces on the AFM tip as it approaches the surface are indicated by the dashed lines while the forces upon retraction are shown by the solid lines. Points "1" and "2" are arbitrarily chosen on the retraction force curve.

We take the case of hyperboloid tip shape as an example. For hyperboloid tip shape, the relationships of the δ-a and of P-a are given by:

$$\delta = \frac{aA}{2R}\left[\frac{\pi}{2} + \arcsin\left(\frac{(a/A)^2 - 1}{(a/A)^2 + 1}\right)\right] - \sqrt{\frac{2a\pi(1-v^2)\gamma_{12}}{E}} \qquad \text{(A3-19)}$$

and

$$P = \frac{2E}{1-v^2}\left[a\delta - \frac{A}{2R}\left[\frac{a^2+A^2}{2}\left(\frac{\pi}{2} + \arcsin\frac{(a/A)^2-1}{(a/A)^2+1}\right) - aA\right]\right] \qquad \text{(A3-20)}$$

where δ and P are the indentation and the load respectively. R is the tip radius of curvature, $A=R\cdot\cot(\alpha)$, α is the tip semivertical angle, v is the Poisson ratio of the sample, E is the elastic modulus of the sample, a is the contact radius, and γ_{12} is the interfacial energy of the tip and the sample.

Here, we combine points “1” and “2” to show how to perform the 2-points method.

At point “1”, the external load P_1 and indentation δ_1 are given by

$$P_1 = \frac{2E}{1-v^2}\left[a_1\delta_1 - \frac{A}{2R}\left[\frac{{a_1}^2 + A^2}{2}\left(\frac{\pi}{2} + \arcsin\frac{(a_1/A)^2 - 1}{(a_1/A)^2 + 1}\right) - a_1 A\right]\right] \tag{A3-21}$$

$$\delta_1 = \frac{a_1 A}{2R}\left[\frac{\pi}{2} + \arcsin\left(\frac{(a_1/A)^2 - 1}{(a_1/A)^2 + 1}\right)\right] - \sqrt{\frac{2a_1\pi(1-v^2)\gamma_{12}}{E}} \tag{A3-22}$$

Similarly, at point “2”, the external load P_2 and indentation δ_2 are given by

$$P_2 = \frac{2E}{1-v^2}\left[a_2\delta_2 - \frac{A}{2R}\left[\frac{{a_2}^2 + A^2}{2}\left(\frac{\pi}{2} + \arcsin\frac{(a_2/A)^2 - 1}{(a_2/A)^2 + 1}\right) - a_2 A\right]\right] \tag{A3-23}$$

$$\delta_2 = \frac{a_2 A}{2R}\left[\frac{\pi}{2} + \arcsin\left(\frac{(a_2/A)^2 - 1}{(a_2/A)^2 + 1}\right)\right] - \sqrt{\frac{2a_2\pi(1-v^2)\gamma_{12}}{E}} \tag{A3-24}$$

Combine Equations (A3-21) and (A3-23), one obtains

$$\frac{P_1}{P_2} = \frac{a_1\delta_1 - \frac{A}{2R}\left[\frac{{a_1}^2 + A^2}{2}\left(\frac{\pi}{2} + \arcsin\frac{(a_1/A)^2 - 1}{(a_1/A)^2 + 1}\right) - a_1 A\right]}{a_2\delta_2 - \frac{A}{2R}\left[\frac{{a_2}^2 + A^2}{2}\left(\frac{\pi}{2} + \arcsin\frac{(a_2/A)^2 - 1}{(a_2/A)^2 + 1}\right) - a_2 A\right]} \tag{A3-25}$$

Combine Equations (A3-22) and (A3-24), one obtains

$$\frac{\delta_1 - \frac{a_1 A}{2R}\left[\frac{\pi}{2} + \arcsin\left(\frac{(a_1/A)^2 - 1}{(a_1/A)^2 + 1}\right)\right]}{\delta_2 - \frac{a_2 A}{2R}\left[\frac{\pi}{2} + \arcsin\left(\frac{(a_2/A)^2 - 1}{(a_2/A)^2 + 1}\right)\right]} = \sqrt{\frac{a_1}{a_2}} \tag{A3-26}$$

Combine Equations (A3-25) and (A3-26), one can obtain a_1 and a_2. Then put a_1 in Equation (A3-21) or a_2 in Equation (A3-23), one can obtain the sample elasticity E.

For example, for the points “1” and “2” in Figure 3-11, using the method above, we obtained a1 = 112.3 nm, a2 = 91.2 nm, and E = 3.4 MPa.

4. Characterization of surface roughness of PDMS samples used in the paper:

The characterization was done using the same DI Dimension 3100 AFM with the tapping mode and given in Figure 3-12. A 40N/m (manufacturer’s nominal value) silicon tapping mode cantilever was used. Scan sizes were 5x5 μm^2 and 10x10 μm^2. Scan rate was 0.25 Hz.

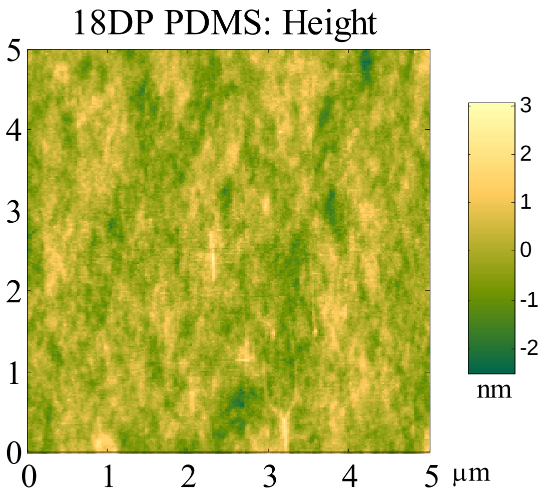
18DP PDMS: Height

RMS Roughness = 0.54 nm

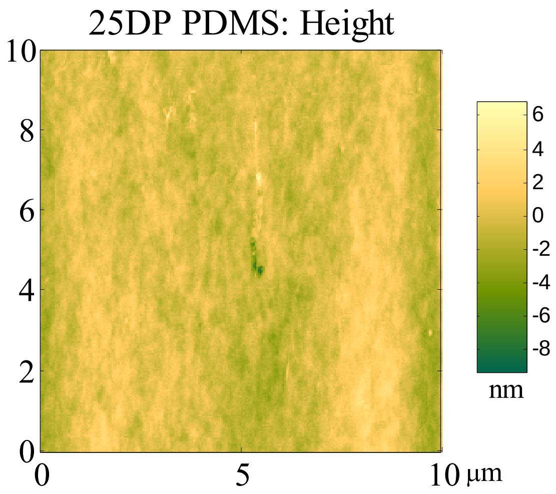
25DP PDMS: Height

RMS Roughness = 1.1 nm

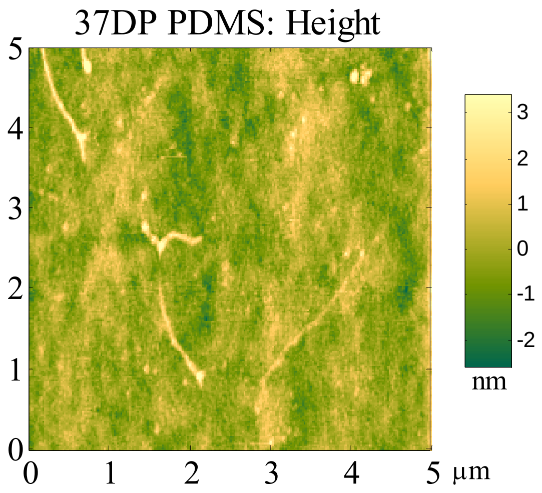
37DP PDMS: Height

RMS Roughness = 0.69 nm

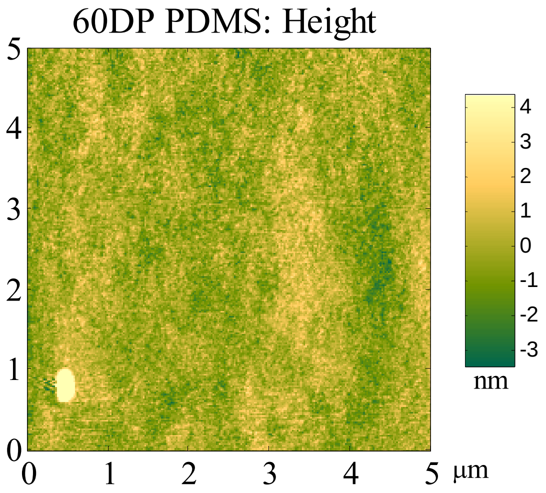
60DP PDMS: Height

RMS Roughness = 0.83 nm

cut out the high spot

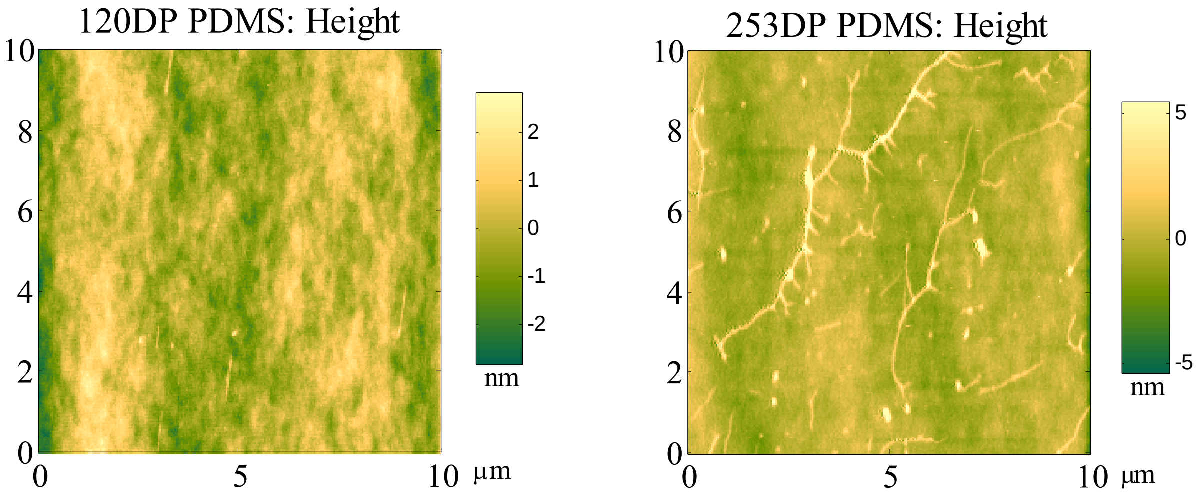
120DP PDMS: Height

253DP PDMS: Height

RMS Roughness = 0.74 nm

RMS Roughness = 1.1 nm

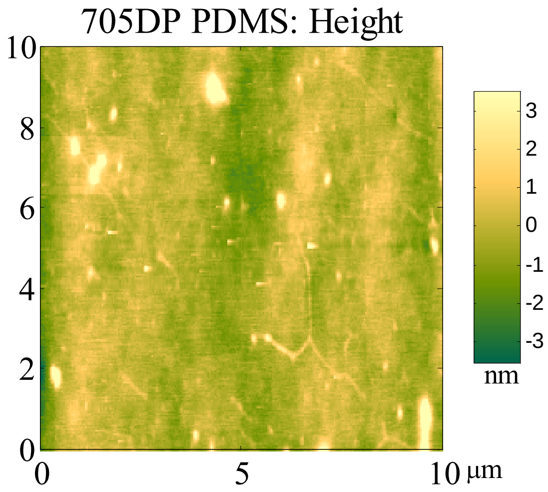
705DP PDMS: Height

RMS Roughness = 0.83 nm
cut out the two high spots

Figure 3-12. Surface roughness of PDMS samples. Images were collected using AFM tapping mode imaging.

5. Discussion of the validity of the continuum mechanics during the sharp tip indenting in a polymer network.

The sample we discussed in Figure 3-6 of the article text is the 120 DP PDMS. Taking its density 1g/cm^3 (more precisely 0.9697g/cm^3) and the molecular weight of its oligomer 8.88kg/mol, one can approximately get the volume of each chain between cross-links under unstreched state. The value is about 15.15 nm^3. The average contour length of each chain between cross-links can be estimated by (O-Si-O bond length) x sin(π/3) x DP ≈ 35 nm. Therefore, it is easily seen that the chains are highly coiled and can hold its continuum mechanical property under large deformation. In addition, as seen in Figure 3-13 below, under an adhesion-induced stress, the cross-lined network (280nm) is stretched to 500nm, where $\Delta l/l_0=(500-280)/280=0.8$.

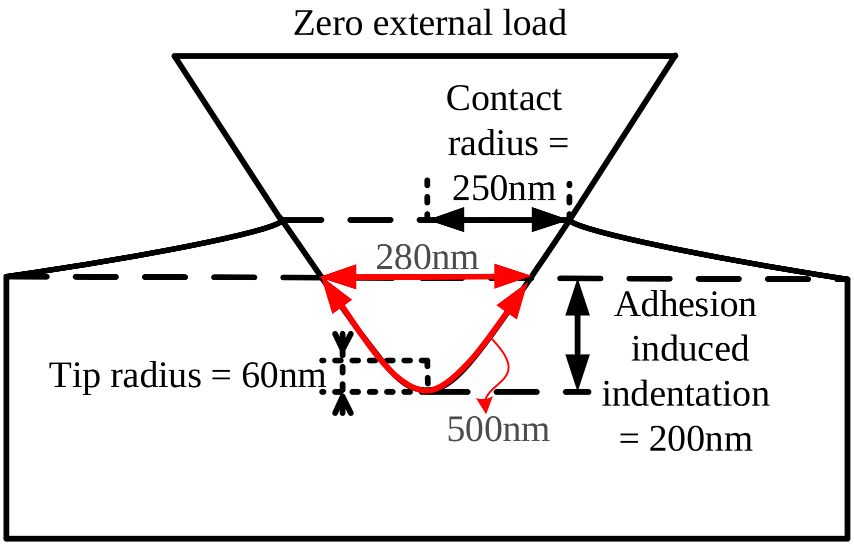

Figure 3-13. The adhesion-induced indentation of the adhesion-induced indentation of AFM tips on 120 DP PDMS.

Referring to Figure 3-14, a typical stress-strain curve of elastomers, (Treloar, L. R. G. The Physics of Rubber Elasticity, Oxford, Clarendon Press, 1975; Bensason, S.; Stepanov, E. V.; Chum, S.; Hiltner, A.; Baer, E. Macromolecules 1997, 30, 2436-2444), the stress-strain behavior in our experiment is still in the region where continuum mechanics is expected to hold.

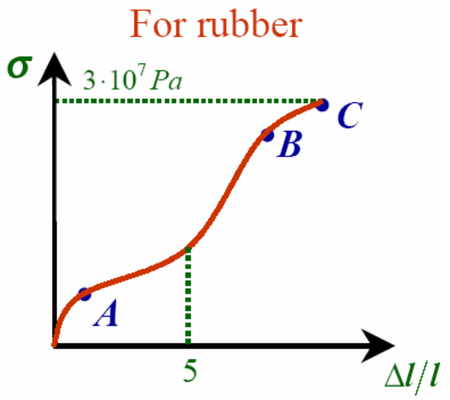

Figure 3-14. Typical stress-strain curves. A - upper limit for stress-strain linearity; B - upper limit for reversibility of deformations; C - fracture point.

Figure 3-14 also implies another advantage of the method that is one can obtain the elasticity of the sample more accurately than using the indentation method if the indentation in the sample breaks stress-strain linearity of the sample, or makes it fracture.

BIBLIOGRAPHY

1. Touhami, A.;Nysten, B.;Dufrene, Y. F. *Langmuir* **2003**, *19*, 4539-4543.

2. Hurley, D. C.;Shen, K.;Jennett, N. M.;Turner, J. A. *J. Appl. Phys.* **2003**, *94*, 2347-2354.

3. Salvadori, M. C.;Brown, I. G.;Vaz, A. R.;Melo, L. L.;Cattani, M. *Phys. Rev. B* **2003**, *67*, 153404.

4. Du, B.;Ophelia, K. C.;Zhang, Q.;He, T. *Langmuir* **2001**, *17*, 3286-3291.

5. Vinckier, A.;Semenza, G. *FEBS Lett.* **1998**, *430*, 12-16.

6. Nie, H. Y.;Motomatsu, M.;Mizutani, W.;Tokumoto, H. *Thin Solid Films* **1996**, *273*, 143-148.

7. Domke, J.;Radmacher, M. *Langmuir* **1998**, *14*, 3320-3325.

8. Bowen, W. R.;Lovitt, R. W.;Wright, C. J. *Biotechnol. Lett.* **2000**, *22*, 893-903.

9. Rixman, M.;Dean, D.;Macias, C.;Ortiz, C. *Langmuir* **2003**, *19*, 6202-6218.

10. Ortiz, C.;Hadziioannou, G. *Macromolecules* **1999**, *32*, 780-787.

11. Al-Mawaali, S.;Bemis, J.;Akhremitchev, B. B.;Janesko, B.;Walker, G. C. *J. Phys. Chem. B* **2001**, *105*, 3965-3971.

12. Vanlandingham, M. R.;Villarrubia, J. S.;Guthrie, W. F.;Meyers, G. F. *Macromol. Symp.* **2001**, *167*, 15-43.

13. A-Hassan, E.;Heinz, W. F.;Antonik, M. D.;Dcosta, N. P.;Nageswaran, S.;Schoenenberger, C.-A.;Hoh, J. H. *Biophys. J.* **1998**, *74*, 1564-1578.

14. Tomasetti, E.;Legras, R.;Nysten, B. *Nanotechnology* **1998**, *9*, 305-315.

15. Fraxedas, J.;Garcia-Manyes, S.;Gorostiza, P.;Sanz, F. *Proc. Natl. Acad. Sci. USA* **2002**, *99*, 5228-5232.

16. Pietrement, O.;Troyon, M. *J. Colloid Interface Sci.* **2000**, *226*, 166-171.

17. Tamayo, J.;Garcia, R. *Appl. Phys. Lett.* **1997**, *71*, 2394-2396.

18. Magonov, S. N.;Elings, V.;Whangbo, M. H. *Surf. Sci.* **1997**, *375*, L385-L391.

19. Akhremitchev, B. B.;Brown, H. G.;Graner, S. R.;Walker, G. C. *Microsc. Microanal.* **2001**, *7*, 32-38.

20. Mahaffy, R. E.;Shih, C. K.;Mackintosh, F. C.;Kas, A. J. *Phys. Rev. Lett.* **2000**, *85*, 880-883.
21. Galuska, A. A.;Poulter, R. R.;Mcelrath, K. O. *Surf. Interface Anal.* **1997**, *25*, 418-429.

22. Jourdan, J. S.;Cruchon-Dupeyrat, S. J.;Huan, Y.;Kuo, P. K.;Liu, G. Y. *Langmuir* **1999**, *15*, 6495-6504.

23. Tabor, D. *J. Colloid Interface Sci.* **1977**, *58*, 2-13.

24. Moy, V. T.;Jiao, Y.;Hillmann, T.;Lehmann, H.;Sano, T. *Biophys. J.* **1999**, *76*, 1632-1638.

25. Domkea, J.;Dannohla, S.;Paraka, W. J.;Muller, O.;Aicher, W. K.;Radmacher, M. *Colloids Surf., B: Biointerfaces* **2000**, *19*, 367-379.

26. Eaton, P.;Smith, J. R.;Graham, P.;Smart, J. D.;Nevell, T. G.;Tsibouklis, J. *Langmuir* **2002**, *18*, 3387-3389.

27. Scheffer, L.;Bitler, A.;Ben-Jacob, E.;Korenstein, R. *Single Mol.* **2000**, *1*, 176.

28. Hertz, H. *J. Reine Angew. Math.* **1882**, *92*, 156.

29. Rimai, D. S.;Quesnel, D. J.;Bowen, R. C. *Langmuir* **2001**, *17*, 6946-6952.

30. Rimai, D. S.;Demejo, L. P.;Bowen, R. C. *J. Appl. Phys.* **1989**, *66*, 3574-3578.

31. Cuenot, S.;Demoustier-Champagne, S.;Nysten, B. *Phys. Rev. Lett.* **2000**, *85*, 1690-1693.

32. K.L.Johnson;Kendall, K.;Roberts, A. D. *Proc. R. Soc. London, Ser. A* **1971**, *324*, 301-313.

33. Weisenhornt, A. L.;Khorsandit, M.;Kasast, S.;Gotzost, V.;Butt, H.-J. *Nanotechnology* **1993**, *4*, 106-113.

34. Rimai, D. S.;Demejo, A. L. P.;Vreeland, W.;Bowen, R.;Gaboury, S. R.;Urban, P. W. *J. Appl. Phys.* **1992**, *71*, 2253-2258.

35. Johnson, K. L.;Sridhar, I. *J. Phys., D: Appl. Phys.* **2001**, *34*, 683-689.

36. Maugis, D. *Langmuir* **1995**, *11*, 679-682.

37. Swedlow, J. L. *Int. J. Fracture Mech.* **1965**, *1*, 210-216.

38. Sneddon, I. N. *Int. J. Engng Sci.* **1965**, *3*, 47-57.

39. Toriiy, A.;Sasakiz, M.;Hanex, K.;Okumaz, S. *Meas. Sci. Technol.* **1996**, *7*, 179-184. 40. Hutter, J. L.;Bechhoefer, J. *Rev. Sci. Instrum.* **1993**, *64*, 1868-1873.

41. Gibson, C. T.;Watson, G. S.;Myhra, S. *Nanotechnology* **1996**, *7*, 259-262.

42. Cleveland, J. P.;Manne, S.;Bocek, D.;Hansma, P. K. *Rev. Sci. Instrum.* **1993**, *64*, 403-405.

43. Sadera, J. E.;Chon, J. W. M.;Mulvaney, P. *Rev. Sci. Instrum.* **1999**, *70*, 3967-3969.

44. Craig, V. S. J.;Neto, C. *Langmuir* **2001**, *17*, 6018-6022.

45. Ramirez-Aguilar, K. A.;Rowlen, K. L. *Langmuir* **1998**, *14*, 2562-2566.

46. Vorvolakos, K.;Chaudhury, M. K. *Langmuir* **2003**, *19*, 6778-6787.

47. Radmacher, M.;Fritz, M.;Cleveland, J. P.;Walters, D. A.;Hansma, P. K. *Langmuir* **1994**, *10*, 3809-3814.

48. Ducker, W. A.;Senden, T. J.;Pashley, R. M. *Langmuir* **1992**, *8*, 1831-1836.

49. Muster, T. H.;Toikka, G.;Hayes, R.;Prestidge, C. A.;Ralston, J. *Colloids Surf., A* **1996**, *106*, 203-211.

50. Toikka, G.;Hayes, R. A.;Ralston, J. *Langmuir* **1996**, *12*, 3783-3788.

51. Barquins, M.;Maugis, D. *J. Adhesion* **1981**, *13*, 53-65.

52. Fowkes, F. M., *Chemistry and Physics of Interfaces*. 1965, American Chemical Society: Washington, D.C. p. 1-12.

53. Papirer, E.;Balard, H., *The Surface Properties of Silicas*, A.P. Legrand, Editor. 1998, Wiley: New York. p. 315-364.

54. Owens, D. K.;Wendt, R. C. *J. Appl. Polym. Sci.* **1969**, *13*, 1741-1747.

55. Aime, J. P.;Elkaakour, Z.;Odin, C.;Bouhacina, T.;Michel, D.;Curbly, J.;Dautant, A. *J. Appl. Phys.* **1994**, *76*, 754-762.

56. Gulbinski, W.;Pailharey, D.;Suszko, T.;Mathey, Y. *Surf. Sci.* **2001**, *475*, 149-158.

57. Piner, R. D.;Mirkin, C. *Langmuir* **1997**, *13*, 6864-6868.

58. Jones, R.;Pollock, H. M.;Cleaver, J. A. S.;Hodges, C. S. *Langmuir* **2002**, *18*, 8045-8055.

59. Maugis, D.;Barguins, M. *J. Phys. D: Appl. Phys.* **1984**, *16*, 1843-1850

60. Maugis, D. *J. Colloid and Interface Sci.* **1992**, *150*, 243-251

Chapter 4. Viscoelastic Response of Poly-(dimethylsiloxane) in Adhesive Interaction with AFM tips

Abstract

Following on the study in Chapter 3, the viscoelastic response of cross-linked poly-(dimethylsiloxane) (PDMS) in adhesive interaction with AFM tips is reported. The indentation of the AFM tip into the polymer caused by adhesion is monotonically dependent on the loading speed. During the unloading process, the adherence force between the AFM tip and the polymer has a turning point at a specific unloading speed. It is found that the viscoelastic relaxation processes in the bulk polymer, which may have more than one component, cause the monotonic rate dependence of the adhesion-induced indentation; the competition between the bulk relaxation and the interfacial relaxation results in the turning point of the adherence force at a specific ramp speed. Experiments at different dwell times provide evidence for existence of material relaxation. Methyl and hydroxyl functionalized AFM tips were used to study PDMS samples and indicated strong dipolar attractions formed at the tip-sample interface.

4.1. Introduction

The atomic force microscope (AFM) can be used to measure the elasticity of surfaces. In the study discussed in Chapter 3, we proposed a model to measure the surface elastic modulus of compliant samples at the nanoscale based on their adhesive interactions with atomic force microscope (AFM) tips. Cross-linked poly(dimethylsiloxane) (PDMS) elastomers with different cross-link density were studied. It was found that the model could not account for viscoelastic effects when AFM tips interact with PDMS samples with low cross-link density, *i.e.*, large molecular weights between cross-links.

During AFM tip loading and unloading on polymer surfaces under adhesive interactions, the main sources of energy dissipation are configurational relaxation in the bulk polymer material and dissipative processes at the tip of crack propagation, which can be determined kinetically, thermodynamically, or in a coupled manner. The adhesive interaction and elastic deformation are related[1-3]. A number of models have been developed to describe the elastic and relaxation properties of cross-linked polymer networks. The phantom model assumes that the cross-linkers are completely free to move in space[4,5] and $E=(\upsilon-\mu)RT$, where υ is the number of moles of chains per unit volume and μ is the number of moles of cross-linkers per unit volume. At the opposite extreme, the affine model assumes that the cross-linkers are confined to fixed locations and move affinely under deformation[6] and $E=\upsilon RT$.

For real networks, fluctuations of the cross-linker junctions are partially suppressed by entanglements of the strands, which is described by the constrained junction model[7,8]. When the strands between two neighboring cross-linkers are longer than a critical chain length, interchain entanglements may significantly affect the motion of the cross-linkers and the modulus. One of the most successful theories to treat the interchain entanglements is the reptation model initially proposed by de Gennes[9] and Doi and Edwards[10]. The theory of reptation theory models confines the motion of a polymer chain within a tube formed by neighboring polymer chains, see Figure 4-1. The chain's diffusion coefficient is proportional to the inverse square of the molecular weight and the longest relaxation time is proportional to the cube of the molecular weight.

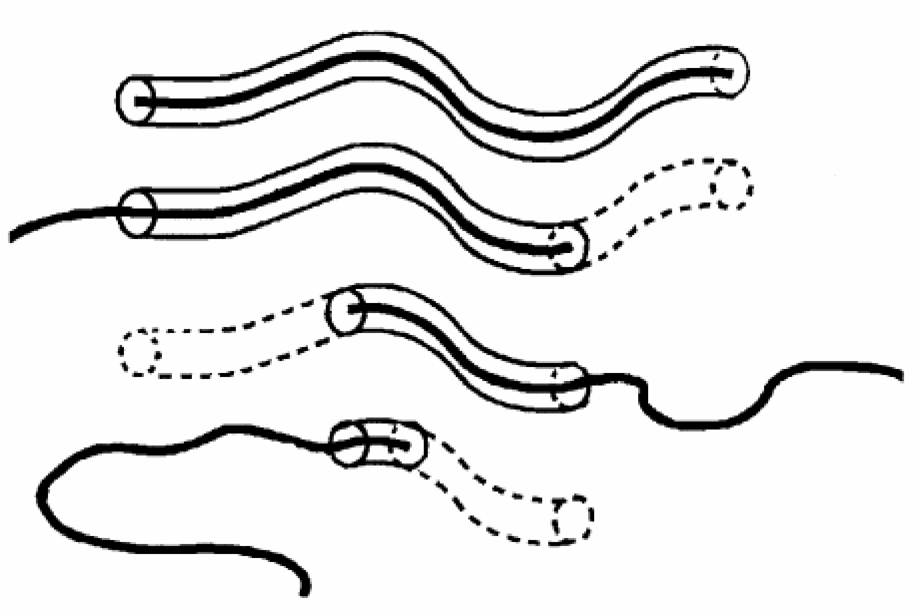

Figure 4-1. The reptation model for polymer relaxation assumes that the motion of a polymer chain is confined within a tube formed by neighboring polymer chains

The diffusion behavior of unentangled polymer systems can be described by the Rouse model[11], in which the polymer chains are modeled as series of beads joined by springs, see Figure 4-2. The diffusion coefficient is proportional to the inverse of the molecular weight.

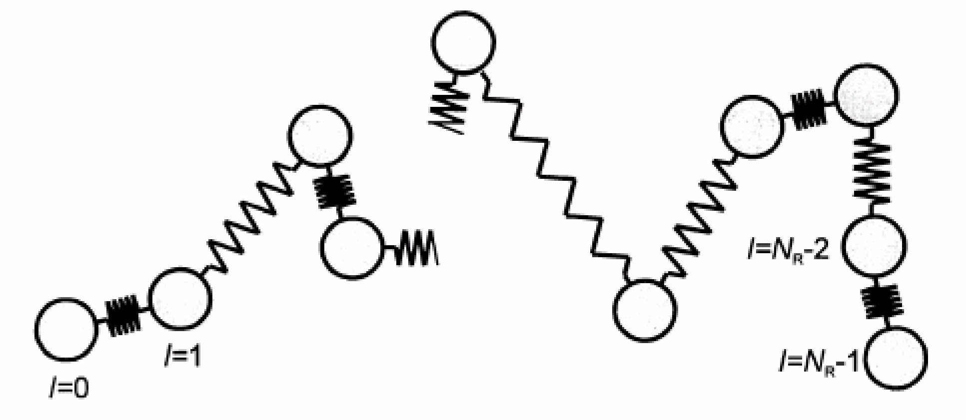

Figure 4-2. The Rouse model assumes that a polymer chain composed of many beads connected by springs. The beads experience elastic forces from the beads and friction forces from the surrounding.

In many dynamic adhesion processes, it is found that more energy is required to separate two surfaces in adhesive contact than is released when they come into contact. This is usually manifested as a hysteresis between the loading and unloading force versus separation force curves in a force measurement. Adhesion hysteresis is widely believed to be due to the energy dissipation in the bulk material and at the crack tip. A number of mechanisms have been proposed to explain the adhesion hysteresis. For instance, viscoelastic or plastic bulk deformation, the formation of weak or strong dipolar attractions at the interface, and cross-linking or physical entangling of tethered chains across the interface. These mechanisms are usually coupled in a practical adhesion system. Considerable work has been done to investigate different mechanisms for the adhesion hysteresis qualitatively or quantitatively. Silberzan *et al.*[12], Choi *et al.*[13-15], Kim *et al.*[16], Mason *et al.*[17], and Perutz *et al.*[18,19] studied the adhesion hysteresis of PDMS-PDMS self-adhesion systems and PDMS self-assembled monolayer systems using the macroscopic JKR method. In those experiments, polymer cross-link density, sol fraction, surface functionality, loading and unloading rates, and the dwell time of contact were varied. Because the loading and unloading processes were controlled to follow a quasi-equilibrium process, the contributions to the adhesion hysteresis from the viscoelasticity of the bulk material were ignored. Instead, hydrogen bonds, cross-linking, and physical chain entanglements were found to dominate the adhesion hysteresis. Pickering and Vancso[20], Vakarelski *et al.*[21], Noel *et al.*[22], and Gillies *et al.*[23] used AFM to study the adhesion hysteresis of polymer systems and found that the viscoelasticity was the dominant factor.

In this chapter, the viscoelastic response of PDMS in adhesive interaction with AFM tips was studied. Loading and unloading rates, dwell time, and AFM tip surface functionality were varied. It is found that the loading and unloading force curves are functions of the loading and unloading rates and dwell times. This implies that the process is dominated by viscoelasticity. When the AFM tip indents into the polymer surface, the main energy dissipation is caused by viscoelastic relaxation processes in the bulk polymer, while when the AFM tip retracts away from the polymer, relaxation processes also occur at the tip-polymer interface in addition to viscoelastic processes in the bulk polymer. In this paper's section on materials and methods, details about samples and the experimental setup are provided. In the results and discussion section, we show the dependence of force curves on loading, unloading rates and dwelling times. Implications and comparisons with the results from other studies are discussed.

4.2. Materials and Methods

As described in Chapter 3, PDMS samples were kindly provided by Vorvolakos and Chaudhury (Lehigh University, Lehigh, Pennsylvania). The degree of polymerization (DP) of the samples are DP= 18, 25, 37, 60, 120, 253, and 705 (corresponding to molecular weights of the oligomeric precursor (kg/mol), M=1.33, 1.85, 2.74, 4.44, 8.88, 18.72, and 52.17, respectively).

A Dimension 3100 AFM with a Nanoscope III controller (Veeco Metrology, Santa Barbara, CA) and silicon nitride AFM tips (DNP, Veeco Metrology, Santa Barbara, CA) were used to collect the force curves. Before use, all tips were cleaned by argon plasma for 20 sec at a low power (180 W). Cantilever sensitivities were collected on a piece of sapphire before and after each experiment. The loading force on the AFM cantilever is obtained by multiplying the cantilever deflection by k_c, the force constant of the AFM cantilever. k_c can be obtained by several methods. We used Cleveland's method to calibrate the force constants of cantilevers. The tip radii were measured by a TG101 tip calibration grating (MikroMasch USA, Portland, Oregon).

When an AFM tip interacts with a soft sample, the sample can be deformed by the AFM tip under an adhesive interaction. A typical AFM force plot for such case is given in Figure 4-3a, where the force is obtained by multiplying the AFM cantilever deflection by the force constant of the cantilever, and Z is the piezocrystal extension and retraction distance relative to the reverse point of the force curve. The change of Z comprises the change of cantilever deflection d and of the sample deformation δ, *i.e.*, $\Delta Z = \Delta d + \Delta\delta$. Upon approach to the surface, the tip jumps to the surface at the point of mechanical instability, when the gradient of the interaction force exceeds the force constant of cantilever. Once the tip contacts the surface, the tip is suddenly pulled into the sample by the adhesive interaction between the tip and the sample. This is shown as the sharp decrease of the force on the AFM cantilever in the extension part of the force plot in Figure 4-3a. As discussed in Chapter 3, the gradient of the van der Waals attraction force at a few nanometers of tip-sample separation is less than the force constant of cantilever. On the other hand, the sudden snap-in depth of tip into the soft PDMS samples due to the interfacial adhesion upon contact is between 30 nm to 300 nm, which is much larger than the jump-to-contact distance induced by the van der Waals attraction force. Therefore, for simplicity, the point where the interaction becomes attractive is assigned to be the point where tip contacts the surface, as shown in Figure 4-3a. With the knowledge of the contact point, a regular AFM force plot can be converted into a force vs. indentation plot as shown in Figure 4-3b, for example. From Figure 4-3b, one can see that when the AFM tip is pulled away from the sample, the adhesive attraction deforms the soft polymer along the direction of the tip motion, and causes a negative indentation, *i.e.*, polymer extension under a tensile stress. At point “**0**”, where the AFM tip is drawn in the sample surface due to the adhesive interaction, the stored elastic energy and the surface energy are balanced, hence there is a zero external force on the AFM cantilever; the indentation between the point where the tip starts to contact the sample surface, and point “**0**” is defined as the adhesion-induced indentation. Point “**1**” corresponds to the adherence force, *i.e.*, the maximum negative force on the AFM cantilever.

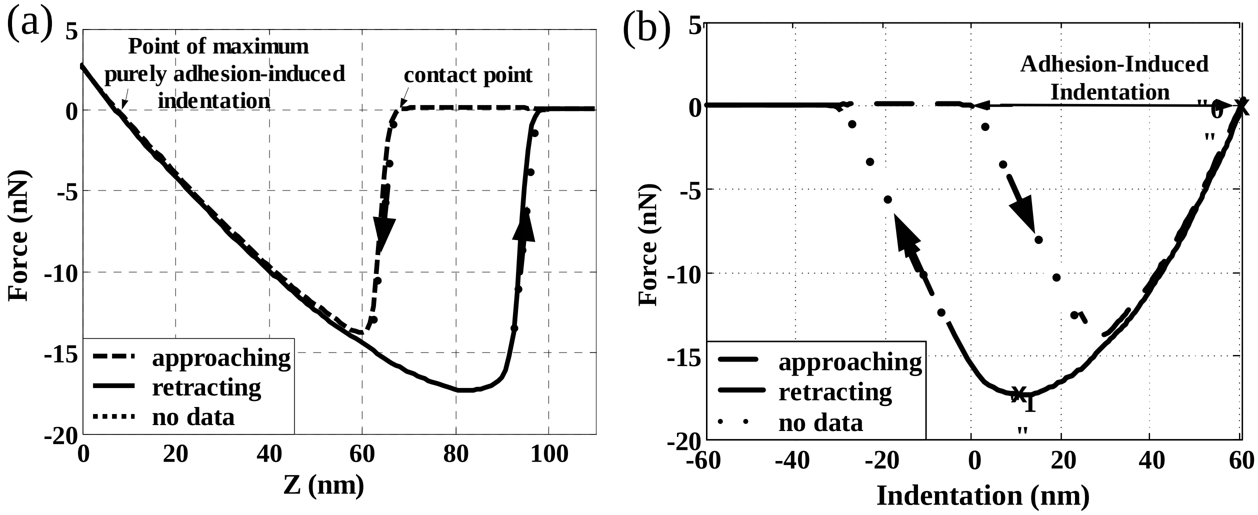

Figure 4-3. (a) A typical AFM force plot for the case of an AFM tip interacting with a soft sample under adhesive interaction (It is a DPN 0.6 N/m cantilever interacting with 37DP PDMS polymer in this case). (b) The corresponding force vs. indentation plot. Point “0” is where the AFM tip has zero external force. Point “1” corresponds to the adherence force.

The silicon nitride tip shape can be modeled by a hyperboloid. In our previous study, we solved the dependence of the load and indentation on the tip-sample contact radius using Griffith’s criterion and the method proposed by Sneddon. They are given in Equations (4-1) and (4-2).

$$\delta = \frac{aA}{2R}\left[\frac{\pi}{2} + \arcsin\left(\frac{(a/A)^2 - 1}{(a/A)^2 + 1}\right)\right] - \sqrt{\frac{2a\pi(1-v^2)w_0}{E}} \tag{4-1}$$

and

$$P = \frac{2E}{1-v^2}\left[\frac{A}{2R}\left[aA + \frac{a^2 - A^2}{2}\left(\frac{\pi}{2} + \arcsin\frac{(a/A)^2 - 1}{(a/A)^2 + 1}\right)\right] - a\sqrt{\frac{2a\pi(1-v^2)w_0}{E}}\right] \tag{4-2}$$

where δ and P are the indentation and the load respectively. R is the tip radius of curvature, $A=R\cdot cot(\alpha)$, α is the tip semivertical angle, v is the Poisson ratio of the sample, E is the elastic modulus of the sample, a is the contact radius, and w_0 is Dupré's work of adhesion. Equations (4-1) and (4-2) were derived for a static system under equilibrium or quasi-equilibrium conditions. However, by considering the rate dependence of the modulus and work of adhesion for crack propagation, the equations can be used for a dynamic system under adhesive interaction where Dupré's work of adhesion w is replaced by the strain energy release rate G. A detailed description is given in the section below named Results and Discussion. At any point on a force curve, the loading force P and indentation δ are known, and the contact radius a can be solved with knowledge of E or w_0 by combining Equations (4-1) and (4-2). The value of either E or w_0 can be obtained if the other is known. When E and w are both assumed to be constant along the retraction force curve, they can be solved by the "2-points method" or a fit to the whole retraction curve of the force plot as described in Chapter 3.

Because only the soft PDMS polymers 120DP, 253DP, and 705DP showed obvious viscoelastic behavior in the previous study, this investigation was focused on these three samples. Force curves at different ramp rates were collected at four randomly chosen locations on each sample. Five force plots were saved at each ramp rate. A few data were also collected on 60DP and 37DP for comparison. AFM tips were held in contact with the samples for different dwell times, and force curves were collected for the analysis of the influence of dwell times on the sample viscoelasticity. The ramp rates and dwell times were controlled with the integrated functions of the DI Nanoscope IIIA program (Version 4.43r8); the ramp rates along Z axis ranged between 0.01 Hz and 27.9 Hz. The maximum delay time for which the tip is held in contact with the sample is 250 seconds. Methyl and hydroxyl functionalized AFM tips

(Novascan Technologies, Inc., Ames, IA) were used to study the influence of dipolar interactions on the adhesion hysteresis. All force plots were collected under a trigger mode, in which the extension force curve reverses at a pre-assigned trigger value of cantilever deflection. To minimize the influence of the excessive compression of the tip to the samples, the trigger deflection value was set as small as possible, usually smaller than 5 nanometers, so the whole extension and retraction force curves can be considered to be governed by the adhesive interaction between the tip and samples. All experiments were done under ambient conditions at room temperature. The force plots were processed by custom software written using Matlab (The Mathworks, Inc., Novi, MI).

4.3. Results and Discussion

During the AFM tip loading process from the point of contact with the sample surface to the point where the loading force on the cantilever is zero, *i.e.*, the point "**0**" in Figure 4-3b, it is found that the adhesion- induced indentation of an AFM tip into the polymer is monotonically dependent on the ramp rates. Figure 4-4a shows this monotonic dependence of the extension force curves on ramp rates for the 705DP PDMS sample. In Figure 4-4a, Z is normalized, and the origin corresponds to the tip-sample contact point. As discussed above, the Z distance between the zero-deflection point and the origin is the adhesion-induced indentation for each ramp rate. A slower ramp rate corresponds to a larger adhesion-induced indentation. Unexpectedly, the retraction force curves during the unloading process did not show a monotonic dependence on the ramp rates. Instead, it was found that the adherence between the AFM tip and the polymer, *i.e.*, the maximum negative deflection point in the retraction force curve, has a turning point as a function of ramp rate. Figure 4-4b, the corresponding retraction force curves of the extension force curves in Figure 4-4a, shows a turning point at 0.8 Hz for the 705DP PDMS sample. In

Figure 4-4b, *Z* is normalized the same way as in Figure 4-4a. The turning point in Figure 4-4b implies that the behaviors of the retraction force curves are not just functions of the ramp rates. Because of the different dependence on ramp rates for the extension and retraction force curves, the results and discussions will be presented separately.

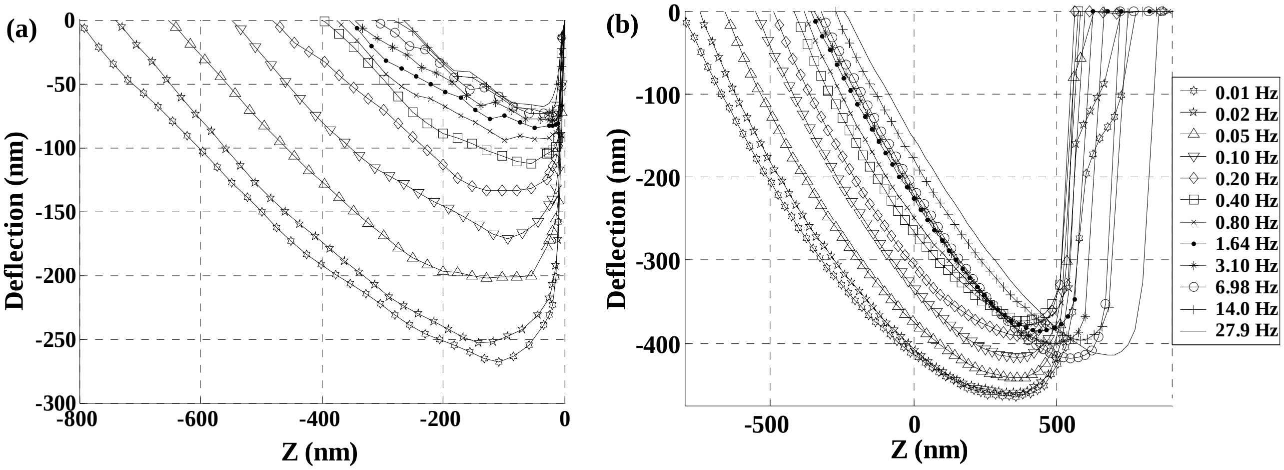

Figure 4-4. (a) Extension force curves at different ramp rates for the 705DP PDMS polymer. (b) Retraction force curves at different ramp rates corresponding to the extension force curves in (a) for the 705DP PDMS polymer. The extension and retraction force curves are plotted separately for easier visualization. *Z* is normalized, and the origin corresponds to the tip-sample contact point.

4.3.1. Studies and discussions of the extension force curves

When an AFM tip comes into contact with the soft PDMS surface, the interfacial adhesion suddenly snaps the tip into the sample, and the cantilever has an abrupt decrease in deflection as seen in the extension part of the force plot in Figure 4-3a. The cantilever applies a tensile stress to the polymer. As the piezocrystal extends, the dynamic competition between the interfacial adhesive force, the cantilever Hookean force, and the polymer elastic repulsive force results in the profile of the extension force curve of the cantilever in Figure 4-1a, in which the tip is drawn in deeper and deeper and the cantilever deflection becomes less and less negative, until the zero cantilever deflection point where the interfacial adhesive force and the polymer elastic repulsive force are balanced dynamically. At different ramp rates, the tip takes different times to reach the zero cantilever deflection point. The indentation vs. time curves for each scan rate from the contact point to the zero cantilever deflection point are converted from Figure 4-4a and plotted in Figure 4-5a. The change of indentation with time is shown by set of solid lines that cascade from the left (fast ramp rates) to right (slow ramp rates). The open circles at the end of each solid line correspond to the adhesion-induced indentation for each ramp rate. Any of the solid lines in Figure 4-5a can be considered equally as due to a particle, which is attached to a continuously varying external tensile force, sitting on a compliant sample, where the contact area changes with time as a result of creep under variable stress. Since the open circles in Figure 4-5a correspond to the adhesion-induced indentation where the external tensile forces are zero, the dashed line which connects the open circles indicates the path of the time dependent indentation of a particle sitting on the compliant sample without any external perturbation, *i.e.*, constant stress. Krishnan *et al.*[24] studied the effect of time on the adhesion of polystyrene particles to silicon substrates under zero external loads, and found the contact area had a logarithmical dependence on time. The long relaxation time (~6 days) was attributed to the slow plastic deformation of polystyrene particles. The contact radius at the zero-deflection point can be obtained through Equations (4-1) and (4-2). Figure 4-5b shows the contact area has an asymptotic dependence on time. However, a single logarithmical function fails to fit.

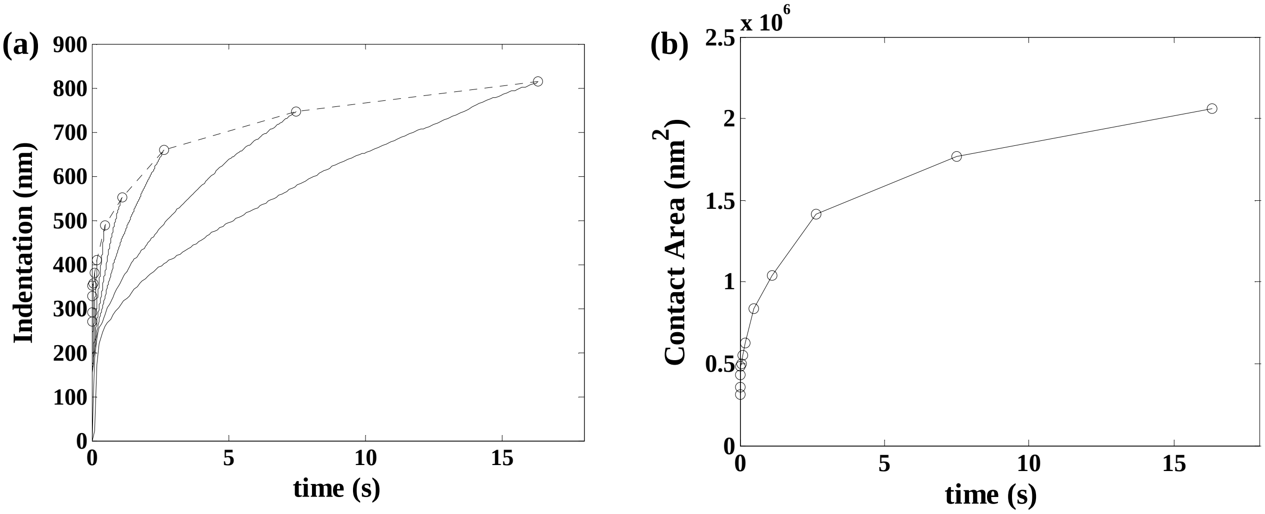

Figure 4-5. (a) The indentation vs. time curves (solid lines) for each ramp rate from the contact point to the zero cantilever deflection point for the force curves in Figure 4-2a. The ramp rate increases from left to right. Open circles at the end of each solid line correspond to the adhesion-induced indentation for each ramp rate. (b) The contact area at the zero-deflection point, corresponding to the open circles in (a) has an asymptotic dependence on time.

A viscoelastic material shows a dynamic modulus under an external perturbation. It presents effectively hard initially and softens over time. The two elastic limits are E_0 for the instantaneous modulus at the start of the external perturbation and E_∞ for the relaxed modulus (infinite time). For cross-linked polymers, the modulus relaxation is usually described by constitutive models for linear viscoelasticity, in which springs and dashpots are combined in series or parallel, and multiple characteristic times can exist in one material. For instance, an extended Zener model[25] is given in Figure 4-6, in which

$$E_r(t) = E_\infty + \sum_{i=1}^{n} E_i \exp(-\frac{E_i}{\eta_i} t) \tag{4-3}$$

where $E_r(t)$ is the relaxed modulus at time t, E_∞ is the relaxed modulus over a long time, and E_i and η_i are the modulus and viscosity of the ith viscoelastic component, respectively. η_i/E_i is the characteristic time of the ith viscoelastic component.

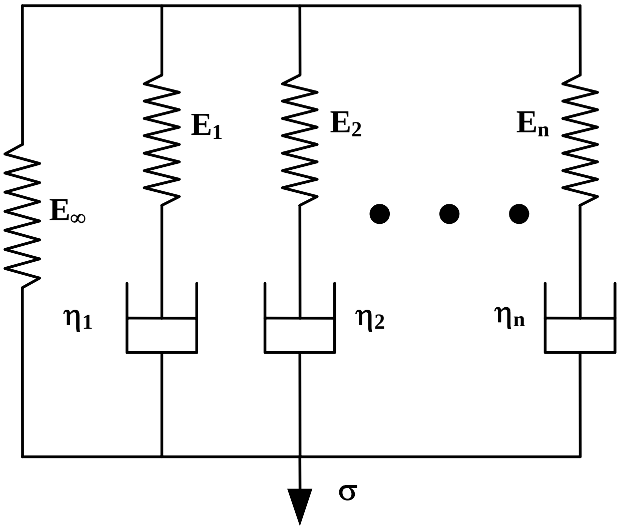

Figure 4-6. Extended Zener's model. E_∞ is the relaxed modulus, E_i and η_i are the modulus and viscosity of the ith viscoelastic component, and σ is the stress.

The characterization of the general constitutive equations usually requires either constant stress for creep or constant strain for stress relaxation. However, along the extension force curves in Figure 4-4a, the stress and strain both vary continuously and nonlinearly, which results in nonlinear creep and relaxation. The kernel functions thus obtained are complicated. The hyperboloidal shape of the AFM tip complicates the situation even further. Fortunately, analysis of the extension force curve at a single ramp rate is not the only way to characterize the relaxation properties of the sample. Alternatively, the viscoelasticity of the sample can be studied using the zero-deflection points at different ramp rates, i.e., the dashed line in Figure 4-5a, where a constant stress is applied. At the beginning of the process along the dashed line, an instantaneous stress is applied to the sample via the impact of a particle on the sample surface. Then the sample goes under an adhesion-induced viscoelastic creep, which results in deeper indentation of the particle. The strain of the sample should follow an asymptotic increase with the time, similar to the dashed line in Figure 4-5a. The creep compliance *Dc(t)* at a fixed stress for the extended Zener's model can be written as

$$D_c(t) = \frac{1}{E_r(t)} = \frac{1}{E_\infty} - \sum_{i=1}^{n} \frac{E_i}{(E_i + E_\infty)E_\infty} \exp(-\frac{E_i E_\infty}{\eta_i (E_i + E_\infty)} t) \qquad (4\text{-}4)$$

where the parameters stand for the same variables as in Equation (4-3).

The relaxed elastic moduli at the adhesion-induced indentation points can be solved from Equations (4-1) and (4-2) with the knowledge of Dupré's work of adhesion w_0, which was estimated to be about 58 mJ/m^2 for the SiO_2 (the outer layer of the plasma cleaned Si_3N_4 tip) and PDMS interface[26]. During the crack healing process when the AFM tip is pulled into the PDMS sample, the effective work of adhesion can be considered constant, as shown in many studies[12,16,17,21]. Figure 4-7 shows the time dependence of the reciprocal of the relaxed elastic moduli at the corresponding adhesion-induced indentation points in Figure 4-5a. A tri-exponential decay function as Equation (4) fits the data in Figure 4-7, and gives $E_\infty = 0.367$ MPa and three characteristic times of 7.57 ms, 0.73 s, and 7.26 s. Similarly, the time dependence of the creep compliance for samples 253DP, 120DP, 60DP, and 37DP is analyzed. It is found that for 253DP and 120DP, the $1/E_r$ vs. t curves are best fitted using bi-exponential decay function, while for 60 DP and 37DP, a single exponential decay function fits well. The fitting results are given in Table 4-1. Values of each viscous and elastic component are also converted based on Equation 4-4 and listed in Table 4-1. It is worthwhile to point out that for the harder and more elastic samples 60DP and 37DP, the change of adhesion-induced indentation is noticeable only for fast ramp rates. That causes the single exponential fit, which includes the data of slow ramp rates, to be questionable. It is clear that the monotonic dependence of the adhesion-induced indentation and the corresponding contact radius dependence on the ramp rate is caused by the viscoelastic relaxation in the bulk material.

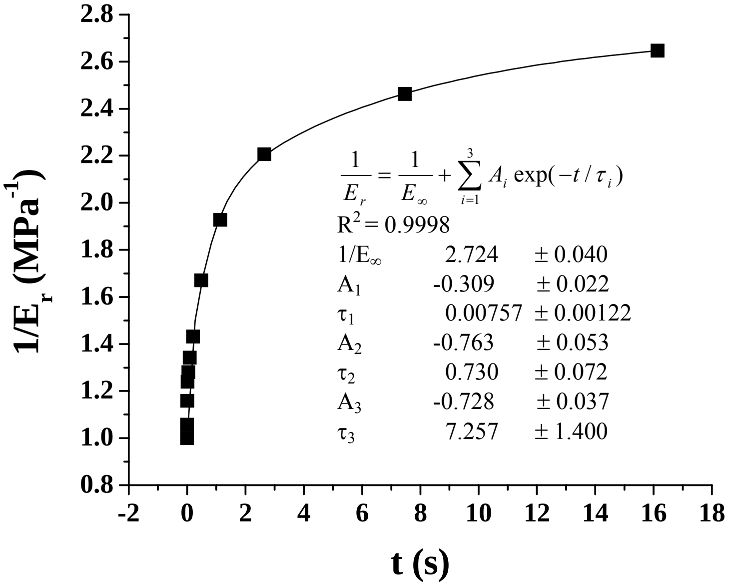

Figure 4-7. The time dependence of the reciprocal of the relaxed elastic moduli at the corresponding adhesion-induced indentation points in Figure 4-3a. A tri-exponential decay function (Equation (4-4)) fits the data.

Table 4-1. Fitting results for different PDMS samples based on Equation (4-4)

	E_∞ (MPa)	A_1	τ_1 (s)	E_1 (MPa)	η_1 (MPa/s)	A_2	τ_2 (s)	E_2 (MPa)	η_2 (MPa/s)	A_3	τ_3 (s)	E_3 (MPa)	η_3 (MPa/s)
705DP	0.36	0.31	7.57 E-3	0.047	3.15 E-4	0.76	0.73	0.14	0.075	0.73	7.26	0.13	0.71
253DP	0.81	0.19	0.016	0.15	2.02 E-3	0.080	2.44	0.057	0.13				
120DP	0.97	0.17	0.029	0.19	4.71 E-3	0.035	1.63	0.034	0.053				
60DP	2.07	0.053	0.12	0.25	0.027								
37DP	3.96	0.027	0.15	0.48	0.065								

When bulk polymer is stressed, the mechanical energy at the boundary is transmitted through the chain molecules primarily along the chain[27]. The local segmental motion of a polymer chain is fast, on a time scale of nanoseconds. In real polymer systems well above Tg, however, a conformer in a chain can interact with other conformers on the same chain or conformers on other chains. These interactions cause so called intramolecular cooperativity and intermolecular cooperativity in the polymer relaxation. These cooperative motions of polymer chains are much slower, on a time scale of milliseconds. In Table 4-1, one can see that denser cross-linked PDMS samples 37DP and 60DP have one characteristic time, intermediate cross-linked PDMS samples 120DP and 253DP have two characteristic times, while highly loose cross-linked PDMS sample 705DP has three characteristic times. It is obvious that the cross-link density determines the relaxation pathways of polymer chains in these samples. In a cross-linked polymer network, the cross-linking remarkably lowers the mobility of the segments close to the cross-linking points. τ_1 in Table 4-1 describes the motion of cooperative cross-links in the network. The cross-links in the lowest cross-linked 705DP polymer have the largest freedom of motion and present a short relaxation time. Accordingly, denser cross-linked polymers have long relaxation times for the cross-linker motion. For 37DP and 60DP, the network chain length is so small that motion of the segments away from the cross-linking points can be coupled with segmental motions around the cross-linkers, and results in a single relaxation time, given the resolution of our experiments. For polymers 120DP, 253DP, and 705DP, polymer chains between cross-links are free from topological constrains of the chemical cross-linking, but bear intramolecular segmental cooperativity in their motion. τ_2 in Table 4-1, about 1 second, are assigned to this motion. Physical entanglements may contribute to the viscoelasticity of a sample significantly. For linear PDMS, the critical molecular weight Mc between cross-linking is about 30 kg/mol[28,29]. When the molecular weight of PDMS is larger than the critical molecular weight M_c, physical entanglements between polymer strands are present extensively in the network. In our experiment, 705DP PDMS has a weight average molecular weight M_w = 52 kg/mol (M_w of 253DP PDMS is 18.7 kg/mol). Therefore, 705DP PDMS is a physical entanglement dominated network. The relaxation of the physical entanglements under stress takes longer time than other relaxation pathways. τ_3 in Table 4-1 is assigned to this motion. The coefficient A_3 shows that the physical entanglements have a large contribution to the unrelaxed modulus of 705DP PDMS. There have been other studies of the relaxation properties of end-linked PDMS networks. Gillies *et al.*[23,30]. used AFM to study cross-linked PDMS and found $E_\infty = 0.8$ MPa (comparable to our 253DP sample) and a characteristic time of 120 ms. Geniesser *et al.*[31] observed similar results using a lateral force rheometer. These characteristic times are all in the range that is comparable with our results, which indicates that AFM can be a powerful tool to study viscoelastic properties of cross-linked polymers. We note that we identified multiple relaxation times within most samples, whereas the above studies identified at most one relaxation time.

4.3.2. Studies and discussions of the retraction force curves

As mentioned previously, the retraction force curves during the unloading process showed a turning point of the adherence with the ramp rates as shown in Figure 4-4b. We find that the turning point is caused by a combined effect of the ramp rates and the contact radii at adhesion-induced indentation point. Many studies have shown that the effective work of adhesion during separating two surfaces is a function of the crack propagation rate, *da/dt*[12,16,17,21,32,33]. *a* is the contact radius. Maugis and Barquins[33] suggested using the strain energy release rate *G* to describe the effective work to extends the crack by a unit area. The sign of the quantity ($G-w_0$) determines if the crack extends or recedes spontaneously. The rate dependence of *G* may originate from several different effects that cause irreversible energy dissipation as discussed in the introduction. Gent and Schultz[34] and Andrews and Kinlock[35] found that the rate dependent strain energy release rate G can be written as

$$G(v) = w_0(1 + \varphi(a_T v)) \tag{4-5}$$

where w_0 is the Dupre's work of adhesion, $\varphi (a_T v)$ is a characteristic of the viscoelastic material, a_T is the shift factor in the Williams-Landel-Ferry transformation[29], and $v = da/dt$ is the crack propagation rate. Several peeling tests of elastomeric materials from a rigid surface showed that $\varphi (a_T v)$ has a power law dependence on v, as:

$$\varphi(a_T v) = \alpha(T) v^n \tag{4-6}$$

where $\alpha(T) = a_T^n$, and n is usually found to be 0.6.

During the AFM tip retracts from the PDMS sample, the change of piezocrystal retraction distance ΔZ is sum of the change of the cantilever deflection Δd and the change of sample deformation $\Delta\delta$, *i.e.*,

$$-\Delta Z = \Delta d + \Delta\delta \tag{4-7}$$

At the adherence point, *i.e.*, the maximum negative deflection point, $\Delta d_{adhr} = 0$, so $-\Delta Z_{adhr} = \Delta\delta_{adhr}$.

The decrease of the stored elastic energy at the adherence point is $-P\Delta\delta_{adhr}$, where $P = k_{tip} \bullet d_{adhr}$ is loading force on the cantilever at the adherence point. k_{tip} is the force constant of the cantilever, and d_{adhr} is the cantilever deflection at the adherence point. The change of the work of adhesion is $2\pi a_{adhr} \cdot \Delta a_{adhr} \cdot G_{adhr}$, where G_{adhr} is used instead of w_0 to include the dissipated energy, a_{adhr} is the contact radius at the adherence point, and Δa_{adhr} is the change of contact radius at the adherence point. The increased surface energy and dissipated energy balances the decrease of the elastic energy as

$$P \cdot \Delta\delta_{\mathrm{adhr}} = 2\pi a_{\mathrm{adhr}} \cdot \Delta a_{\mathrm{adhr}} \cdot G_{\mathrm{adhr}} \tag{4-8}$$

and then

$$\frac{d_{adhr}}{a_{adhr}} = \frac{2\pi}{k_{tip}} \cdot \frac{\Delta a_{adhr}}{\Delta\delta_{adhr}} \cdot G \tag{4-9}$$

Assuming G has a power law dependence of the crack propagation rate as in Equation (4-6), we have

$$G = w_0(1+\alpha(T)\cdot(da/dt)^{\mathrm{n}}) \tag{4-10}$$

Note during the retraction of the AFM tip from the sample, the crack propagation rate da/dt is not a constant as in the case of an elastomeric pad peeled from a flat rigid surface. Instead, the ramp rate $V = dZ/dt$ is a constant. Equation (4-10) becomes

$$G = w_0(1+\alpha(T)\cdot(da/dZ)^{\mathrm{n}}\cdot V^{\mathrm{n}}) \tag{4-11}$$

and Equation (4-9) becomes

$$\frac{d_{adhr}}{a_{adhr}} = \frac{2\pi}{k_{tip}}\cdot\frac{\Delta a_{adhr}}{\Delta\delta_{adhr}}\cdot w_0(1+\alpha(T)\cdot\left(\frac{\Delta a_{adhr}}{\Delta\delta_{adhr}}\right)^{\mathrm{n}}\cdot V^{\mathrm{n}}) \tag{4-12}$$

Considering the geometry of the AFM tip, $\Delta a_{adhr}/\Delta\delta_{adhr}\approx \tan(\alpha)=0.7$, where $\alpha = 35°$ is the semi-vertical angle of the AFM tip. Taking $w_0 = 58\ mJ/m^2$, and $k_{tip} = 0.36\ N/m$, Equation (4-12) becomes

$$\frac{d_{adhr}}{a_{adhr}} \approx 0.71\cdot(1+\alpha(T)\cdot 0.71^{\mathrm{n}}\cdot V^{\mathrm{n}}) \tag{4-13}$$

Equation (4-13) shows that the adherence force of the AFM tip is a function of both the ramp rate V and the contact radius a_{adhr}. The normalized adherence (d_{adhr}/a_{adhr}) has a power law dependence on the ramp speed. Equations (4-1) and (4-2) can be used to describe the adherence point when replacing w_0 with G and E with $E_r(t)$, which is described as in Equation (4-4). The contact radii are solved for the adherence points at different ramp rates in Figure 4-4b. Figure 4-8a shows how the adherence d_{adhr} varies with the ramp speed. A turning point occurs obviously at 4000nm/s, *i.e.*, at the ramp rate 0.8 Hz. Figure 4-8b shows the dependence of the normalized adherence (d_{adhr}/a_{adhr}) on ramp speeds. A power law function as given in Equation (4-13) fits the data, and gives the coefficient 0.68 which is close to the predicted value 0.71 in Equation (4-13). The fit gives the power, n=0.26.

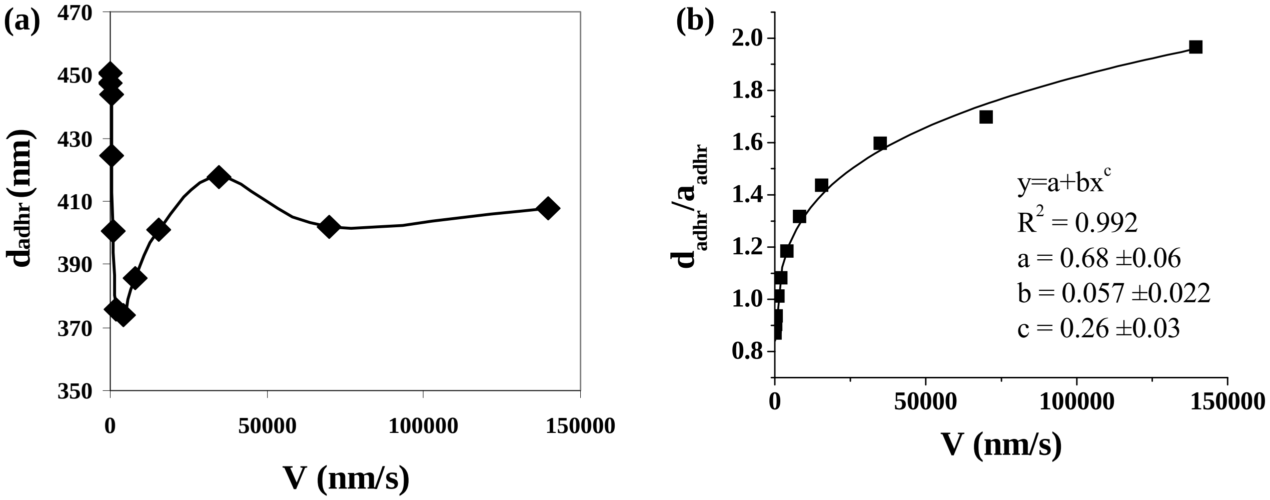

Figure 4-8. (a) The adherence dadhr varies with the ramp speed and shows a turning point around 4000nm/s, i.e., at the ramp rate 0.8 Hz. (b) the normalized adherence (d_{adhr} /a_{adhr}) shows a monotonic dependence on ramp speeds. A power law function as given in Equation (4-13) fits the data.

In Chapter 4.3.1, it is found that the contact radius at the adhesion-induced indentation point is determined by the viscoelastic relaxation of the bulk material. During the retraction force curve, energy dissipation occurs both in the bulk and at the interface. The contact radius at the adherence point is thus determined by the ramp rate dependent processes in both the bulk and the interface. Figure 4-9 shows a power law dependence on the ramp rate dependence for the contact radius at the adherence point of 705DP PDMS. Nonetheless, the logarithmic plot shows a tilted seagull shape, and interestingly, the transition point is at 0.8 Hz, which corresponds to the turning point of the rate dependent adherence force.

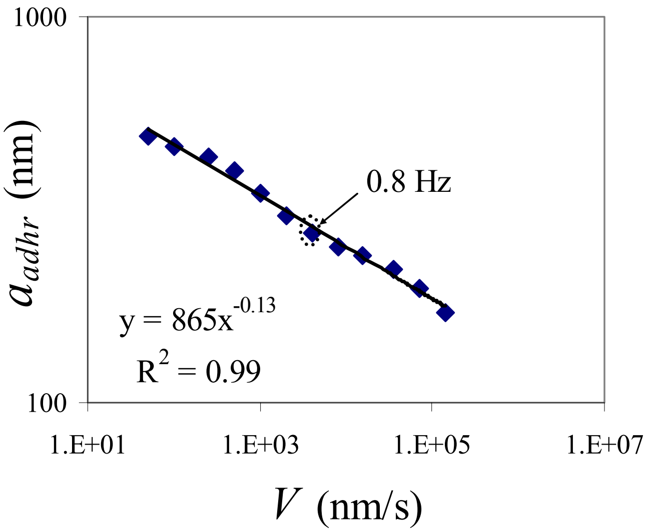

Figure 4-9. The contact radii at the adherence point vary with the ramp speeds.

When the power law fit in Figure 7 is used, Equation (13) becomes

$$d_{adhr} \approx A \cdot (1 + B \cdot V^{\mathrm{n}}) \cdot V^{-m} \qquad \text{(4-14)}$$

where the coefficients in Equation (4-13) are replaced by parameters *A* and *B*. Obviously, Equation (4-14) gives a turning point of d_{adhr} as a function of *V*. In summary, the adherence d_{adhr} is determined by viscoelastic processes both in the bulk and at the interface.

4.3.3. Other evidence for the viscoelastic response of PDMS under adhesive interaction with AFM tips.

AFM tips were held in contact with the PDMS samples for different dwell times to study the viscous relaxation. Figure 4-10 gives the typical force plots of 705DP PDMS under different dwell times at a constant ramp rate of 0.1 Hz. When there is no delay, the retraction force curve starts where the extension curve ends. When the tip is held in contact with the PDMS, the retraction force curve starts at a more negative force. A longer dwell time causes a larger gap between the end of the extension curve and the beginning of the retraction curve as seen in

Figure 4-10. It is believed that the negative shift of the cantilever deflection during the dwell time is caused by the sample relaxation[20]. This observation is consistent with the results and discussions in Chapter 4.3.1. 253DP PDMS showed a similar dependence on the dwelling time, while other harder PDMS samples did not have obvious effects of the dwell time. A longer dwell time also causes a larger adherence in the retraction force curve as shown in Figure 4-10. This is obvious based on the discussion in Chapter 4.3.2, where the adherence is found to be a function of both the ramp rate and the contact radius. At a longer dwell time, the AFM tip is pulled into the DPMS sample deeper, *i.e.*, a larger contact radius. The cut-off region at the bottom of the retraction curve of 20 s case occurred because the deflection was over the detection limit of the detector.

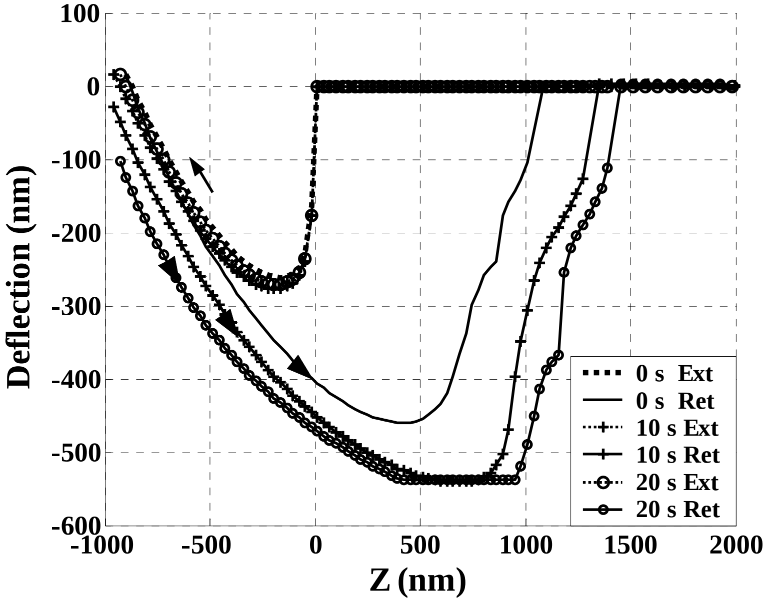

Figure 4-10. Typical force plots of 705DP PDMS under different dwell times at a constant ramp rate of 0.1 Hz.

Several studies have found that when a PDMS sample interacts with a hydrophilic surface, polymer chains at the interface can re-organize to form strong dipolar interaction, such as H-bonds, with the surface, and in turn cause a large hysteresis[12,13,15-17,19]. To investigate the main source of the hysteresis in our experiment, methyl and hydroxyl functionalized AFM tips, which are named “CH3” and “OH” tips respectively hereafter, were used to collect force plots on PDMS samples. The tip radii and force constants (k_{CH3}/k_{OH} = 0.94) of the two functionalized tips were similar as measured. The quality of the two tips was checked by measuring their adhesion at a same rate on the surface of freshly cleaved mica. The results are given in Figure 4-11a, where one can see that on the hydrophilic mica surface, the OH tip has an adhesion about two times that of the CH3 tip. Figure 4-11b shows the force plots for the two tips on the 253DP PDMS sample at two extreme ramp rates of 27.9 Hz and 0.02 Hz.

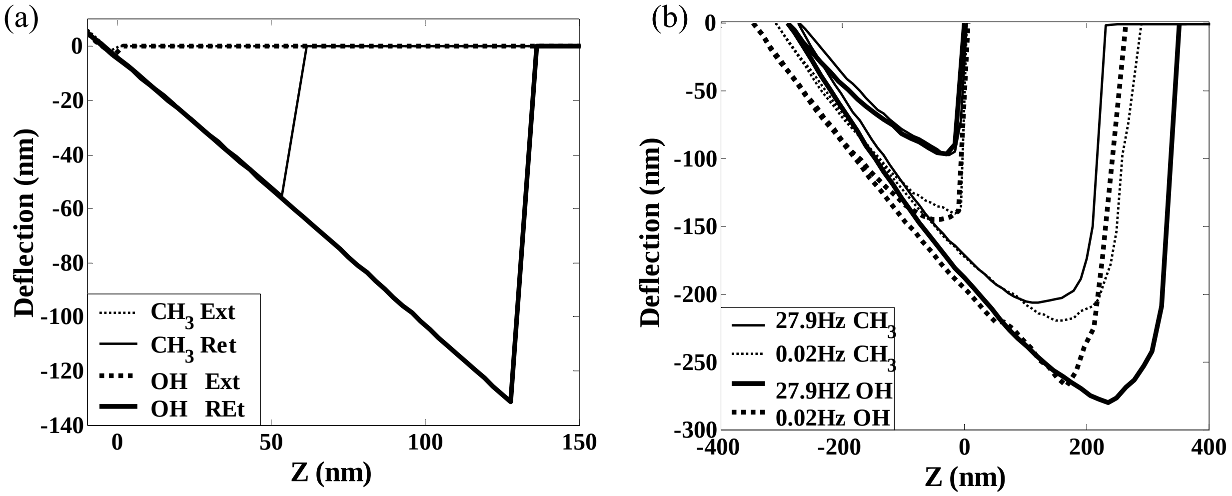

Figure 4-11. (a) Force plots of CH3 tip and OH tip at a same z-motion rate on a piece of freshly cleaved mica surface. (b) Force plots for CH3 tip and OH tip on the 253DP PDMS sample at two extreme ramp rates of 27.9 Hz and 0.02 Hz.

For both tips, the adhesion-induced indentation at 0.02 Hz is larger than that at 27.9 Hz as expected. At the same ramp rate, the OH tip has larger adhesion-induced indentation and adherence than the CH3 tip does. This indicates the existence of hydrogen-bond effects. For the CH3 tip, the adherence at 0.02 Hz is larger than that at 27.9 Hz, while for the OH tip, the situation is opposite. Based on Equation (4-14), one can conclude that for the CH3 tip, the energy dissipation is dominated by bulk relaxation, while for the OH tip, it is dominated by interfacial relaxation. This is additional evidence that stronger bonds formed at the interface of the PDMS and the OH tip.

de Gennes[36] has suggested that for a rubber-solid interface, if the energy dissipation is mostly through the stretch and detachment of the chains in the vicinity of the crack tip, the strain energy release rate, *G*, should be always larger than Dupre's work of adhesion w_0. An extrapolation to the zero crack propagation rate gives $G \approx w_0 N_0^{1/2}$, where N_0 is the number of monomers between cross-links. Choi *et al.*[15] studied the adhesion of cross-linked PDMS to silicon oxide surfaces using the JKR method, and found *G* and w_0 were well correlated by the de Gennes model. Using the whole-curve fitting method proposed in Chapter 3, the averaged *G* along the retraction curves were obtained for the PDMS samples. To prevent possible uniqueness of the force plot at a single random sample point, force volume data were collected for each sample with a scan size of 10x10 μm^2. Note that *G* depends on the crack propagation rate *da/dt* and increases continuously along the retraction force curve, so the obtained *G* are averaged values. Figure 4-12 shows the results at ramp rates between 0.1 Hz and 3.2 Hz. One can see that *G* is linearly proportional to $N_0^{1/2}$ in the tested ramp rate range. Figure 4-12 also shows that *G* of less cross-linked PDMS sample is more sensitive to the change of ramp rates, which implies slower relaxation process undergoing at the surface of the less cross-linked PDMS.

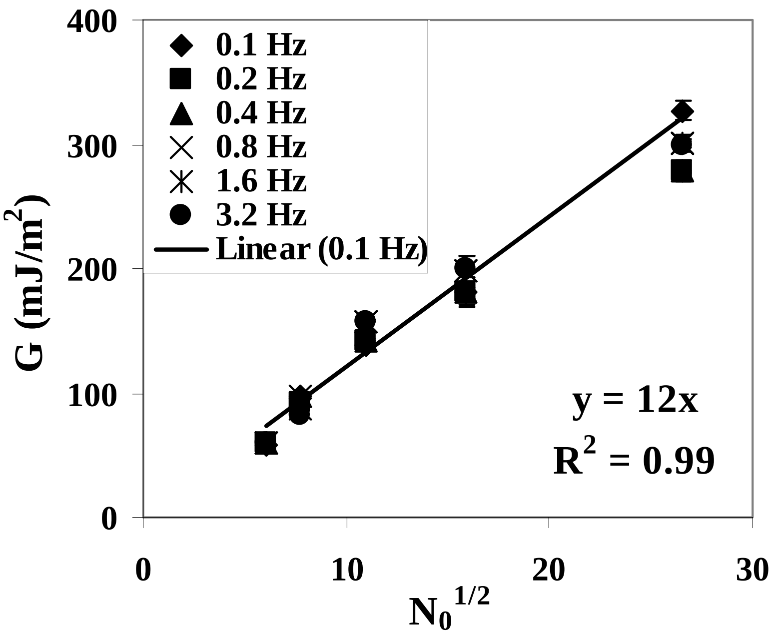

Figure 4-12. The averaged strain energy release rate G at an intermediate ramp rate is linearly proportional to N01/2. N0 is the number of monomers between cross-links.

4.4. Conclusion

The viscoelastic response of cross-linked poly-(dimethylsiloxane) (PDMS) in the adhesive interaction with AFM tips has been studied as a follow-up of our previous study of simple elasticity. It is found that in the extension force curve, the adhesion-induced indentation is dependent on the ramp speed monotonically, while for the retraction force curve, the adherence force has a turning point as a function of ramp speeds. Analysis of the extension force curves reveals viscoelastic relaxation processes in the bulk polymer, which causes a monotonic rate dependence of the adhesion-induced indentation. The viscoelastic relaxation processes in the bulk polymer have different components based on the molecular weight between cross-links. Analysis of the retraction force curves shows that besides the viscoelastic processes in the bulk, relaxation processes also occur at the tip-polymer interface. The competition between the bulk relaxation and the interfacial relaxation results in the turning point of the adherence force as a function of the ramp speed. Results of the dwell time tests and the functionalized AFM tips provide support for the conclusions. The energy dissipation processes can be quantified by using the described interpretation of force plots for AFM tip-sample viscoelastic interaction. The study has shown that AFM is a powerful tool to study the damping mechanics of polymer surfaces at nanometer scales.

BIBLIOGRAPHY

1. Domkea, J.;Dannohla, S.;Paraka, W. J.;Muller, O.;Aicher, W. K.;Radmacher, M. *Colloids Surf., B: Biointerfaces* **2000**, *19*, 367-379.
2. Moy, V. T.;Jiao, Y.;Hillmann, T.;Lehmann, H.;Sano, T. *Biophys. J.* **1999**, *76*, 1632-1638.
3. Tabor, D. *J. Colloid Interface Sci.* **1977**, *58*, 2-13.
4. James, H. M.;Guth, E. *J. Chem. Phys.* **1947**, *15*, 669-683.
5. James, H. M.;Guth, E. *J. Chem. Phys.* **1943**, *11*, 455-481.
6. Wall, F. T. *J. Chem. Phys.* **1943**, *11*, 527-530.
7. Flory, P. J. *J. Chem. Phys.* **1977**, *66*, 5720-5729.
8. Ronca, G.;Allegra, G. *J. Chem. Phys.* **1975**, *63*, 4990-4997.
9. De Gennes, P. G. *J. Chem. Phys.* **1971**, *55*, 572-579.
10. Doi, M.;Edwards, S. F. *J. Chem. Soc., Faraday Trans. 2* **1978**, *74*, 1789-1801.
11. Rouse, P. E. J. *J. Chem. Phys.* **1953**, *21*, 1272-1280.
12. Silberzan, P.;Perutz, S.;Kramer, E. J.;Chaudhury, M. K. *Langmuir* **1994**, *10*, 2466-2470.

13. Choi, G. Y.;Kang, J. F.;Ulman, A.;Zurawsky, W. *Langmuir* **1999**, *15*, 8783-8786.

14. Choi, G. Y.;Kim, S.;Ulman, A. *Langmuir* **1997**, *13*, 6333-6338.

15. Choi, G. Y.;Zurawsky, W.;Ulman, A. *Langmuir* **1999**, *15*, 8447-8450.

16. Kim, S.;Choi, G. Y.;Ulman, A.;Fleischer, C. *Langmuir* **1997**, *13*, 6850-6856.

17. Mason, R.;Emerson, J.;Koberstein, J. T. *J. Adhes.* **2004**, *80*, 119-143.

18. Perutz, S.;Kramer, E. J.;Baney, J.;Hui, C. Y.;Cohen, C. *J. Polym. Sci., Part B: Polym. Phys.* **1998**, *36*, 2129-2139.

19. Perutz, S.;Kramer, E. J.;Baney, J.;Hui, C. Y. *Macromolecules* **1997**, *30*, 7964-7969.

20. Pickering, J. P.;Vancso, G. J. *Macromol. Symp.* **2001**, *166*, 189-199.

21. Vakarelski, I. U.;Toritani, A.;Nakayama, M.;Hisashitani, K. *Langmuir* **2001**, *17*, 4739-4745.

22. Noel, O.;Brogly, M.;Castelein, G.;Schultz, J. *Eur. Polym. J.* **2004**, *40*, 965-974.

23. Gillies, G.;Prestidge, C. A.;Attard, P. *Langmuir* **2002**, *18*, 1674-1679.

24. Krishnan, S.;Busnaina, A. A.;Rimai, D. S.;Demejo, L. P. *J. Adhesion Sci. Technol.* **1994**, *8*, 1357-1370.

25. Ward, I. M., *Mechanical Properties of Solid Polymers*. 2nd ed. **1983**, Chichester: Wiley.

26. Sun, Y.;Akhremitchev, B.;Walker, G. C. *Langmuir* **2004**, *20*, 5837-5845.

27. Matsuoka, S., *Relaxation phenomena in polymers*. **1992**, Oxford, U.K.: Oxford University Press.

28. Doi, M., *Introduction to Polymer Physics*. **1996**, Oxford, U.K.: Oxford University Press.

29. Ferry, P., *Viscoelastic properties of polymers*. **1980**, New York: John Wiley & Sons.

30. Gillies, G.;Prestidge, C. A. *Adv. Coll. Inter. Sci.* **2004**, *108-109*, 197-205.

31. Genieser, L. H.;Hendriks, K. C. P.;Baaijens, F. T. P.;Meijer, H. E. H. *J. Rheol.* **2000**, *44*, 1003-1017.

32. Barquins, M. *J. Adhes.* **1981**, *14*, 63-82.

33. Maugis, D.;Barquins, M. *J. Phys. D: Appl. Phys.* **1978**, *11*, 1989-2023.

34. Gent, A. N.;Schultz, J. *J. Adhes.* **1972**, *3*, 281-294.

35. Andrews, E. H.;Kinloch, A. J. *Proc. R. Soc. A* **1973**, *332*, 385-399.

36. De Gennes, P. G. *C. R. Acad. Sci. Paris* **1995**, *320*, 193-197.

Chapter 5. Surface Elastic Modulus of Barnacle Adhesive and Release Characteristics from Silicone Surfaces

Abstract

The properties of barnacle adhesive on silicone surfaces were studied by AFM indentation, imaging, and other tests and compared to the barnacle shear adhesion strength. A multilayered structure of barnacle adhesive plaque is proposed based on layered modulus regions measured by AFM indentation. The fracture of barnacles from PDMS surfaces was found to include both interfacial and cohesive failure of barnacle adhesive plaque, as determined by protein staining of the substrate after forced barnacle release from the substrate. Data for freshly released barnacles showed that there was a strong correlation between the mean Young's modulus of the outermost (softest) adhesive layer ($E<0.3$ MPa) and the shear strength of adhesion, but no correlation for other higher modulus regions. Linear, quadratic, and Griffth's failure criterion (based on rough estimate of crack length) regressions were used in the fit, and showed significance.

5.1. Introduction

Biofouling is the undesired accumulation of micro-organisms, plants or animals on artificial surfaces. Fouling on hulls can increase hydrodynamic drag on vessels, which in turn increases fuel cost by millions of dollars annually and reduces their speed and range[1]. Traditionally, fouling has been controlled by the use of antifouling paints containing poisons, however, environmental impacts of excessive biocide input into the environment have resulted in regulations restricting or banning the use of many compounds, and there is interest in developing biocide free methods of control. Silicone fouling release coatings are a promising, biocide free technology, which have received considerable interest for biofouling control in recent years[2-13].

The mechanism of fouling release from silicone surfaces is still not completely understood, however it is generally believed that their anti-biofouling properties are due to their low surface energies[14,15], low glass transition temperature[4], and low modulus[8]. The forced release of barnacles may be considered a fracture process. The defects or voids between the contacts produce stress concentrations where the cracks initiate and propagate. At the moment when the effective stress $\widetilde{\sigma}$ reaches the critical failure stress σ_c, the failure is expected to happen. When a crack propagates under a thermodynamic equilibrium, the work of the external force W_d and the loss of the elastic energy U stored in the bulk of the specimen equal the gain of the surface free energy. Based on this, Griffith derived his fracture theory[16,17] for an elastic material containing a sharp crack for plane stress as shown in Equation (5-1).

$$\sigma_c = \sqrt{\frac{2EG_c}{\pi a}} \tag{5-1}$$

Here σ_c is the critical crack stress, G_c is the critical fracture energy, E is the elastic modulus, and a is half the crack length. Based on Griffith fracture criterion, Kendall[18] derived how the critical crack stress depends on the thickness of a thin elastic film when a rigid stud is peeled off from it by a force normal to the surface. The expression is given in Equation (5-2)

$$\sigma_c = \sqrt{\frac{2I_c K}{t}} \tag{5-2}$$

where I_c is the interfacial fracture energy, K is the coating bulk modulus, and t is the coating thickness. The interfacial fracture energy I_c is defined as the energy required to separate the unit area of the contacting surfaces in the absence of energy losses. For joints that exhibit a solely interfacial locus of failure, and show no energy dissipation during the crack growth, e.g., the crack growth rate is slow and adhesion is reversible, and in which only secondary bonding is established, then $I_c = W_a$, where W_a is the work of adhesion.

Equations (5-1) and (5-2) indicate an importance of elastic modulus to fracture. There have been several studies using pseudobarnacles[19-21] to investigate the relationship between coating modulus and detachment. However, it must be remembered that the modulus of barnacle adhesive differs from these artificial adhesives, and the barnacle adhesive modulus may be important for bioadhesive efficiency. Several papers have presented observations relating the condition of the barnacle adhesive to the substrate on which they are settled[6,22-25] . In this study, we investigated barnacles that grew on three different types of substrata, and used the atomic force microscopy indentation technique to study the surface elastic moduli of barnacle adhesive plaque. Correlations were found between the shear strength of adhesion and the mean barnacle adhesive elastic modulus. Adhesion failure models that interpret the correlation are discussed.

5.2. Materials and Methods

Two different types of silicone (PDMS, DC 3140 and T2 Silastic) of different thickness (600, 200, 50 μm) with and without DC550 silicone fluid (hereafter referred to as “oil”) were applied to glass panels and exposed to fouling at the Florida Institute of Technology (FIT) static immersion site. Barnacle adhesion measurements were collected using ASTM D5618-94 procedures, and the properties of the barnacle adhesive were investigated using AFM and optical light microscopic techniques.

Data were collected on two types of barnacles, *Balanus eburneus* (Be) and *Balanus variagatus* (Bv). The first set of barnacles in this study was selected to represent three groups from panels: maximum, mean, and minimum adhesion values, which were measured at FIT and transported in wet tissue paper to University of Pittsburgh by overnight mail. The information of the first and second sets of barnacles is given in Table 5-1 and Table 5-2, respectively. The second set of barnacles were transported with the panels in coolers of seawater to the University of Pittsburgh and the barnacle adhesion measurements made just prior to examination of the barnacle to minimize changes that may occur due to prolonged exposure to air. This set included 7 Be and 1 Bv barnacles on 600 μm thick T2 Silastic coatings without oil.

Table 5-1. The information of the first set of barnacles studied in AFM experiments.

Box #	Barnacle #	Type	Coating	Thickness (μm)	Addition
10	1 2 3	Be	DC 3140	600	none
10	4 5 7 8	Be	DC 3140	200	"oil"
10	6	Bv	DC 3140	200	"oil"
10	9 10 11	Be	DC 3140	50	"oil"
18	1	Be OG	DC 3140	600	none
18	2 3	Be	DC 3140	600	none
18	4 5 6	Be	DC 3140	200	"oil"
18	7 8 9	Be	DC 3140	50	"oil"
18	10	Bv	DC 3140	50	"oil"
18	11 12 13	Be Def	DC 3140	50	"oil"
403	1 2 3 4 5 6	Be	DC 3140	50	none
403	7 8 9 10 11 12	Be	T2 Silastic	50	none
404	1 2 3 4 5 6	Be	DC 3140	50	none
404	7 8 9 10 11 12	Be	T2 Silastic	50	none

Table 5-2. The information of the second set of barnacles studied in AFM experiments.

Barnacle #	Type	Coating	Thickness (μm)	Addition
1	Be	T2 Silastic	600	none
2	Be	T2 Silastic	600	none
3	Be	T2 Silastic	600	none
4	Be	T2 Silastic	600	none
5	Be	T2 Silastic	600	none
6	Be	T2 Silastic	600	none
7	Be	T2 Silastic	600	none
8	Bv	T2 Silastic	600	none

Atomic force microscopy (Digital Instruments Dimension 3100, Santa Barbara, CA) was used to image the barnacle adhesive plaque and quantify surface modulus. Tapping mode cantilevers (Mikromash, NSC-15, Tallinn, Estonia) were used for the tapping mode imaging of the barnacle adhesive plaque. Contact mode cantilevers (Digital Instrument NP-SW, Santa Barbara, CA) were used for the indentation experiment. The force constant of the contact mode cantilever was 0.66 N/m as measured by the add-mass method[26]. All indentation experiments were done in artificial sea water. In addition to the imaging and indentation measurement using AFM, the percentage of soft area of barnacle adhesive plaque were estimated by visual inspection and probing the surface with a hard sharp needle to distinguish distinct areas as soft or hard. Because it has been reported that barnacles that grow on PDMS may exhibit cup-shape bases filled with white and soft glue[11,23,27], we also measured the maximum center depth (1/curvature of baseplate). To characterize the surface energy, contact angles were measured on each barnacle adhesive plaque.

Seawater preparation: Seawater was prepared from the instant seawater recipe of Aquarium Systems (Mentor, Ohio). Following instruction on the package, 0.5 Cup of Instant Ocean salt was added in each U.S. Gallon of water and the solution was stirred vigorously overnight to balance the CO_2 level.

Optical light microscopy and stain experiment: An inverted light microscope (Olympus IX71, Melville, NY) was used to study the barnacle adhesive plaque and the films left behind by barnacles on the PDMS panel. Red dye Eosin Y was used to stain the adhesive plaque and films on the panel.

Preparation of barnacles for AFM imaging and indentation experiments: Barnacles were put upside down into wet fine sand, and the adhesive plaques were aligned horizontally by eye.

This treatment can keep barnacles alive during the experiments. All barnacles removed at FIT were put in the synthetic seawater upon arrival in Pittsburgh 24 hours after release and kept in a refrigerator. All freshly removed barnacles were studied by AFM within an hour after detachment. Before each experiment, barnacle adhesive plaques were cleaned by splashing them with deionized water and dried by wicking the water using paper tissues.

AFM imaging of barnacle adhesive plaques: Tapping mode AFM was employed to image barnacle adhesive plaque in air. To avoid the dehydration problem, imaging was performed within a few minutes after barnacles being removed from the panel. In most cases, light tapping ($A/A_0 \approx 0.9$ where A is the amplitude of AFM cantilever when interacting with samples, and A_0 is the amplitude of AFM cantilever in air) was used in imaging. Different scan sizes, from 1μm x 1μm to 20μm x 20μm, were used to visualize the surface topology and other properties on different length scales. Because the barnacle adhesive can be very sticky, large scan sizes were hard to accomplish under stable scanning conditions.

AFM indentation on barnacle adhesive plaques: AFM experiments were accomplished under seawater. Indentation experiments were designed as follows: a constant maximum indentation force (~30 nN) was set for indentation on all barnacles. On each barnacle, indentation points were chosen sequentially along the radial direction of barnacle adhesive plaque over the workable area (some barnacles had deep, concave regions on their plaques, which were inaccessible to AFM tips). Contiguous locations were spaced either by 500 μm or 300 μm, depending on the size of baseplates. At each location, two (for the first set of barnacles) or five (for the second set of barnacles) indentation force plots were collected at three proximal points (usually 2μm from each other). Usually, there were several tens to two hundred of indentation force plots collected on a barnacle. The sensitivity values of AFM cantilevers were calibrated on a piece of sapphire before and after the indentation measurement on each sample.

Contact angle measurement: A home-made apparatus was used to measure the contact angle. Measurements were made using static droplets of milli-pure water. Several contact angle measurements were done on each barnacle adhesive plaque and on the film left behind on the panel by barnacles.

Shear Strength measurement: Measurements of barnacle shear strength were based on procedures outlined in ASTM D5618-94, "Standard Test Method for Measurement of Barnacle Adhesion Strength in Shear". Measurements were made on live individuals. A hand-held force gauge was used to apply a force (F) parallel to the attachment plane of the organism at a rate of approximately 4.5 Ns^{-1} until it was removed from the surface. Attachment area was determined by two methods as follows: 1) For the first set of barnacles, barnacle bases were scanned with a Hewlett Packard Scanjet 3500c at 300 dpi and the images analyzed using Sigma Scan Pro5 ™ software to integrate the area or 2) For the second set of barnacles, diameter measurements were taken with digital calipers in four directions along the bases and the average diameter (D_a) was used to calculate the area from $A = (D_a^2)/4$. Adhesive shear strength, τ, was calculated by dividing shear force, F, required to remove the organism by the surface area, A, of attachment ($\tau = F/A$).

Processing of the AFM indentation force plots: The elastic moduli of samples were obtained from sample indentation by considering a rigid axisymmetric tip under an applied load. All force plots were converted into loading force vs. indentation plots, and the load-indentation dependence for a conical shape of tip revolution as described by Sneddon[28] was used to model the measurements.

$$F = \frac{2E\tan(\alpha)}{\pi(1-\nu^2)}\delta^2 \tag{5-3}$$

where F is the loading force, δ is indentation, α is tip semivertical angle, E is the Young's Modulus, and υ is the Poisson ratio. In this model, the indentations are considered to be purely elastic.

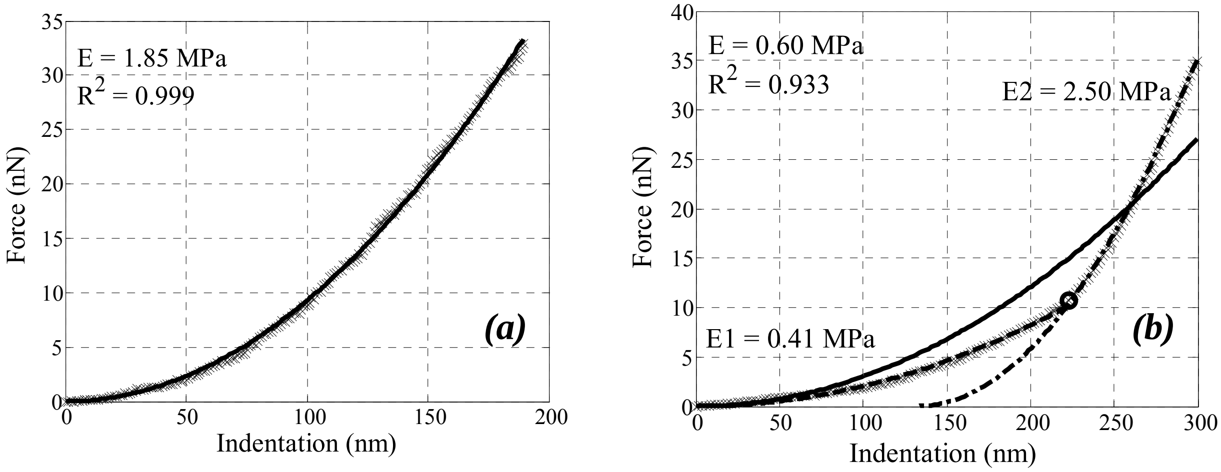

Figure 5-1. Typical force-indentation plots and their fits based on Equation (5-3). (a) A force plot that can be simply fit by Equation (5-3). (b) A force plot that needs to be fit by two sections. *E* is the modulus value obtained from the fit of the overall force curve. *E1* and *E2* are the elastic modulus values obtained from the fits of the first and second section of the force curve. X the original data; —— single modulus fit to the overall force curve; — — fit to the first section of the force curve; — · — fit to the second section of the force curve.

Some typical force-indentation plots and fits based on Equation (5-3) are given in Figure 5-1. Most of the force plots are similar to that seen in Figure 5-1a, which can be simply fit by Equation (5-3). In some cases, the force plots had to be fit by two sections as shown in Figure 5-1b. This was due to a multiple layered structure of barnacle adhesive plaque or a soft contamination attached on the tip.

5.3. Results and Discussion

5.3.1. Effectiveness of the two-section force plot fit

As mentioned above, in some AFM indentation measurements, the force plots showed two sections that could not be well fit by Equation (5-3). Those types of force plots may be due to a multiple layered structure of barnacle adhesive plaque or a soft contamination attached on the tip. There have been a few papers that treat the moduli of a multilayered structure[29-31]. However, all of them used numeric analysis, which would be impractical given the thousands of force plots collected on barnacle adhesive plaque. In our analysis, we used a much simpler model to fit the two-section force plots. In this model, the load is carried by two layers that experience the indentation of a conical tip as shown in Equation (5-4). The two layers are assumed to have the same Poisson ratio.

$$F = \frac{2\tan(\alpha)}{\pi(1-\sigma^2)}\left(E_1\delta_1^{\ 2} + E_2\delta_2^{\ 2}\right) \tag{5-4}$$

where F is the loading force, α is tip semivertical angle, σ is Poisson ratio, E_1 and E_2 are the Young's moduli of the two layers, and δ_1 and δ_2 are the indentations of the two layers. A fit based on Equation (5-4) was given in Figure 5-2. One can see that before the indentation reached 50 nm, the contribution from the second layer was minor while the contribution from the first layer was dominant. E_1 and E_2 are the fitted Young's moduli of the first and the second layers, respectively. When using E_2 to plot a force-indentation curve based on Equation (5-3), *i.e.* without the existence of the first layer, one can see the translated curve fits the data points in the second section well. The analysis was consistent with our previous work[32], which showed how the normalized Young's modulus depends on the normalized indentation and the ratio of Young's moduli of two layers. When the fitted range of the indentation is within about 70% of the thickness of the first layer, the Young's modulus from the fit has an error of less than 20%.

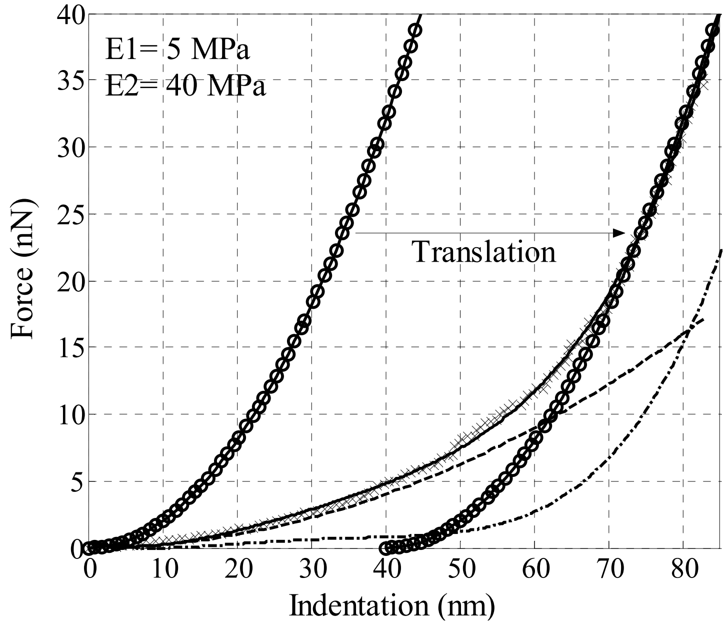

Figure 5-2. A typical two-section force-indentation plot fit by Equation (5-3), ***E1*** **and** ***E2*** **are the Young' s Moduli of the first layer and the second layer from the fit. X the original data; — layered modulus fit to the overall force curve; — — contribution from the first section of the force curve; — · — contribution from the second section of the force curve; θ the simulated force-indentation curve for the second layer without the existence of the first layer. A translation of the simulation curve showed that it fits the second section of the data well.**

5.3.2. Implications of two-section force plots for barnacle adhesive plaque structure

The majority of the two-section force plots were found to be from a multilayered structure of barnacle adhesive plaque, although some intermittent soft contamination of the AFM tip occurred. The absorption of contamination on a tip is a random process with a low possibility because the parental adhesive materials have larger adhesion to the soft contamination adhesive than a hydrophilic AFM tip. Additionally, the sensitivity of each cantilever before and after indentation experiments for each barnacle was checked. The sensitivity values collected at low forces had no obvious changes (data not shown). Therefore, the two-section force plots implied a multilayered structure of barnacle adhesive plaque. Figure 3 shows a cartoon of such a multilayered structure of barnacle adhesive plaque. Each layer has a different Young's modulus, and the modulus increases from the outer layer to the inner layer. A layered adhesive structure is consistent with the way barnacles grow[33], as was observed by Wiegemann[25]. Wiegemann also concluded that there is a continuous decrease of crosslinking within the multilayered adhesive plaque from the outer layer to the inner layers, based on the observation that the stain density faded for each consecutive layer.

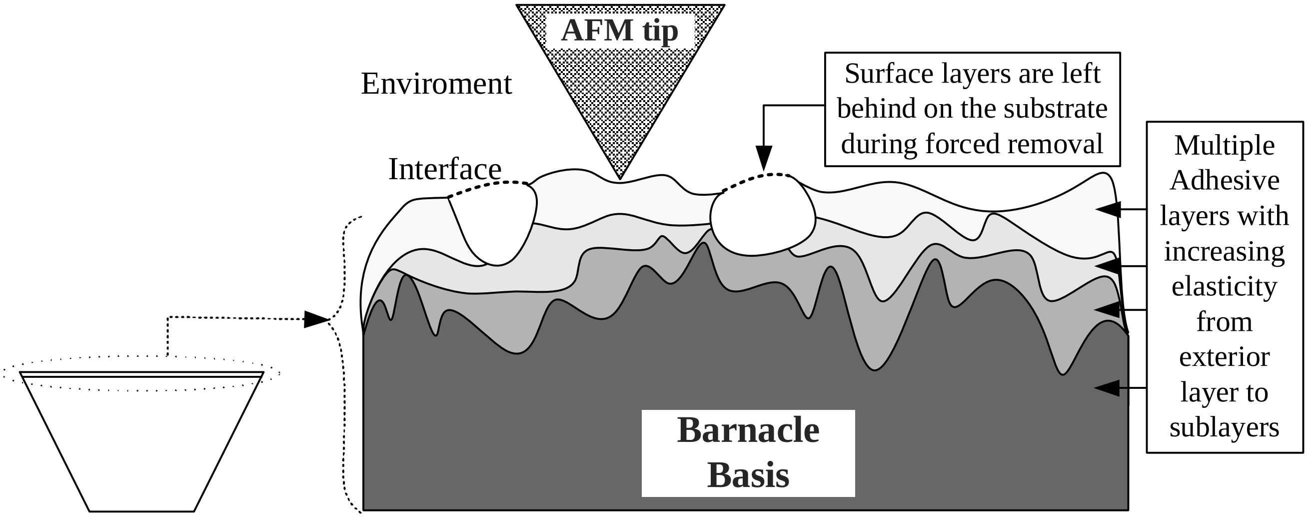

Figure 5-3. A cartoon shows the likely multilayered structure of barnacle adhesive plaque that is implied by the two-section force plots in the AFM indentation experiments. Most of the time, the AFM tip was only able to detect the top two layers due to the preset load.

5.4. Surface elastic moduli of barnacle adhesive plaques

5.4.1. The histogram of barnacle adhesive elastic moduli

The moduli of the barnacle adhesive plaque for a single barnacle fell into a large range, 0.01-100 MPa. This indicates that the released barnacle adhesive plaques were laterally heterogeneous. A few of adhesive plaque regions showed extreme hardness with modulus values of several thousands of MPa, which were believed to be due to the $CaCO_3$ embedment. Figure 4 shows histograms of the surface elastic moduli of barnacle adhesive plaques measured by AFM indentation experiments.

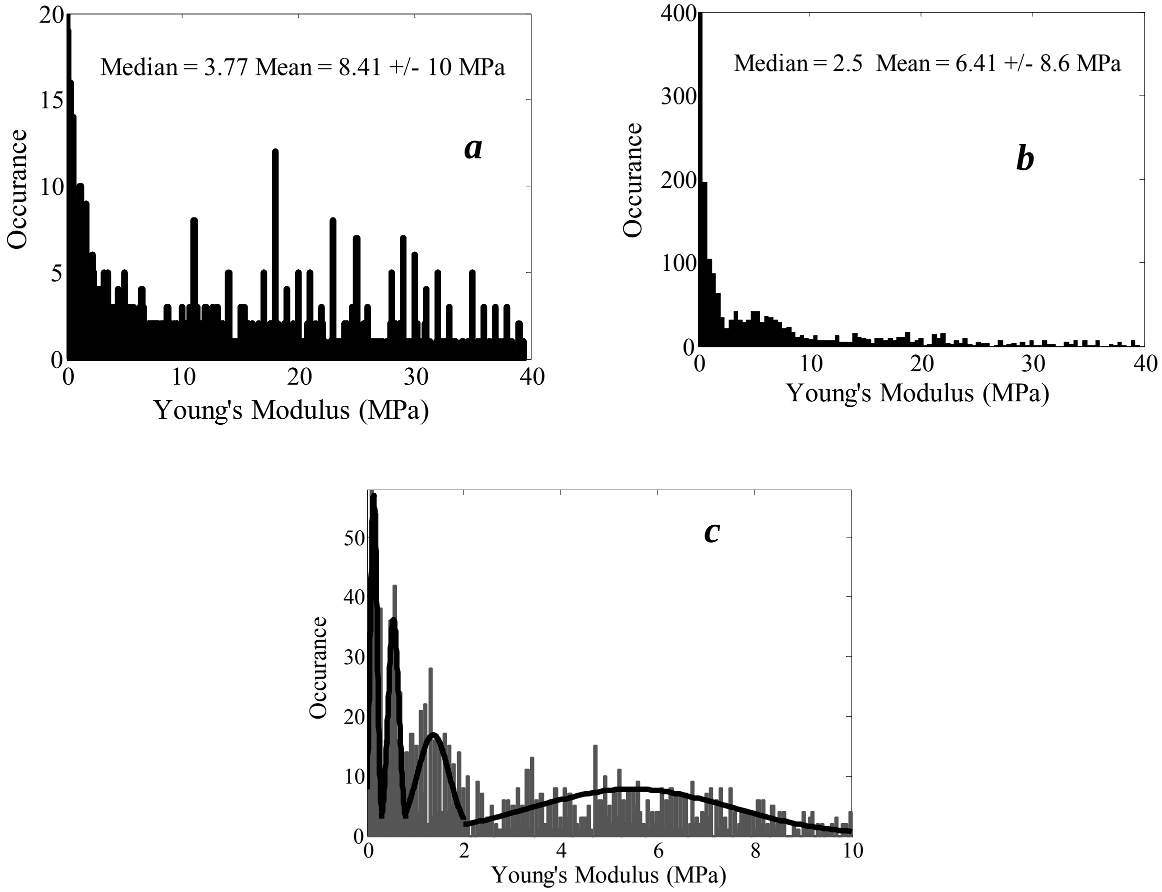

Figure 5-4. Histograms of the surface elastic moduli of barnacle adhesive plaques measured by AFM indentation experiments. a) the first set of barnacle samples; b) the second set of barnacle samples. c) expansion of (b) between 0–10 MPa.

Figure 5-4a summarizes the first set of barnacle samples, and Figure 5-4b and 5-4c summarize the second set of barnacle samples. For the two-section force plots, the Young's moduli of the first layers were included in the histogram. The range of the histograms was chosen between 0 to 40 MPa, which include about 68% of the data within one standard deviation of the mean. Figure 5-4c shows an expansion of Figure 5-4b between 0–10 MPa. Gaussian normal distribution fits in Figure 5-4c showed four characteristic modulus regions, 0-0.3 MPa, 0.3-0.8 MPa, 0.8-2 MPa, and 2-10 MPa. The region 10-40 MPa in Figure 5-4b does not show a normal distribution. However, it was still included in the analysis. Figure 5-4a did not show such obvious regions. Instead, the fraction of values between 10-40 MPa was much larger than seen in Figure 5-4b. This was probably due to the dehydration of the barnacle adhesive during the overnight transportation of the first set of barnacles. We found that the dehydration of barnacle adhesive can harden the material.

5.4.2. Fractural failure modes

To develop a better understanding of the relevance of barnacle adhesive elastic moduli, visual observation, optical light microscopic photography, digital photography, and protein staining were used to study the failure modes of detaching barnacles from PDMS panels. The barnacles studied were from the second set of barnacles, *i.e.*, freshly released barnacles. The substrate surface was T2 Silastic PDMS. Figure 5-5 shows typical photographs and optical light micrographs of the released barnacle adhesive plaque and the failure surfaces after removal of barnacles. In Figure 5-5, it is apparent that for both *Balanus eburneus* (Be) and *Balanus variagatus* (Bv) barnacles released from the T2 Silastic PDMS, incomplete protein adhesive layers were left behind on the substrate. The protein layer left by the Bv on T2 Silastic appeared as ring structures; see Figure 5-5d and 5-5e. Figure 5-5 indicates that the failure mode of Be and Bv barnacles released from T2 Silastic is a mixture of a cohesive failure within the barnacle adhesive layers and an interfacial failure between the first adhesive layer of barnacle and the silicone substrate. Cohesive failures in the barnacle adhesive could occur between sublayers, but with a much lower probability. The cohesive failure implies that for the released barnacle adhesive plaque, at the locations where cohesive failures in the barnacle adhesive occurred, the

AFM tip actually indented into the sublayers. This suggests there are several modulus regions as depicted in Figures 5-4b and 5-4c, *i.e.*, they correspond to different adhesive layers of the adhesive multilayered structure.

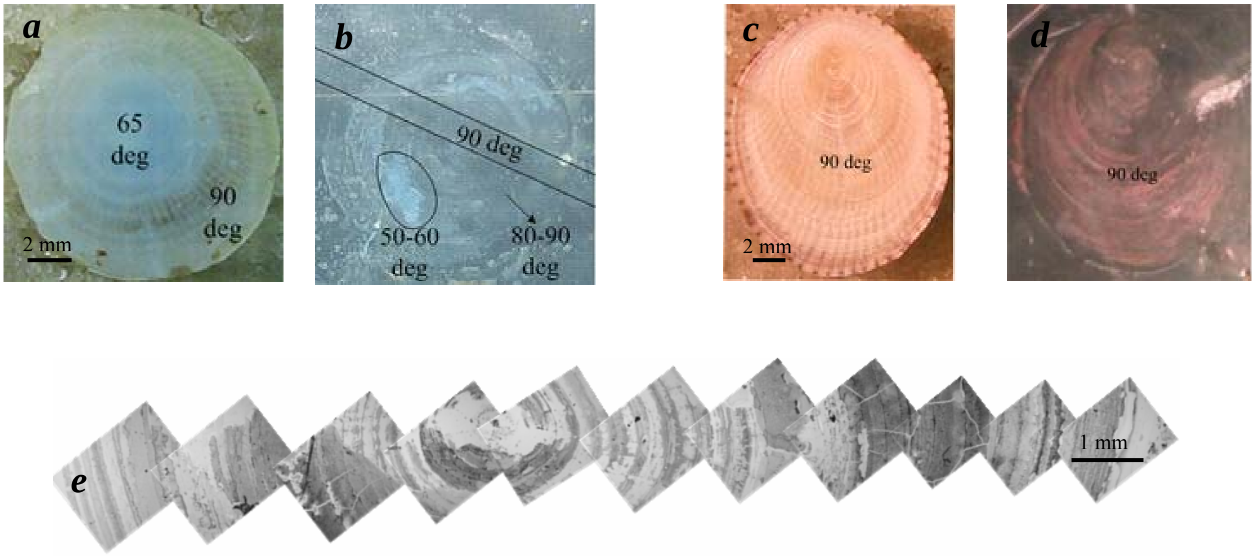

Figure 5-5. Photographs and optical light micrographs of the released barnacle adhesive plaques and the failure surfaces after removal of barnacles. The numbers are the static contact angles measured at the corresponding locations. a) A digital photograph of a Be barnacle after removal from the panel; b) the digital photograph of the failure surface after removal of the Be barnacle in a), without staining; c) A digital photograph of a Bv barnacle after removal from the panel; d) the digital photograph of the failure surface after removal of the Bv barnacle in a), with protein stained red; e) the optical light microscopy photograph of the failure surface after removal of the Bv barnacle followed by protein staining. Protein seen as red in image.

5.4.3. Correlation between the barnacle shear strength of adhesion and the mean adhesive plaque Young's modulus

The mean Young's modulus for the adhesive plaque of each of the first set of barnacles was calculated for the data in Figure 5-4a. Figure 5-6 shows how the mean Young's modulus relates to the barnacle shear adhesion strength.

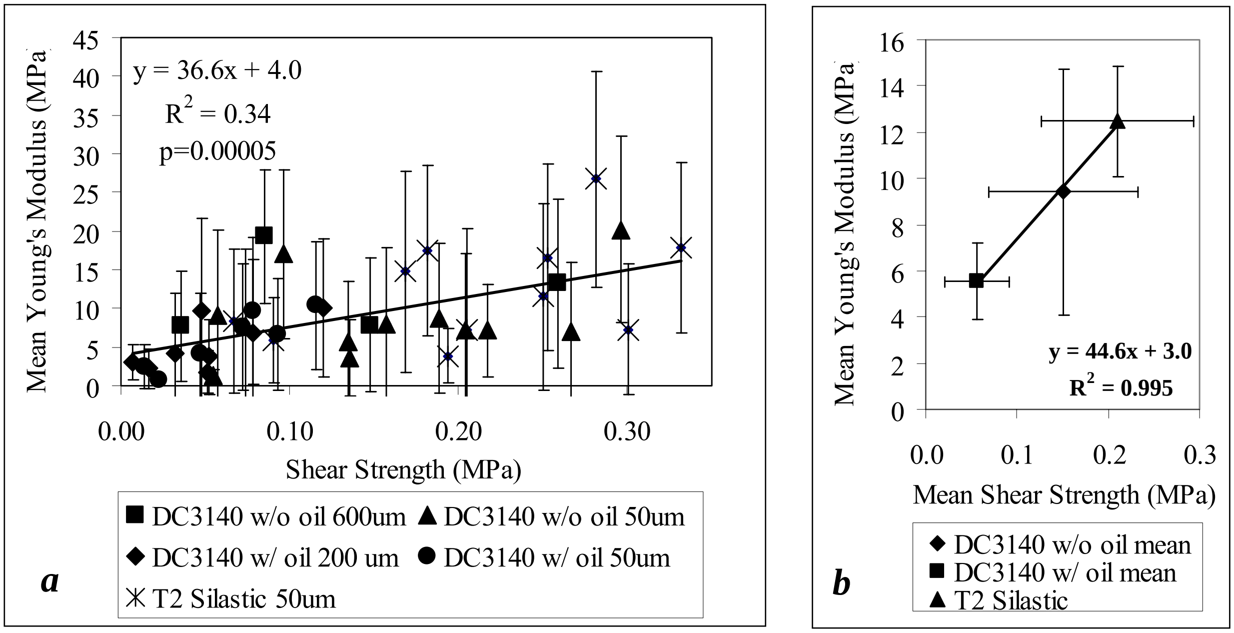

Figure 5-6. The mean Young's moduli for the adhesive plaque vs. the barnacle shear strength of adhesion. a) shows each barnacle on substrates with different PDMS types, additions, and thickness. b) shows the average of barnacles on the same type of substrates with out considering thickness.

Figure 5-6a plots the modulus versus individual barnacle adhesion strength for all substrates. Figure 5-6b plots the modulus versus the average barnacle adhesion strength on the same type of substrates without considering thickness. The plots show that low barnacle adhesion strength correlates with low mean adhesive plaque modulus; and that barnacle adhesion strength was lowest on the DC3140 with oil followed by DC3140 without oil and then T2 Silastic. Figure 5-6a also shows that the adhesive plaque moduli of barnacles on DC3140 with oil have a narrow distribution, while the moduli of barnacles on DC3140 without oil and T2 Silastic have a broad distribution. This is also reflected in the error bars in Figure 5-6b. We do not have a clear explanation for this. However, a reasonable hypothesis is that for the barnacles on DC3140 with oil, which showed lowest shear strength of adhesion, interfacial failure was the dominant mode of fracture. The AFM tip indentations for these barnacle adhesive plaques were mostly into the first layer of the adhesive multilayer, which was softer. For the barnacles on

DC3140 without oil and T2 Silastic, which showed relatively large shear strength, interfacial failure and cohesive failure in the adhesive layers could coexist. The AFM tip indentations on these adhesive plaques were both into the first layer (softer) or into the sublayer (harder) of the adhesive multilayer. Thus, larger mean moduli with a broader distribution were obtained from the AFM indentation experiments.

To investigate the dependence of shear strength of adhesion on different properties of barnacle adhesive and substrates, a multiple linear regression was done. The dependent variable was the barnacle shear strength of adhesion, and the independent variables were the coating type (DC3140, DC3140 + oil, T2 Silastic), coating thickness (50 μm, 200 μm, 600μm), arcsin square root of %soft area, maximum center depth, mean adhesive plaque Young's moduli, and mean contact angles. The *P*-value for the *F* statistic test is less than 0.001 (R^2=0.51, alpha was set as 0.01). The significance of factors is given in Table 5-3. One can see that in the multiple linear regression, the shear strength of adhesion was strongly dependent on the mean Young's modulus for the adhesive plaque, and somewhat dependent on the coating type and maximum center depth, but the contribution from the coating thickness, %soft area, and mean contact angle was no better than random. This suggests that application of the Kendall model for fracture mechanics of an epoxy adhesive on a thin film system[18,20] cannot be used to explain the results of this study.

Table 5-3. The probability level of factors in the multiple linear regression.

Factor	Coating type	Coating thickness	Arcsin sqrt (%soft area)	Maximum center depth	Mean contact angle	Mean adhesive plaque Young's moduli
p	0.028	0.631	0.411	0.073	0.708	0.004

For the second set of barnacles, which were freshly released from panels, five characteristic modulus regions were found (Figure 5-4b and 5-4c). These barnacles were all removed from 600 μm thick T2 Silastic coatings; therefore, there were fewer coating variables for this set of samples than the first set. The correlation between the mean adhesive plaque modulus and the shear strength of adhesion within the five characteristic modulus regions were analyzed separately. Linear and quadratic fits based on Griffith's failure criterion were compared in the correlation analysis. The characteristic length of cracks *a* is needed to quantify in Griffith's fracture theory as seen in Equation (1). However, recent data[34] revealed that the cracking process of barnacle shear release is complex, perhaps fractal. The length of cracks is difficult to quantify. In one approximate evaluation, the radii of barnacle baseplates were chosen to be the characteristic length of cracks. Table 5-4 gives the significance of different regressions between the shear strength of adhesion and the mean adhesive plaque modulus within different characteristic modulus regions for the second set of barnacles. One can see that within the modulus region 0-0.3MPa, the mean adhesive plaque modulus has strong correlation with the shear strength for all three models. There are no correlations for other regions.

Table 5-4. The significances of different regressions between the shear strength of adhesion and the mean adhesive plaque Young's moduli within different characteristic modulus regions for freshly released barnacles.

E (MPa) / Models		0-0.3	0.3-0.8	0.8-2	2-10	10-40
Linear	R^2	0.68	0.07	0.22	0.33	0.06
	p	0.01	0.53	0.25	0.14	0.55
Griffth	R^2	0.62	0.01	0.12	0.27	0.01
	p	0.02	0.78	0.40	0.19	0.84
Quadratic	R^2	0.69	0.02	0.11	0.29	0.02
	p	0.01	0.76	0.41	0.17	0.76

Figure 5-7 shows the mean adhesive plaque modulus of the second set of barnacles within the modulus region 0-0.3 MPa vs. the shear strength of adhesion fitted by different functions. All three fits indicate strong correlations between the mean adhesive plaque Young's modulus and the shear strength of adhesion.

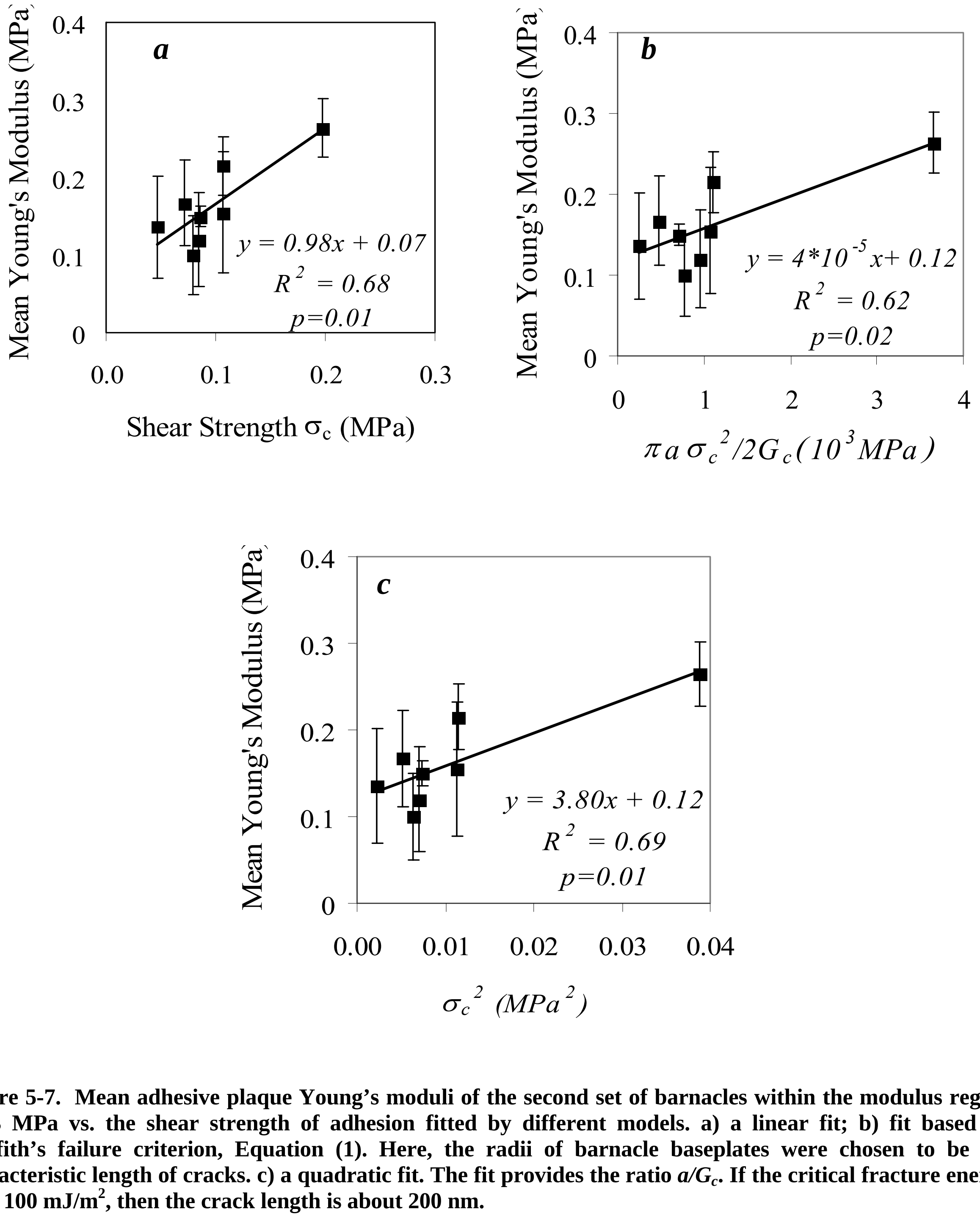

Figure 5-7. Mean adhesive plaque Young's moduli of the second set of barnacles within the modulus region 0-0.3 MPa vs. the shear strength of adhesion fitted by different models. a) a linear fit; b) fit based on Griffith's failure criterion, Equation (1). Here, the radii of barnacle baseplates were chosen to be the characteristic length of cracks. c) a quadratic fit. The fit provides the ratio a/G_c. If the critical fracture energy G_c is 100 mJ/m^2, then the crack length is about 200 nm.

Figure 5-7a is a linear fit. Figure 5-7b is the fit based on Griffith's failure criterion using the radii of barnacle basis to be the characteristic length of cracks. The critical fracture energy G_c is roughly estimated to be 100 mJ/m^2. Figure 5-7c is a quadratic fit. The fit provides the ratio a/G_c. If the critical fracture energy G_c is 100 mJ/m^2, then the crack length is about 200 nm, which is about the size of globules shown in Figure 5-8. This is speculation since we do not know the actual value of G_c in this case. The intercepts of fits in Figure 5-7 can be caused by several reasons. For instance, although we tried to measure the barnacle adhesive plaque modulus as quickly as possible, the operation of taking pictures and contact angle measurements on the barnacle caused slight dehydration of the adhesive before the AFM indentation measurement. This could cause the measured modulus to be larger than the modulus of natural barnacle adhesive. In addition, the elastic PDMS substrate (~0.8 MPa) was ignored in the fits. For improved accuracy, the normalized moduli, which is smaller (~30%), should be used in the fits.

For the first set of barnacles, there was no correlation for small ($E<10$ MPa) mean adhesive plaque moduli. There was good correlation for large ($E>10$ MPa) mean adhesive plaque moduli. The inconsistence of correlation for the two sets of samples could also be due to the dehydration of the barnacle adhesive during the overnight transportation of the first set of barnacles. Dehydration presumably hardened a large fraction of the soft barnacle adhesive on the top layer, thus shifting the correlation to a larger Young's modulus region for the first set of barnacles.

5.4.4. Roughness and viscoelasticity of barnacle adhesive

As mentioned in the section of materials and methods, indentation points were chosen sequentially along the radial direction of each barnacle from center to periphery. The Young's modulus was calculated for each location on a barnacle. There were no significant correlations between the radial distance and the Young's moduli (data not shown). At each location, three proximal points (usually 2 µm from each other) were selected to perform AFM tip indentation. Proximal locations usually had similar moduli. However, in some cases, they showed quite different modulus values indicating that the structure of the barnacle adhesive plaque is heterogeneous over a short length scale (several µm or shorter). To visualize this, AFM tapping mode imaging was done on some of the barnacle adhesive plaque. AFM tapping mode imaging can illustrate the morphology of barnacle adhesive plaque with a high resolution (down to tens of nanometers) and provide information on the viscoelastic properties of barnacle adhesive from phase images. AFM tapping mode images showed that the barnacles had different morphologies. Small structures, down to sub micrometer size, were found as shown in Figure 5-8. The two barnacles in Figure 5-8 were from the second set of barnacles which were freshly released from panels. Both adhesive plaques exhibited globule structures, but the size of globules on *B eburneus* was several times larger than that of and *B variagatus*. The *B variagatus* adhesive plaque was about two times as smooth as the B *eburneus* adhesive plaque.

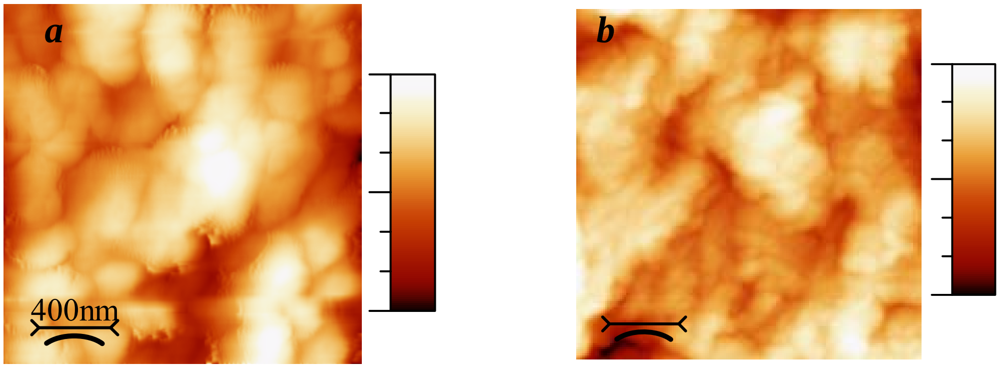

2 µm x 2 µm
RMS Roughness = 35 nm

2 µm x 2 µm
RMS Roughness = 18 nm

Figure 5-8. AFM height images of barnacle adhesive plaque, 2 µm x 2 µm scan size. a) Be barnacle on T2 Silastic; b) Bv barnacle on T2 Silastic.

Unloading force curves from AFM force measurements can provide additional information. Some typical force plots in the barnacle adhesive plaque indentation experiments are shown in Figure 5-9. The hysteresis between the loading and unloading force curves as shown in Figure 5-9a , 5-9b, and 5-9c indicates that the barnacle adhesive is viscoelastic material. Although a quantitative analysis has not been done, one implication of this qualitative observation is that the barnacle shear strength of adhesion should depend on the loading rate of the external removal force. Many force plots had saw-tooth patterns in their unloading force curve as shown in Figure 5-9b. This could be due to the denaturation of protein domains[35] in barnacle adhesive or sequential breaking of multiple bonds, and future analysis of this mechanical denaturization could give valuable insight into the adhesive strength. In some cases, the adhesive was seen to remain stuck to the AFM tip and to exhibit a nonlinear elastic response as seen in Figure 9c. In a few force plots, it was seen that the AFM tip could not break free from the barnacle adhesive even for 2500 nm pulling distance. This might be because the AFM tip indented into a premature adhesive layer, which was soft and sticky, and could withstand large strains.

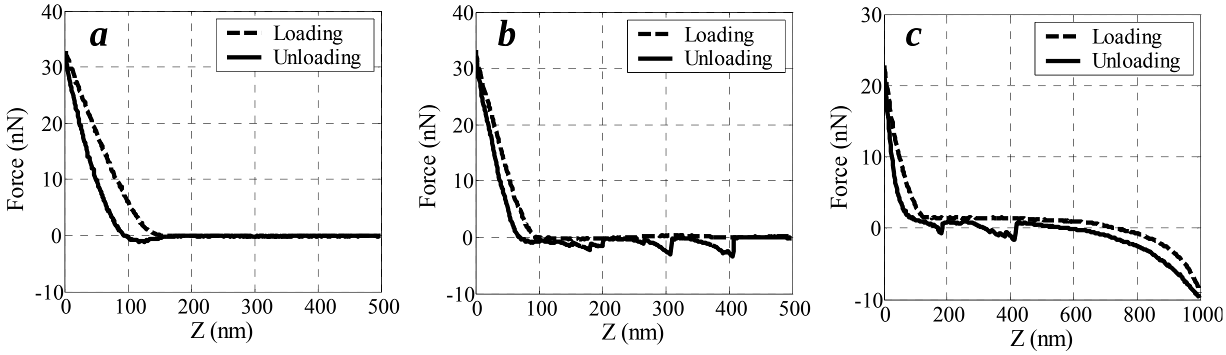

Figure 5-9. Some typical force plots in the barnacle adhesive plaque indentation experiments. a) hysteresis exists between the loading and unloading force curves; b) Saw-tooth pattern in the unloading force curve; c) the AFM tip was stuck in barnacle adhesive.

5.5. Conclusion

The properties of barnacle adhesive plaque were studied by AFM indentation, imaging, and other tests. AFM indentation experiments on freshly released barnacle adhesive plaque revealed that there were several characteristic regions of modulus for the fresh barnacle adhesive, which may be caused by consecutive layers in the multilayered structure of the plaque. Combining the evidence from the protein staining of the substrate, the barnacle fracture from the PDMS substrate was found to occur in a coexistence of interfacial failure and cohesive failure of barnacle adhesive. A multiple linear regression revealed that the shear strength of adhesion was strongly dependent on the mean Young's modulus for the adhesive plaque ($p = 0.004$), and somewhat dependent on the coating type and maximum center depth ($p = 0.028$ and 0.073 respectively), but the contribution from the coating thickness, %soft area, and mean contact angle was no better than random. Hence, a simple application of Kendall's model, which has been proposed by previous research is not seen to apply. For freshly released barnacles, it was found that there is a strong correlation between the shear strength of adhesion and the modulus of the barnacle adhesive that occurred at the surface layer ($E<0.3$ MPa) but no correlation for the modulus measured for the interior layers ($E>0.3$ MPa). Linear regression and quadratic regression based on Griffith's failure criterion work equally well at modeling these observations. A model for a multilayer adhesive structure with complex interactions and fracture patterns is needed to describe the detachment of barnacles from substrates.

BIBLIOGRAPHY

1. Schultz, M. P.;Kavanagh, C. J.;Swain, G. W. *Biofouling* **1999**, *13*, 323-335.

2. Swain, G. W.;Schultz, M. P. *Biofouling* **1996**, *10*, 187-197.

3. Burnell, T. B.;Carpenter, J. C.;Carroll, K. M.;Serth-Guzzo, J.;Stein, J.;Truby, K. E.;Swain, G. W.;Schultz, M. *Advances in nontoxic silicone biofouling release coatings*. in *215th ACS National Meeting*. 1998. Dallas.

4. Mera, A. E.;Fox, R. B.;Bullock, S.;Wynne, K. J. *Proceedings of the Annual Meeting of the Adhesion Society* **1998**, *21st*, 138-140.

5. Berglin, M.;Gatenholm, P. *Journal of Adhesion Science and Technology* **1999**, *13*, 713-727.

6. Brady, R. F., Jr. *Progress in Organic Coatings* **1999**, *35*, 31-35.

7. Tian, J.;Xue, Q. *Acta Oceanologica Sinica* **1999**, *18*, 97-102.

8. Brady, R. F., Jr.;Singer, I. L. *Biofouling* **2000**, *15*, 73-81.

9. Brady, R. F., Jr. *European Coatings* **2000**, *76*, 29-35.

10. Wynne, K. J.;Swain, G. W.;Fox, R. B.;Bullock, S.;Uilk, J. *Biofouling* **2000**, *16*, 277-288.

11. Berglin, M.;Larsson, A.;Jonsson, P. R.;Gatenholm, P. *J. Adhesion Sci. Technol.* **2001**, *15*, 1485-1502.

12. Kavanagh, C. J.;Swain, G. W.;Kovach, B. S.;Stein, J.;Darkangelo-Wood, C.;Truby, K.;Holm, E.;Montemarano, J.;Meyer, A.;Wiebe, D. *Biofouling* **2003**, *19*, 381-390.

13. Hoipkemeier-Wilson, L.;Schumacher, J. F.;Carman, M. L.;Gibson, A. L.;Feinberg, A. W.;Callow, M. E.;Finlay, J. A.;Callow, J. A.;Brennan, A. B. *Biofouling* **2004**, *20*, 53-63.

14. Baier, R. E., in *proceedings of the 3rd International Congress on Marine Corrosion and Fouling*, W.P. Iverson, Editor. 1973, National Bureau of Standards: Gaithersburgh, MD. p. 633-639.

15. Dexter, S. C.;J. D. Sullivan, J.;Iii, J. W.;Watson, S. W. *Applied Microbiology* **1975**, *30*, 298-308.

16. Griffith, A. A. *Philos. Trans. R. Soc. Lond. A* **1921**, *221*, 163-198.

17. Swedlow, J. L. *Intern. J. Fracture Mech.* **1965**, *1*, 210-216.

18. Kendall, K. *J. Phys. D: Appl. Phys.* **1971**, *4*, 1186-1195.

19. Kohl, J. G.;Singer, I. L. *Progress in Organic Coatings* **1999**, 36, 15-20.

20. Patterson, M.;Lakrout, H.;Singer, I. L. *Proceedings of the Annual Meeting of the Adhesion Society* **2000**, 23rd, 71-73.

21. Berglin, M.;Lonn, N.;Gatenholm, P. *Biofouling* **2003**, 19, 63-69.

22. Crisp, D. J. Mechanisms of adhesion of fouling organisms. in *Proceedings of the Third International Congress on Marine Corrosion and Fouling*. **1973**. Evanston, IL: Northwestern University Press.

23. Stein, J., Truby, K., Wood, C. D., Wiebe, D., Montemarano, J., Holm, E., Wendt, D., Smith, C., Meyer, A., Swain, G., Kavanagh, C., Kovach, B., and Lapota, D. *Polymer Preprints* **2001**, 42, 236-237.

24. Berglin, M.;Gatenholm, P. *Colloids and Surfaces B: Biointerfaces* **2003**, 28, 107-117.

25. Wiegemann, M.;Watermann, B. *Journal of Adhesion Science and Technology* **2003**, 17, 1957-1977.

26. Cleveland, J. P.;Manne, S.;Bocek, D.;Hansma, P. K. *Rev. Sci. Instrum.* **1993**, 64, 403-405.

27. Watermann, B.;Berger, H. D.;Sonnichsen, H.;Willemsen, P. *Biofouling* **1997**, 11, 101-118.

28. Sneddon, I. N. *Int. J. Engng Sci.* **1965**, 3, 47-57.

29. Dhaliwal, R. S. *Int. J. Engng Sci.* **1970**, 8, 273-288.

30. Djabella, H.;Arnell, R. D. *Thin Solid Films* **1994**, 245, 27-33.

31. Engel, P. A.;Yang, Q. *Journal of Tribology* **1997**, 119, 1-7.

32. Akhremitchev, B. B.;Walker, G. C. *Langmuir* **1999**, 15, 5630-5634.

33. Walker, G., *in Microscopic Anatomy of Invertebrates 9: Crustacea*, A.G. Humes, Editor. **1999**, John Wiley: New York, NY. p. 249-311.

34. Kavanagh, C. J.;Swain, G. W. *in ONR program review*. **2004**. San Franscisco, CA.

35. Meadows, P. Y.;Bemis, J. E.;Walker, G. C. *Langmuir* **2003**, 19, 9566-9572.

Chapter 6. Concluding Remarks

In this thesis, I described my graduate research work on the mechanics and dynamics of particle assembly and polymer surfaces. Novel methods to assemble colloidal particles into pre-designed patterned on surfaces and measure surface moduli of compliant materials were proposed. The dynamics involved in these processes were studied in detail.

In Chapter 2, I described my research on methodologies of assembling colloidal particles into pre-designed patterns on surfaces. A novel method based on the assistance of surface topography was proposed and investigated in detail. Micrometer-size latex particles were self-assembled in wetting films on patterned poly-dimethylsiloxane (PDMS) polymer surfaces. Based on direct microscopic observations, the mechanisms of the particle transportation and the particle self-assembly were discussed. The particles were transported by a flux caused by the pressure gradient in an evaporating meniscus. The self-assembly of particles was driven by the lateral capillary force between the partially immersed particles. It was found that this topography-assistant method is simple, efficient, and universal. The obtained patterns of particle assembly are reproducible as faithful replicates of the substrate, and with a small number of defects. Varying the constitution and size of particles and substrate patterns accordingly can thus produce required functional devices based on assembled particle patterns. An important future direction of this work is to extend uniform patterning over several millimeters. This is necessary for constructing photonic devices of practical dimensions. In addition, patterning of biological particles using this technique, in varying solvents and with particles of different modulus, should also prove possible. This may also provide insight into the design of textured polymer surfaces for applications such as non-toxic, fouling prevention in marine and implant environments.

In Chapter 3 and Chapter 4, I described my research on the development of a novel method for measuring surface elasticity based on the adhesive interactions between AFM tips and compliant samples surfaces. The method is particularly useful when there is a large adhesion between the AFM tip and soft samples, when the indentation method would be less accurate. The model was tested on PDMS polymers with different crosslink density, and found to work well on soft samples. Without any correction, the results for moderately soft samples such as 18 DP, 25 DP, 37 DP, 60 DP and 120 DP PDMS samples, which have elastic moduli ranging between 10 MPa and 1 MPa, are very close to the results obtained from the macroscopic JKR method.

During the test of the method of elasticity measurement, it was found that for soft, less crosslinked PDMS polymers, such as 253 DP and 705 DP PDMS samples, the results obtained are consistently larger than that obtained by the macroscopic method. This was thought to be due to the larger viscoelastic response between the softer or less crosslinked PDMS polymers and AFM tips. Chapter 4 described the investigation in detail. It was found that energy dissipation occurs mainly in the bulk of polymer when an AFM tip indents into a polymer. When the tip is pulled out from the polymer, the energy dissipation occurs both in the bulk and interfaces, which causes a turning point of the adherence force of AFM tip with changes of scan rates. Multiple relaxation rates are characterized. The study has shown that AFM is a powerful tool to study the damping mechanics of polymer surfaces at nanometer scales.

In Chapter 5, the properties of barnacle adhesive plaque were studied by AFM indentation, imaging, and other tests. AFM indentation experiments on freshly released barnacle adhesive plaque revealed a multilayered structure of barnacle adhesive plaque. Combining the evidence from the protein staining of the substrate, the barnacle fracture from the PDMS substrate was found to occur in a coexistence of interfacial failure and cohesive failure of barnacle adhesive. A multiple linear regression revealed that the shear strength of adhesion was strongly dependent on the mean Young's modulus for the adhesive plaque, and somewhat dependent on the coating type and maximum center depth. For freshly released barnacles, it was found that there is a strong correlation between the shear strength of adhesion and the modulus of the barnacle adhesive that occurred at the surface layer ($E < 0.3$ MPa) but no correlation for the modulus measured for the interior layers ($E > 0.3$ MPa). Linear regression and quadratic regression based on Griffith's failure criterion work equally well at modeling these observations. An important future direction of this work is to build up a model for a multilayer adhesive structure. Complex interactions and fracture patterns will be needed to describe the detachment of barnacles from substrates.